Atomic Force Microscopy Study of Clay Mineral Dissolution

Barry R. Bickmore

Dissertation submitted to the faculty of the Virginia Polytechnic
Institute and State University in partial fulfillment of the
requirements for the degree of

Doctor of Philosophy
in
Geological Sciences

Michael F. Hochella, Jr., Chair
J. Donald Rimstidt
Paul H. Ribbe
Gerald V. Gibbs
Lucian W. Zelazny

December 9, 1999
Blacksburg, Virginia

Keywords: SFM, AFM, crystal structure, periodic bond chain, phlogopite, biotite, vermiculite, montmorillonite, kaolinite, HCl, polyethyleneimine, sapphire, Tempfix.

Atomic Force Microscopy Study of Clay Mineral Dissolution

Barry R. Bickmore

Abstract

An integrated program has been developed to explore the reactivity of 2:1 phyllosilicates (biotite and the clays montmorillonite, hectorite, and nontronite) with respect to acid dissolution using *in situ* atomic force microscopy (AFM). Three techniques are described which make it possible to fix these minerals and other small particles to a suitable substrate for examination in the fluid cell of the atomic force microscope. A suite of macros has also been developed for the Image SXM image analysis environment which make possible the accurate and consistent measurement of the dimensions of clay particles in a series of AFM images, so that dissolution rates can be measured during a fluid cell experiment. Particles of biotite and montmorillonite were dissolved, and their dissolution rates normalized to their reactive surface area, which corresponds to the area of their edge surfaces (A_e). The A_e-normalized rates for these minerals between pH 1-2 are all $\sim 10^{-8}$ mol/m^2•s, and compare very well to other A_e-normalized dissolution rates in the literature. Differences between the A_e-normalized rates for biotite and the BET-normalized rates (derived from solution chemical studies) found in the literature can be easily explained in terms of the proportion of edge surface area and the formation of leached layers. However, the differences between the A_e-normalized montmorillonite rates and the literature values cannot be explained in the same way. Rather, it is demonstrated that rates derived from solution studies of montmorillonite dissolution have been affected by the colloidal behavior of the mineral particles. Finally, the dissolution behavior of hectorite (a trioctahedral smectite) and nontronite (a dioctahedral smectite) were compared. Based on the differential reactivity of their crystal faces, a model of their surface atomic structures is formulated using Hartman-Perdock crystal growth theory, which explains the observed data if it is assumed that the rate-determining step of the dissolution mechanism is the breaking of connecting bonds between the octahedral and tetrahedral sheets of the mineral structure.

“It would be hard to say which is the more miraculous, to make a stone speak or to make a philosopher shut up.”

-Sozomen, Ecclesiastical History

Acknowledgements

I would like to thank Mike Hochella and Barbara Bekken for the wisdom, guidance, availability, and deep friendship they have given me over the past 5 1/2 years. From now on, my advice to students looking for a graduate advisor will simply be, “Find someone like Mike Hochella.”

Several professors, especially Lucian Zelazny and Don Rimstidt, have spent a great deal of time discussing ideas with me and keeping me on the right track. I thank them for their deep commitment to education.

My work would have been impossible, quite literally, if not for the efforts of my coworkers, Eric Rufe, Dirk Bosbach, Steve Barrett, and Laurent Charlet. Each added essential ingredients that serendipitously came together in my dissertation.

I also appreciate the friendship, intelligence, and know-how of the graduate students and postdocs who have been in the Rimstidt/Hochella geochemistry group during my tenure here. These include Jodi, Kevin, Udo, Dirk, John, Chris, Eric R., Eric W., Jeane, Rob, Steve, Erin, and Treavor.

The office staff in Geological Sciences, including Mary, Carolyn, Linda, and Connie, have been good friends and indispensable guides through the bureaucratic morass that is Virginia Tech.

My wife, Keiko, has put up with far more than she had to in order to get me through school and into a “real job”. I will always treasure the love, support, and encouragement she has given me during this time. None of this would be worthwhile without being able to share it with her.

I am constantly amazed by my children, Elijah and Amaya, who give everything in my life added meaning. They also remind me how smoothly life can sail with a little faith, imagination, and forgiveness behind the sails.

Finally, I thank God, who has made His love, forgiveness, care, and existence, known to me in several very specific and striking ways. “Where is your wise man now, your man of learning, or your subtle debater—limited, all of them, to this passing age? God has made the

wisdom of this world look foolish. As God in his wisdom ordained, the world failed to find him by its wisdom, and he chose to save those who have faith by the folly of the Gospel." (1 Corinthians 1:20-21) I give my praise to Him who makes the stones speak and the philosophers shut up!

Table of Contents

Table of Figures

Table of Tables

Chapter 1: Introduction

The Problem of Reactive Surface Area

One of the most pressing problems in the field of geochemistry is the characterization of "reactive surface area". When chemical reactions take place at the surfaces of mineral grains, they proceed via specific mechanisms, which depend on the presence of particular surface functional groups. However, since the crystal structures of many minerals are anisotropic, these functional groups are often distributed heterogeneously. For example, on a single crystal, two crystal faces not related by symmetry might have very different densities of the site in question, or similar sites on the two faces might have differences related to their chemical environment, which cause them to react differently. The net result of this phenomenon is that the reaction rate is not necessarily proportional to the total surface area of a mineral grain. This is a significant problem, because reaction rates for mineral-fluid interactions have traditionally been normalized to total surface area, as measured by BET or a similar technique, so the absolute values of these rates may not be strictly comparable from sample to sample.

Therefore, for any surface-controlled reaction taking place at a mineral surface, the difficulty at hand is threefold. First, the mechanism of reaction must be determined. Second, the distribution of the surface sites involved in the rate-determining reaction step must be characterized. Finally, the reaction rate must be normalized to some value that is proportional to the number of these sites available. Experimentally, these problems would usually be solved in reverse. That is, once the relative reactivity of different surfaces on a crystal is determined, it can be assumed that any differences are related either to the abundance or specific bonding environments of the available reactive sites. Given a model of the surface atomic structures involved, and hence the types of surface functional groups available, the rate determining step of the reaction mechanism may sometimes be inferred.

In this project, a new, integrated experimental approach has been designed, utilizing *in situ* Atomic Force Microscopy (AFM), to characterize the reactivity of 2:1 phyllosilicate clay surfaces during acid dissolution. These minerals were chosen because of the extreme anisotropy of their crystal structures, which gives rise to a relatively well defined "reactive surface area". That is, their basal surfaces consist of fully bonded siloxane groups, which are comparatively unreactive. On the other hand, their edge surfaces are dominated by broken bonds, which are generally very reactive, and it is well-established that acid dissolution of 2:1 phyllosilicates proceeds at these edges. *In situ* AFM was chosen as a means to attack the problem because of its ability to create 3-dimensional profiles of single clay particles under aqueous solutions. Thus, the reactivity of different crystal surfaces can be tracked as the dissolution reaction progresses.

Overview

In Chapter 2, three new sample preparation techniques are described, which make it possible to fix clay minerals and other very small particles down on a substrate for *in situ* AFM imaging. These techniques open a number of possible avenues of research on small particles, but until now, such studies have not been possible, and therefore this represents a significant scientific advance.

In Chapter 3, a suite of macros programmed for the Image SXM image analysis environment is described, which allow for the consistent and accurate measurement of the perimeter, area, and volume of discrete features (e.g. clay particles) in AFM images. In the context of this project, the software allows for accurate measurements of edge surface area (A_e) and the particle volume, so the dissolution rates, normalized to the reactive surface area, can be obtained for single clay particles from a reaction series of AFM images.

Chapter 4 describes dissolution experiments performed on biotite and montmorillonite particles at pH 1-2. The dissolution rates were normalized to reactive surface area, which corresponds to A_e. The A_e-normalized rates obtained for these minerals between pH 1-2 are all $\sim10^{-8}$ mol/m^2•s, and compare very well to other A_e-normalized dissolution rates in the literature. Differences between the A_e-normalized rates for biotite and the BET-normalized rates (derived from solution chemical studies) found in the literature can be easily explained in terms of the proportion of edge surface area and the formation of leached layers. However, the differences between the A_e-normalized montmorillonite rates and the literature values cannot be explained in the same way. Rather, it is demonstrated that rates derived from solution studies of montmorillonite dissolution have been affected by the colloidal behavior of the mineral particles.

In Chapter 5, the dissolution behavior of hectorite (a trioctahedral smectite) and nontronite (a dioctahedral smectite) were compared. Based on the differential reactivity of their crystal faces, a model of their surface atomic structures is formulated using Hartman-Perdock crystal growth theory, which explains the observed data if it is assumed that the rate-determining step of the dissolution mechanism is the breaking of connecting bonds between the octahedral and tetrahedral sheets of the mineral structure.

Impact

The value of this study should be judged on the merits of the “useful things” that have come out of it. Such a list might include the following. First, this study has produced the *only* methods now available to fix very fine particles for *in situ* AFM analysis. Since *in situ* imaging is one of the most unusual and powerful capabilities of AFM, researchers in many disciplines will hopefully find these techniques, and similar ones, highly useful. Second, the software developed for the measurement of features in AFM images is both convenient and powerful. Most AFM users do not begin to use the amount of information available in these images, and this software will greatly enhance their ability to more fully utilize this new experimental technique. Third, this study has produced some of the only A_e-normalized phyllosilicate dissolution rates now available. These serve as a baseline from which to interpret dissolution rates obtained using other methods, and it has become apparent which factors need to be considered in order to fully characterize phyllosilicate dissolution kinetics. Finally, this study has produced the *only* experimental evidence with any reasonably direct bearing on the atomic structures of phyllosilicate edge surfaces and the rate-controlling step in the phyllosilicate dissolution mechanism. These are extremely difficult topics to approach experimentally, and it is hoped that the experimental and analytical techniques adopted here will serve as a model to enable future advances in the field of mineral-fluid reaction kinetics.

Chapter 2: Methods for Performing Atomic Force Microscopy Imaging of Clay Minerals in Aqueous Solutions

Introduction

Atomic force microscopy (AFM) is a powerful technique for the characterization of mineral surface microtopography and reactivity (see Nagy and Blum, 1994; Hochella, 1995). One great strength of AFM is that it characterize surface microtopography directly in solution. Thus it can track the progress of reactions such as mineral growth, dissolution and heterogeneous precipitation as they occur (Drake *et al.*, 1989; Hillner *et al.*, 1992; Dove and Hochella, 1993; Bosbach and Rammensee, 1994; Dove and Chermak, 1994; Junta and Hochella, 1994; Bosbach *et al.*, 1995; Putnis *et al.*, 1995; Bosbach and Hochella, 1996; Bosbach *et al.*, 1996; Grantham and Dove, 1996; Liang *et al.*, 1996; Junta-Rosso *et al.*, 1997). However, none of the above real-time, in-situ studies involved clay minerals because the standard sample preparation techniques used to fix clay particles for AFM characterization in air are inadequate for fluid-cell applications (Dove and Chermak, 1994). Therefore, AFM work on clays is concentrated on observations of microtopography of clay mineral surfaces and the morphology of clay particles, as measured in air (Lindgreen *et al.*, 1991; Blum and Eberl, 1992; Garnaes *et al.*, 1992; Johnsson *et al.*, 1992; Sharp *et al.*, 1992; Gaber and Brandow, 1993; Blum, 1994; Nagy, 1994; McDaniel *et al.*, 1995; Brady *et al.*, 1996; Zbik and Smart, 1998). The application of AFM techniques to the study of clay-mineral surface reactivity has mainly involved inferences made from these *ex-situ* observations (Dove and Chermak, 1994; Nagy, 1994).

Sample preparation for imaging clay particles with AFM involves fixing the particles onto some substrate. However, to image under fluid, certain criteria must be met: 1. The substrate surface must be locally smooth to aid in image interpretation. Not only is it difficult to find particles on a rough surface, but the more irregular the surface, the more artifacts are introduced into the imaging process, also. Similarly, accurate measurement of whole-particle morphology requires a well-defined baseline. 2. The substrate surface must be "sticky" with respect to the particles of interest. Thus, the particles must not float away upon introduction of fluid, and they must not be swept away from the imaging area by lateral forces caused by the scanning motion of the AFM tip. TMAFM greatly reduces the lateral tip-sample forces (Johnson, 1995), and requires a less "sticky" substrate than does contact mode AFM. 3. The substrate surface cannot be too soft, that is, the AFM tip cannot interact too strongly with the substrate. In this case, minute portions of the substrate can adhere to the tip and change its shape. TMAFM also reduces the tip-sample interaction, and is capable of imaging softer surfaces than contact mode AFM (Hansma *et al.*, 1994). 4. The substrate surface must be relatively insoluble in the solutions used, and also inert to the reactions of interest.

In this paper, three techniques suitable for preparing clay-size particles for AFM examination in solution are described, and they generally meet the above criteria. In one technique, clay-size phyllosilicates are fixed on a polished single-crystal _-Al_2O_3 (sapphire) substrate that holds clay particles by electrostatic attraction. In another technique, a mica substrate is coated with a monolayer of polyethyleneimine, a cationic polyelectrolyte, which also fixes clay particles by electrostatic attraction. Finally, clay particles are anchored into the surface of a thermoplastic adhesive, Tempfix. Each technique has advantages and disadvantages, but together they allow for the AFM examination of a variety of clay-size particles in aqueous solution.

Materials and Methods

Samples and characterization

Four samples were used, two clays (Georgia kaolinite, KGa-1, and Na-montmorillonite, SWy-1, both obtained from The Clay Minerals Society Source Clay Repository and used as received) and clay-size fractions of phlogopite (Kingsmere, Ontario, Canada) and vermiculite (Phalaborwa Igneous Complex, Palabora, South Africa). The phlogopite was prepared by grinding on a fixed diamond wheel, after which the < 2 μm size fraction was separated by sedimentation. Vermiculite was soaked for 3 h in 1% HCl and cleaned in an ultrasonic bath to remove carbonate impurities. Cleavage sheets were then ground with a file, after which the < 2 μm fraction was separated by sedimentation.

Chemical analyses of the phlogopite and vermiculite were obtained using the electron microprobe and the X-ray fluorescence (XRF), respectively. Analyses of KGa-1 and SWy-1 standard clay samples were obtained from van Olphen and Fripiat (1979). These analyses were used to calculate permanent charge (see below) values for each sample.

Instrumentation

Instruments used included an Artek sonic dismembrator (Dynatech Laboratories, Chantilly, Virginia, model 300), a Dimension 3000 atomic force microscope (Digital Instruments, Santa Barbara, California), a MultiMode atomic force microscope (Digital Instruments, Santa Barbara, California), a Cameca SX-50 electron microprobe (Cameca Instruments, Trumbull, Connecticut), a Philips PV9550 X-ray fluorescence (XRF) unit (Philips Analytical X-Ray, Mahwah, New Jersey), a Perkin-Elmer (PHI) 5400 X-ray photoelectron spectroscopy (XPS) unit (Perkin-Elmer Corporation, Norwalk, Connecticut), a Dohrmann DC-80 total organic carbon analyzer (Tekmar-Dohrmann, Cincinatti, Ohio), and an ISI SX-40 scanning electron microscope (International Scientific Instruments, Milipitas, California).

AFM imaging

In AFM experiments, all particles were imaged under deionized water. For phlogopite particles fixed on the polished sapphire substrates and the montmorillonite particles fixed on the polyethyleneimine-coated mica substrates images were obtained under NaOH and HNO_3 of various strengths. A plastic petri dish was used as the fluid cell for the Dimension 3000, whereas the closed fluid cell supplied by Digital Instruments was used with the MultiMode. Both AFMs were operated in TappingMode (TMAFM). The Dimension 3000 was used with the polished sapphire and Tempfix, whereas the MultiMode was used with the polyethyleneimine-coated mica substrates. Oxide-sharpened silicon nitride tips on 100 μm long, thick-legged cantilevers (Digital Instruments) were used because their resonant frequencies in solution are suitable for

TMAFM imaging. The cantilever oscillation must be driven at 1-2 V RMS (root mean square) amplitude to image accurately the clay particles.

The AFM images are constructed from height data, and were subjected to the flattening routine (a *least-squares* polynomial fit to remove unwanted features from the scan lines) included with the Digital Instruments software. Also, where necessary the images were subjected to a "shadowing" routine included with the ImageSXM image analysis program (v. 1.60, Steve Barrett) to make topographic details apparent.

To confirm that the AFM images taken in solution were accurately reproducing the lateral dimensions of the clay grains, the ground phlogopite was imaged with scanning electron microscopy (SEM). Considering the limitations of imaging edges with AFM due to tip shape (exaggerated as particles become thicker), the grain shapes were reproduced well. Of course, small steps (in the nanometer range) easily observed by AFM were not apparent by SEM.

Polished single-crystal α-Al_2O_3 (sapphire) substrate

Sapphire has a point of zero charge (PZC, see Sposito, 1992) between 8 -9 (Stumm, 1992), whereas mica and other phyllosilicates have a two component surface charge: an overwhelming negative permanent charge (a structural negative charge delocalized on the basal planes), and a minor, pH variable charge with a point of zero net proton charge (PZNPC, see Sposito, 1992) between 2 -6 (*e.g.*, Anderson and Sposito, 1991; Sumner, 1992; Stumm, 1992; Charlet *et al.*, 1993; Hartley *et al.*, 1997) located on edge faces. Thus, sapphire surfaces have a positive surface charge in circumneutral pH conditions, whereas phyllosilicates have a negative surface charge. This allows the phyllosilicate particles to be held to the substrate electrostatically in aqueous solutions near neutral pH. This technique only works when imaging with TMAFM, however, because lateral forces between the scanning tip and the clay particles in contact mode AFM cause the particles to be swept from the imaging area.

A dilute suspension of the clay in deionized water (~1 mg clay per 20 ml water) was prepared and then dispersed with the sonic dismembrator set at ~150 Watts. (Clay particle dispersal on the substrate surface is desirable, because flocculated masses of particles are too difficult to image. Note, however, that excessive ultrasonic dismembration can produce disaggregation of clay particles, especially kaolinite (Blum, 1994). However, for most *in situ* studies of clay surface reactivity this is of little concern.) A polished sapphire window (Insaco, Quakertown, Pennsylvania) with a 20/10 polish (scratch width = 2 µm) was oven heated to ~90°C, and a few drops of the dispersed clay suspension were placed on the heated substrate surface to dry quickly.

To determine the stability of the clay particles fixed to the sapphire substrate under varying surface charge conditions, phlogopite particles were imaged continuously as the pH was varied in the fluid cell. These experiments were initiated by imaging the phlogopite particles in deionized water (pH 4.7) in the open Dimension 3000 fluid cell. NaOH or HNO_3 solutions (pH 12.5 and 1.5, respectively) were then pumped into the cell at ~0.5 ml/min and the effluent was removed at the same rate using peristaltic pumps. AFM images of a single area of the substrate surface were taken under deionized water, and after it was certain that the pH of the fluid cell solution reached that of the inflowing solution. The pH of the final solution in the petri dish was then determined with a pH meter.

Polyethyleneimine-coated mica substrate

Polyethyleneimine (PEI) is a highly branched polyelectrolyte polymer containing primary, secondary, and tertiary amino groups in the ratio 1:2:1 (Alince *et al.*, 1991). A mica substrate coated with a monolayer of PEI has an isoelectric point of ~10, and a large positive surface charge in moderate to low pH conditions (Claesson *et al.*, 1997). Therefore, negatively charged clay particles adhere tightly to a PEI-coated mica substrate, even moreso than to a polished sapphire surface. Contact mode AFM may be used to image clay particles in solution on the PEI-coated surface, as well as TMAFM.

Polyethyleneimine $(C_2H_5N)_n$ (M.W. 1800, Polysciences, Warrington, Pennsylvania) was diluted 1:500, 1:1000, or 1:2000 by volume. A small disc of muscovite was taped with double-sided tape to a similarly-shaped steel AFM sample puck and immersed in the suspension for ~30 s. The muscovite was then rinsed with a stream of deionized water for 5 min and dried in a 90°C oven for 20 min. A dilute suspension of the clay in deionized water (~0.2 mg clay per 20 ml water) was prepared and then dispersed with the sonic dismembrator set at ~150 Watts. The dried PEI-coated muscovite was immersed in the clay suspension for 1 min, and then blown dry with compressed air.

The average thicknesses of the PEI coatings were calculated from the relative intensities of Si_{2p} XPS peaks, using the following equation adapted from Seah (1990)

$$d_{PEI} = \lambda \bullet \cos\theta \bullet \ln\left(\frac{I_{Si2p}}{I_{Si2p}^{\infty}}\right) \qquad (1)$$

where d_{PEI} is the coating thickness, λ is the attenuation length of a Si_{2p} photoelectron within the polymer coating, θ is the angle between the electron detector and a line normal to the plane of the sample, I_{Si2p} is the intensity of the Si_{2p} XPS peak for a coated muscovite sample, and I_{Si2p}^{∞} is the intensity of the Si_{2p} XPS peak for an uncoated muscovite sample under the same instrumental conditions. $\lambda = 2.6$ nm was assumed for Si_{2p} photoelectrons (Hochella and Carim, 1988; cf. Briggs, 1990). The surface concentration of PEI on the coated substrates was calculated using the measured thickness, assuming the PEI coating has the same density as liquid PEI, 1.040 g/cm^3.

The stability of the PEI coating in water was examined by coating muscovite in 1:500 PEI, cutting it into smaller pieces, immersing the pieces in 5 ml deionized water up to 23 h, and then using XPS to determine the relative intensity of the N_{1s} peak.

To determine the stability of the clay particles fixed to the PEI-coated muscovite substrate under varying surface charge conditions, fixed montmorillonite particles were imaged continuously as the pH was varied in the fluid cell. These experiments were initiated by imaging the montmorillonite particles in deionized water in the closed MultiMode fluid cell. NaOH or HNO_3 solutions between pH 12.5 -1.0 were then slowly flushed into the cell via a syringe, after which more images were taken. The high pH solutions did not appear to damage the fluid cell.

Tempfix substrate

A disc-shaped steel sample puck was oven heated to ~120°C, after which a thin slice of Tempfix (Neubauer Chemikalien, Münster, Germany), a thermoplastic adhesive, was placed on the puck and melted. An air stream was used to spread the melted adhesive over the puck evenly, and heating was continued until the Tempfix became smooth. The Tempfix was then cooled to room temperature. A small amount of clay was then dispersed in deionized water (~1 mg per 20 ml) using an ultrasonic dismembrator. One or two drops of this suspension were placed on the Tempfix-covered puck, and quickly dried in a vacuum desiccator to retain some measure of particle dispersion on the Tempfix surface. The sample was then placed in a cool oven and heated to ~38°C, and then removed to cool. This allowed the Tempfix surface to become slightly tacky, while preventing the particles from sinking too deeply into the polymer.

The solubility of the Tempfix was tested by immersing a 15 mg piece of the material (approximately the amount needed to cover the sample puck) in 10 ml deionized water for 6 h, after which we removed the Tempfix and measured the total organic carbon (TOC) content of the water, as well as that of deionized water blanks. The combustion-infrared method described in Greenberg *et al.* (1992) was used to measure TOC.

Results and Discussion

Polished sapphire substrate

The polished sapphire substrate was sufficiently smooth for effective image interpretation. Analysis of TMAFM images of the blank substrates yielded RMS (root mean square) roughness values between 1.3-1.7 nm for scan areas between 2.5-10 µm square (*i.e.*, the standard deviation of the recorded height values was between 1.3-1.7 nm). Although larger features such as scratches and ledges occurred on the polished sapphire surface, there were also large areas that were nearly atomically smooth, and particles were clearly visible in images where clay was deposited on the substrate.

The electrostatic attraction between clay particles with higher surface charge and the sapphire substrate was sufficient to secure the particles sufficiently for effective TMAFM imaging. Figure 1 shows a TMAFM image of a phlogopite (permanent layer charge = 2.0 per $O_{20}(OH)_4$) particle taken under deionized water, and indeed, phlogopite particles were fixed sufficiently for hours of imaging. However, imaging instability occurred when the pH was adjusted to give both the sapphire substrate and the phlogopite edges the same surface charge. At pH values above the PZC of sapphire (both sapphire and clay have a negative surface charge) or below the point of zero net proton charge (PZNPC) of the clay particles (both sapphire and clay edges have a positive surface charge) the particles become unstable on the surface and the lateral forces of the tip, even in tapping mode, often move or sweep them aside. Figure 2 shows a TMAFM image of vermiculite (permanent layer charge = 1.8 per $O_{20}(OH)_4$) particles under deionized water. The vermiculite particles were also held sufficiently by the sapphire substrate.

This method was insufficient for imaging phyllosilicates with a lower permanent layer charge than mica and vermiculite. For example, kaolinite particles, which have essentially no permanent layer charge, were not fixed sufficiently to image properly, and the tip swept them aside easily even in TappingMode. The Na-Montmorillonite (SWy-1, permanent layer charge = 0.7 per $O_{20}(OH)_4$) particles could be imaged, but were still more prone to movement than the mica. Another consideration might be that the the structural charge of both phlogopite and vermiculite is located in the tetrahedral sheet (Bailey, 1984; de la Calle and Suquet, 1988), whereas that of montmorillonite is located in the octahedral sheet (Güven, 1988), reducing the electrostatic attraction according to Coulomb's law (Kodama *et al.*, 1974).

With a hardness of 9 on Moh's scale, degradation of the sapphire substrate surfaces by the AFM tip is not an issue. Similarly, because aluminum oxides and oxyhydroxides are highly insoluble at near-neutral pH values (Baes and Mesmer, 1976), dissolution of the sapphire and contamination of the fluid cell solution were insignificant. Indeed, even at pH values far from neutral, the dissolution behavior of sapphire is not very different from that of an aluminosilicate clay mineral (*e.g.* Walther, 1996).

Polyethyleneimine-coated mica substrate

PEI-coated mica surfaces are nearly as smooth as uncoated mica, because the adsorbed PEI molecules on the mica surface tend to adopt a flat conformation (Böhmer *et al.*, 1990; Dahlgren *et al.*, 1993). Analysis of TMAFM images of the blank substrates yielded RMS roughness values of ~6 Å for substrates coated in a 1:2000 PEI suspension, and between 24-29 Å for substrates coated in either a 1:500 or 1:1000 PEI suspension, with scan areas between 2.5-10 µm square. However, calculations from XPS data revealed no systematic variation in the PEI coating thickness or N surface concentration with suspension concentration. The average thickness of the coating was calculated at 6 ± 3 Å (95% confidence), which is 3×10^{-7} mol

PEI/m^2. Similarly, the ratio of the intensities of the N_{1s} and Si_{2p} peaks was nearly constant, varying between 0.49-0.51, for muscovite samples coated in suspensions of different concentration. Given this data, it is unclear why the surface roughness appeared to vary with coating suspension concentration, but this effect may be due to subtle differences in how the PEI molecules lie on the surface at different solution conditions. In fact, the surfaces of substrates coated in the more concentrated suspensions appeared to be covered with small "lumps", greater than a nanometer high, perhaps indicating that the PEI macromolecules no longer lie flat. In addition, minor instabilities in the tapping oscillations of the tip caused by electrostatic interactions with the polyelectrolyte coating added random noise to the image, which added to the calculated roughness values. These phenomena may also explain the RMS roughness values for 1:500 or 1:1000 PEI-coated substrates, which are high considering that the coating thickness is near 6 Å.

Not only mica and vermiculite, but also montmorillonite and kaolinite adhere to the PEI-coated mica substrates sufficiently for AFM imaging. Figure 3 shows a TMAFM image of SWy-1 montmorillonite, whereas Figure 4 shows a TMAFM image of a kaolinite particle under deionized water. Substrates coated with PEI suspensions of higher concentration appeared to hold low-charge clay particles more tightly, perhaps due to increased surface roughness. It is unclear why kaolinite adheres to the PEI-coated mica surface since kaolinite has essentially no basal surface charge, but perhaps the amine groups in the PEI form hydrogen bonds with the basal siloxane surface on the tetrahedral side of the kaolinite particles.

In experiments where solutions in a range of pH values were flushed into the fluid cell, a significant number of montmorillonite particles adhered well to the substrate surface between pH 1.0-12.0. Some particles became free of the substrate upon introduction of pH 1.0 solution, but others remained fixed and their dissolution was observed. However, at pH 12.5 the surface immediately became particle-free.

It was expected that the montmorillonite particles, which have a PZNPC similar to that of mica, would not adhere as well to the PEI-coated mica substrate at pH values below 2-3 or above 10, because the sign of the surface charge on both clay particle edges and PEI substrate is the same. However, the more complicated behavior occurs because the montmorillonite basal planes are permanently negatively charged, and electrostatic forces are not the only known interactions between PEI and phyllosilicate surfaces. Below pH 2-3, the electrostatic attraction between the substrate and the negatively charged basal planes of some of the particles (in contrast to the positively charged edges) adds to their stability, whereas above pH 10 the electrostatic interactions between the clay surfaces and the substrate are entirely repulsive. Claesson *et al.* (1997) reported that the pull-off force between a PEI-coated mica surface and a bare mica surface is high (at near 500 mN m^{-1}), suggesting a significant contribution from bridging PEI chains (*cf.*, Ruehrwein and Ward, 1952; Aly and Letey, 1988; Gregory, 1989; Sumner, 1992). Also, Luckham and Klein (1984) reported that when polyelectrolyte chains are adsorbed to a mica surface, then compressed between another mica surface, they become irreversibly adsorbed. Therefore, PEI chains between the mica and some montmorillonite particles probably bridge the two surfaces and are irreversibly adsorbed to both. Alternatively, above pH 10, electrostatic and stearic forces combine to create what Claesson *et al.* (1997) called an "electrostearic repulsion" between PEI-coated mica surfaces. Thus, at pH values below 2-3, bridging attraction of PEI chains between the mica substrate and some montmorillonite particles, combined with electrostatic attraction to the clay basal planes, may overcome the electrostatic repulsion caused by the reversed surface charge on the montmorillonite edges. Between pH 10-12.0, adsorption (bridging) forces likely overcome the “electrostearic” repulsion between the negatively charged clay particles and PEI coating. At near pH 12.5 this repulsion may overcome bridging forces, causing all the montmorillonite particles to be repelled from the substrate surface. The hardness of the PEI coating was not an issue when TMAFM was used, but in contact mode the AFM tip often scraped the coating from exposed areas of the substrate and allowed deposition at the edge of the imaging area.

Semi-quantitative XPS measurements of the N_{1s}/Si_{2p} peak intensity ratio on a 1:500 PEI-coated muscovite substrate before and after exposure to deionized water revealed no systematic variation with exposure time (to 23 h), suggesting that any desorption of the PEI coating is minor during the timescale of an AFM experiment (see Figure 5). Thus, adsorption of resuspended PEI onto fixed clay particles, which might alter their surface chemistry, does not appear to be a significant problem.

Tempfix substrate

The Tempfix surface was clearly not as smooth as that of the polished sapphire or PEI-coated mica. Thus, typical RMS roughness values calculated for 10 µm scans of the surface were between 12-13 nm. We chose to use kaolinite with the Tempfix because it failed to adhere adequately to the polished sapphire substrate. Also, KGa-1 is composed of larger particles with a distinctive pseudo-hexagonal morphology, which may be easily detected with a rough substrate surface. In contrast, smectite, which also failed to adhere adequately to the polished sapphire, is fine-grained with no distinctive morphology.

Figure 6 shows a TMAFM image of KGa-1 on the Tempfix surface. Clearly the kaolinite particles adhere to the Tempfix sufficiently, and excellent images can be taken, at least of particles greater than ~0.3 µm in diameter. Smaller particles are either obscured by the relatively rough topography of the Tempfix surface, or sink below the Tempfix surface. Tempfix is not too soft for effective imaging, at least in TMAFM. However, preliminary experiments using AFM in contact mode were unsuccessful because the AFM tips tended to stick to the substrate, and also to dislodge poorly bound particles. These factors contributed to the overall degradation of contact mode image quality.

TOC measurements on deionized water which were in contact with Tempfix for six hours revealed no dissolution of the substrate. The TOC of deionized water before and after exposure to the Tempfix sample was 1.18 ± 0.08 mg/l and 1.14 ± 0.02 mg/l (95% confidence), respectively.

Conclusions

Polished sapphire substrates have the advantage of allowing analysis of clay particles of various sizes and shapes in aqueous solutions with a minimum amount of complication from the substrate. However, polished sapphire may only provide adequate adherence for phyllosilicate particles with a high permanent layer charge, such as mica or vermiculite. PEI-coated mica appears suitable for fixing clay minerals of any variety in aqueous solution. However, it may not be suitable in some experimental settings to have a polyelectrolyte in the system. Clay particles will adhere to Tempfix regardless of surface charge and the Tempfix is relatively inert. However, Tempfix is better for clay particles of well-defined shape and relatively large size because of the uneven nature of its surface, and the tendency of particles to sink below the Tempfix surface.

The sample preparation methods presented here, in total, will enable the examination of any clay mineral and chemical processes associated with its surfaces using fluid cell AFM. Studies now within reach include real-time measurement of clay dissolution, the expansion behavior of clays, the precipitation of oxyhydroxides on clay surfaces, and studies of electrostatic particle interactions. In addition, these techniques should prove useful for studies of particles other than clays. For instance, Tempfix and PEI-coated muscovite have been successfully used to anchor clay-size hematite and lithiophorite ($(Al,Li)MnO_2(OH)_x$) particles for fluid cell AFM analysis, respectively.

Acknowledgements

We thank I. Yildirim (Mining and Mineral Engineering, Virginia Tech) for operating the X-ray fluorescence unit and to T. Solberg and C. Tadanier (Geological Sciences, Virginia Tech) for operating the electron microprobe and total organic carbon analyzer, respectively. We also thank L. Zelazny, J.D. Rimstidt, J. Rosso, K. Rosso and E. Rufe for many useful discussions and comments. K. Nagy and one anonymous reviewer gave thoughtful and very helpful reviews of the initial manuscript. Phlogopite and vermiculite samples were provided by the Virginia Tech Museum of Geological Sciences (phlogopite sample C3-204, Jack Boyle Collection; vermiculite sample H542.) This work was funded by grants from the National Science Foundation (EAR-9527092, EAR-9628023) and the National Science Foundation Graduate Fellowship Program and the American Federation of Mineralogical Societies Scholarship Foundation.

References Cited

Alince, B., Petlicki J., and van de Ven, T.G.M. (1991) Kinetics of colloidal particle deposition on pulp fibers 1. Deposition of clay on fibers of opposite charge. Colloids and Surfaces, 59, 265-277.

Aly, S.M. and Letey, J. (1988) Polymer and water quality effects on flocculation of montmorillonite. Soil Science Society of America Journal, 52, 1453-1458.

Anderson, S.J. and Sposito, G. (1991) Cesium-adsorption method for measuring accessible structural surface charge. Soil Science Society of America Journal, 55, 1569-1576.

Baes C.F., Jr. and Mesmer, R.E. (1976) The Hydrolysis of Cations, 489 pp. John Wiley and Sons.

Bailey, S.W. (1984) Classification and structures of the micas. In Micas, (ed. S.W. Bailey) Reviews in Mineralogy, 13, 1-12. The Mineralogical Society of America

Blum, A.E. (1994) Determination of illite/smectite particle morphology using scanning force microscopy. In Scanning Probe Microscopy of Clay Minerals (ed. K.L. Nagy and A.E. Blum), pp. 171-202. The Clay Minerals Society.

Blum, A.E. and Eberl, D.D. (1992) Determination of clay particle thicknesses and morphology using scanning force microscopy. In Water-Rock Interaction (ed. Y.K. Kharaka and A.S. Maest), pp. 133-140. A. A. Balkema.

Böhmer, M.R., Evers, O.A., and Scheutjens, J.M.H.M. (1990) Weak polyelectrolytes between two surfaces: Adsorption and stabilization. Macromolecules, 23, 2288-2301.

Bosbach, D., and Hochella, M.F. Jr. (1996) Gypsum growth in the presence of growth inhibitors: a scanning force microscopy study. Chemical Geology, 132, 227-236.

Bosbach, D. and Rammensee, W. (1994) In situ investigation of growth and dissolution on the (010) surface of gypsum by Scanning Force Microscopy. Geochimica et Cosmochimica Acta, 58, 843-849.

Bosbach, D., Jordan, G., and Rammensee, W. (1995) Crystal growth and dissolution kinetics of gypsum and fluorite: An in situ Scanning Force Microscope study. European Journal of Mineralogy, 7, 267-278.

Bosbach, D., Junta-Rosso, J.L., Becker, U., and Hochella, M.F. Jr. (1996) Gypsum growth in the presence of background electrolytes studied by Scanning Force Microscopy. Geochimica et Cosmochimica Acta, 60, 3295-3304.

Brady, P.V., Cygan, R.T., and Nagy, K.L. (1996) Molecular controls on kaolinite surface charge. Journal of Colloid and Interface Science, 183, 356-364.

Briggs, D. (1990) Applications of XPS in Polymer Technology. In Practical Surface Analysis (2nd Edition) Volume 1: Auger and X-ray Photoelectron Spectroscopy (ed. D. Briggs and M.P. Seah), pp. 437-483. John Wiley & Sons.

Charlet, L., Schindler, P.W., Spadini, L., Furrer, G., and Zysset, M. (1993) Cation adsorption on oxides and clays: The aluminum case. Aquatic Science, 55, 291-303.

Claesson, P.M., Paulson, O.E.H., Blomberg, E., and Burns, N.L. (1997) Surface properties of poly(ethylene imine)-coated mica surfaces--salt and pH effects. Colloids and Surfaces A, 123-124, 341-353.

Dahlgren, M.A.G., Waltermo, Å., Blomberg, E., Claesson, P.M., Sjöström, L., Åkesson, T., and Jönsson, B. (1993) Salt effects on the interaction between adsorbed cationic polyelectrolyte layers--Theory and experiment. Journal of Physical Chemistry, 97, 11769-11775.

de la Calle, C. and Suquet, H. (1988) Vermiculite. In Hydrous Phyllosilicates (exclusive of micas) (ed. S.W. Bailey), Reviews in Mineralogy, 19, pp. 455-496. The Mineralogical Society of America.

Dove, P. and Chermak, J. (1994) Mineral-water interactions: Fluid cell applications of scanning force microscopy. In Scanning Probe Microscopy of Clay Minerals (ed. K.L. Nagy and A.E. Blum), pp. 139-169. The Clay Minerals Society.

Dove, P.M. and Hochella, M.F. Jr. (1993) Calcite precipitation mechanisms and inhibition by orthophosphate: In situ observations by Scanning Force Microscopy. Geochimica et Cosmochimica Acta, 57, 705-714.

Drake, B., Prater, C.B., Weisenhorn, A.L., Gould, S.A.C., Albrecht, T.R., Quate, C.F., Cannell, D.S., Hansma, H.G., and Hansma, P.K. (1989) Imaging crystals, polymers, and processes in water with the atomic force microscope. Science, 243, 1586-1588.

Gaber, B.P. and Brandow, S.L. (1993) Imaging of cylindrical microstructures in halloysite using atomic force microscopy. Rocks and Minerals, 68, 123.

Garnaes, J., Lindgreen, H., Hansen, P.L., Gould, S.A.C., and Hansma, P.K. (1992) Atomic force microscopy of ultrafine clay particles. Ultramicroscopy, 42-44, 1428-1432.

Grantham, M.C. and Dove, P.M. (1996) Investigation of bacterial-mineral interactions using Fluid Tapping Mode Atomic Force Microscopy. Geochimica et Cosmochimica Acta, 60, 2473-2480.

Greenberg, A.E., Clesceri, L.S., and Eaton, A.D., eds. (1992) Standard Methods for the Examination of Water and Wastewater. American Public Health Association.

Gregory, J. (1989) Fundamentals of flocculation. Critical Reviews in Environmental Control, 19, 185-230.

Güven, N. (1988) Smectites. In Hydrous Phyllosilicates (exclusive of micas) (ed. S.W. Bailey), Reviews in Mineralogy 19, pp. 497-560. The Mineralogical Society of America.

Hansma, P.K., Cleveland, J.P., Radmacher, M., Walters, D.A., Hillner, P.E., Bezanilla, M., Fritz, M., Vie, D., Hansma, H.G., Prater, C.B., Massie, J., Fukunaga, L., Gurley, J., and Elings, V. (1994) Tapping mode atomic force microscopy in liquids. Applied Physics Letters, 64, 1738-1740.

Hartley, P.G., Larson, I., and Scales, P.J. (1997) Electrokinetic and Direct Force Measurements between Silica and Mica Surfaces in Dilute Electrolyte Solutions. Langmuir, 13, 2207-2214.

Hillner, P.E., Gratz, A.J., Manne, S., and Hansma, P.K. (1992) Atomic-Scale imaging of calcite and dissolution in real time. Geology, 20, 359-362.

Hochella, M.F. Jr. (1995) Mineral surfaces: their characterization and their chemical, physical and reactive nature. In Mineral Surfaces (ed. D.J. Vaughan and R.A.D. Pattrick), pp. 17-60. Chapman & Hall.

Hochella, M.F. Jr. and Carim, A.H. (1988) A reassessment of electron escape depths in silicon and thermally grown silicon dioxide thin films. Surface Science, 197, L260-L268.

Johnson, C.A. (1995) Applications of scanning probe microscopy part 4: AFM imaging in fluids for the study of colloidal particle adsorption. American Laboratory, 27, 12.

Johnsson, P.A., Hochella, M.F. Jr., and Parks, G.A. (1992) Direct observation of muscovite basal-plane dissolution and secondary phase formation: An XPS, LEED, and SFM study. In Water-Rock Interaction (ed. Y.K. Kharaka and A.S. Maest), pp. 159-162. A. A. Balkema.

Junta, J.L. and Hochella, M.F. Jr. (1994) Manganese (II) oxidation at mineral surfaces: A microscopic and spectroscopic study. Geochimica et Cosmochimica Acta, 58, 4985-4999.

Junta-Rosso, J.L, Hochella, M.F. Jr., and Rimstidt, J.D. (1997) Linking microscopic and macroscopic data for heterogeneous reactions illustrated by the oxidation of manganese (II) at mineral surfaces. Geochimica et Cosmochimica Acta, 61, 149-159.

Kodama, H., Ross, G.J., Iiyama, J.T., and Robert. J.-L. (1974) Effect of layer charge location on potassium exchange and hydration of micas. American Mineralogist, 59, 491-495.

Liang, Y., Baer, D.R., McCoy, J.M., Amonette, J.E., and LaFemina, J.P. (1996) Dissolution kinetics at the calcite-water interface. Geochimica et Cosmochimica Acta, 60, 4883-4887.

Lindgreen, H., Garnaes, J., Hansen, P.L., Besenbacher, F., Laegsgaard, E., Stensgaard, I., Gould, S.A.C., and Hansma, P.K. (1991) Ultrafine particles of North Sea illite/smectite clay minerals investigated by STM and AFM. American Mineralogist, 76, 1218-1222.

Luckham, P.F. and Klein, J. (1984) Forces between mica surfaces bearing adsorbed polyelectrolyte, poly-L-lysine, in Aqueous media. Journal of the Chemical Society, Faraday Transactions I, 80, 865-878.

McDaniel, P.A., Falen A.L., Tice, K.R., Graham, R.C., Fendorf, S.E. (1995) Beidellite in E horizons of northern idaho spodosols formed in volcanic ash. Clays and Clay Minerals, 43, 525-532.

Nagy, K.L. (1994) Application of morphological data obtained using scanning force microscopy to quantification of fibrous illite growth rates. In Scanning Probe Microscopy of Clay Minerals (ed. K.L. Nagy and A.E. Blum), pp. 203-239. The Clay Minerals Society.

Nagy, K.L. and Blum, A.E., eds. (1994) Scanning Probe Microscopy of Clay Minerals, 239 pp. The Clay Minerals Society.

Putnis, A., Junta-Rosso, J.L., and Hochella, M.F. Jr. (1995) Dissolution of barite by a chelating ligand: An atomic force microscopy study. Geochimica et Cosmochimica Acta, 59, 4623-4632.

Ruehrwein, R.A. and Ward, D.W. (1952) Mechanism of clay aggregation by polyelectrolytes. Soil Science, 73, 485-492.

Seah, M.P. (1990) Quantification of AES and XPS. In Practical Surface Analysis (2nd Edition) Volume 1: Auger and X-ray Photoelectron Spectroscopy (ed. D. Briggs and M.P. Seah), pp. 201-255. John Wiley & Sons.

Sharp, T.G., Banin, A., and Buseck, P.R. (1992) Morphology and structure of montmorillonite surfaces with atomic-force microscopy. American Chemical Society Abstracts, 203, 52.

Sposito, G. (1992) Characterization of particle surface charge. In Environmental Particles vol. 1 (ed. J. Buffle and H.P. van Leeuwen), pp. 291-314. Lewis Publishers.

Stumm, W. (1992) Chemistry of the Solid-Water Interface, 428 pp. John Wiley & Sons.

Sumner, M.E. (1992) The electrical double layer and clay dispersion. In Soil Crusting: Chemical and Physical Processes (ed. M.E. Sumner and B.A. Stewart), pp. 1-31. Lewis Publishers.

van Olphen, H., and Fripiat, J.J., eds. (1979) Data Handbook for Clay Materials and Other Non-metallic Minerals, 346 pp. Pergamon Press.

Walther, J.V. (1996) Relation between rates of aluminosilicate mineral dissolution, pH, temperature, and surface charge. American Journal of Science, 296, 693-728.

Zbik, M. and Smart, R.S.C. (1998) Nano-morphology of kaolinites: Comparative SEM and AFM studies. Clays and Clay Minerals, 46, 153-160.

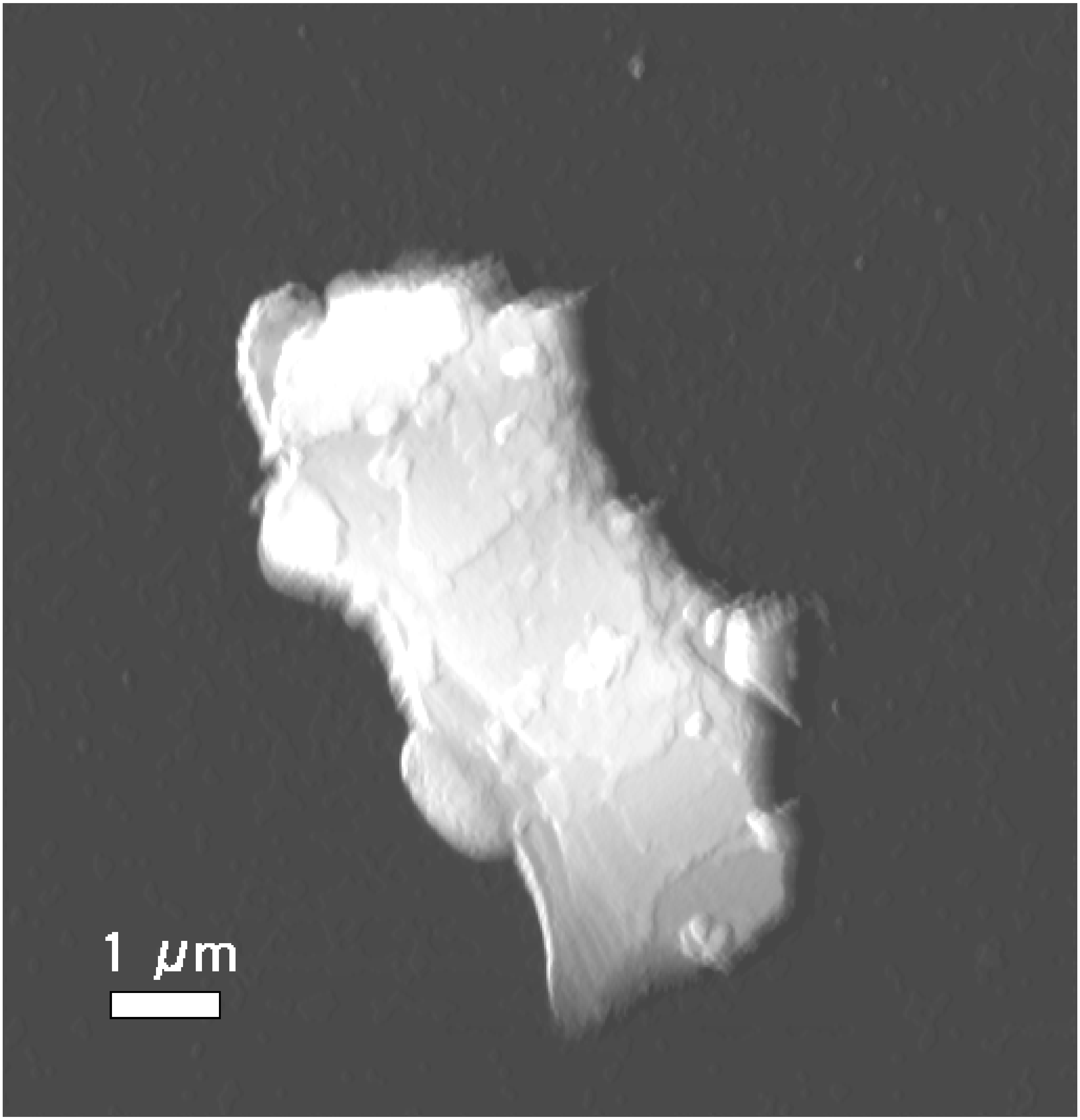

Figure 2-1. TMAFM height image of a ground phlogopite particle electrostatically fixed to a polished sapphire substrate under deionized water. Max particle height = 789 nm.

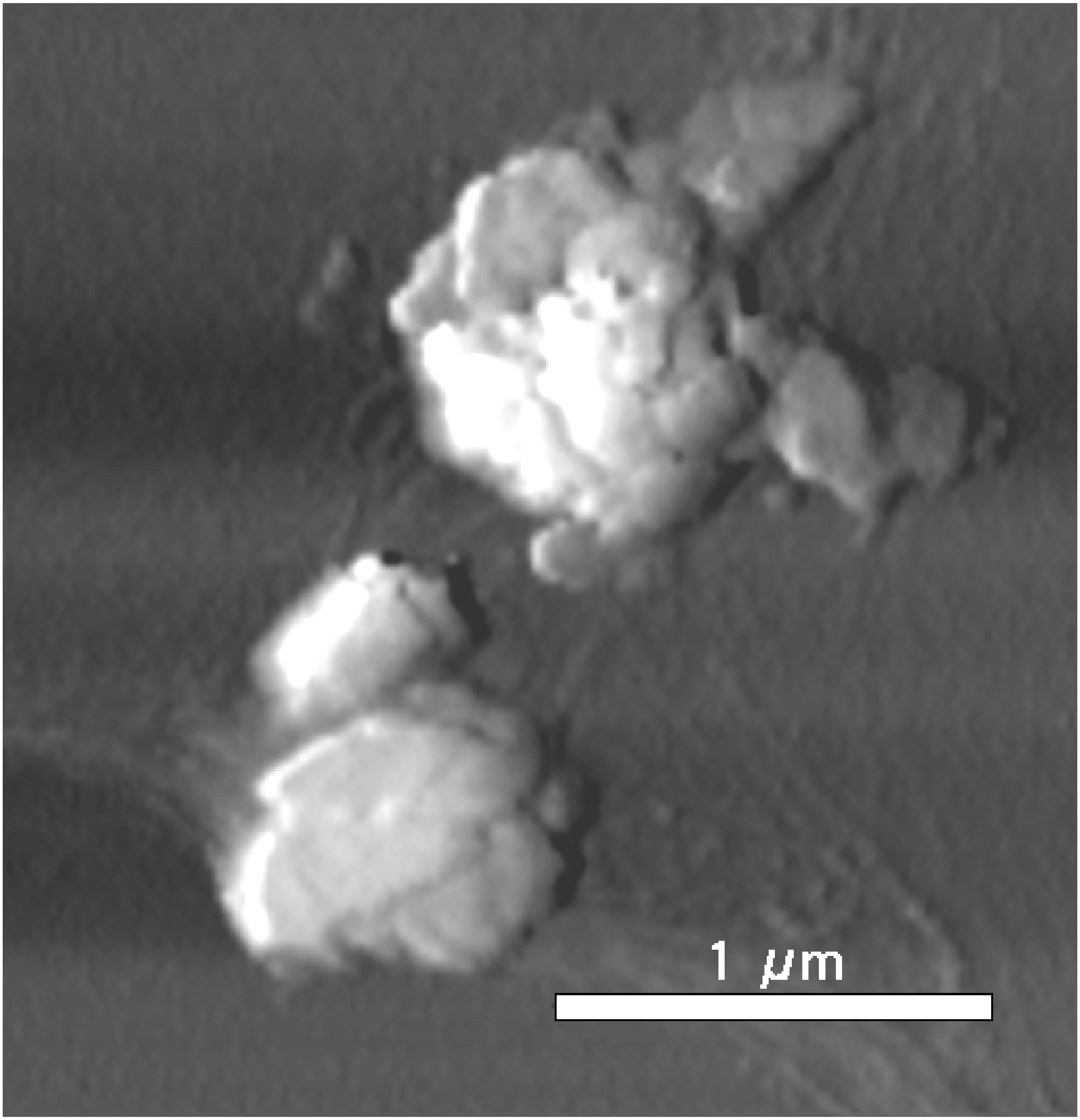

Figure 2-2. TMAFM height image of a ground vermiculite particle on a polished sapphire substrate under deionized water. Max particle height = 370 nm.

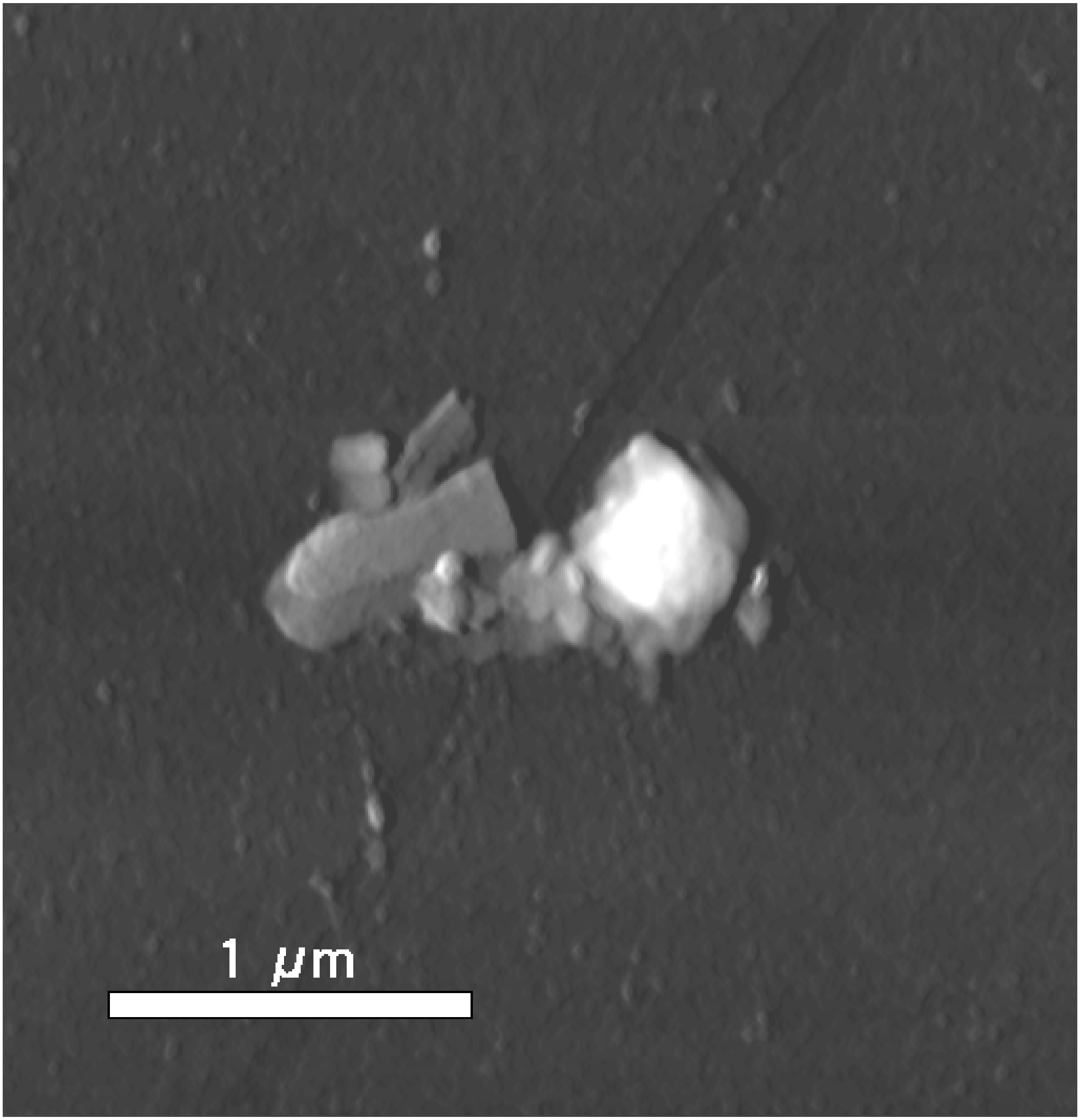

Figure 2-3. TMAFM height image of montmorillonite (SWy-1) particles fixed to a PEI-coated mica substrate under deionized water. Max particle height = 94 nm.

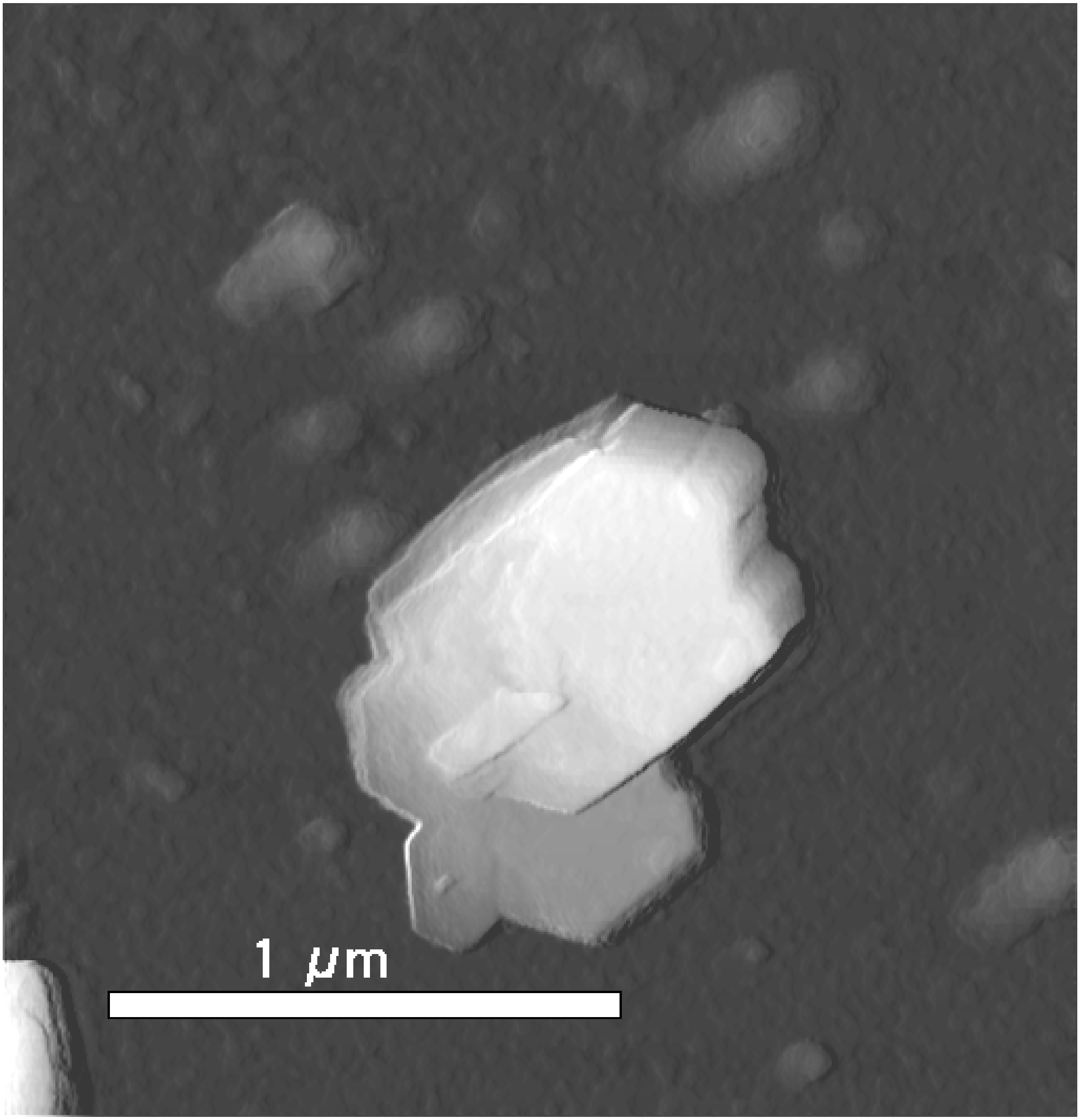

Figure 2-4. TMAFM height image of a kaolinite particle fixed to a PEI-coated mica substrate under deionized water. Max particle height = 201 nm.

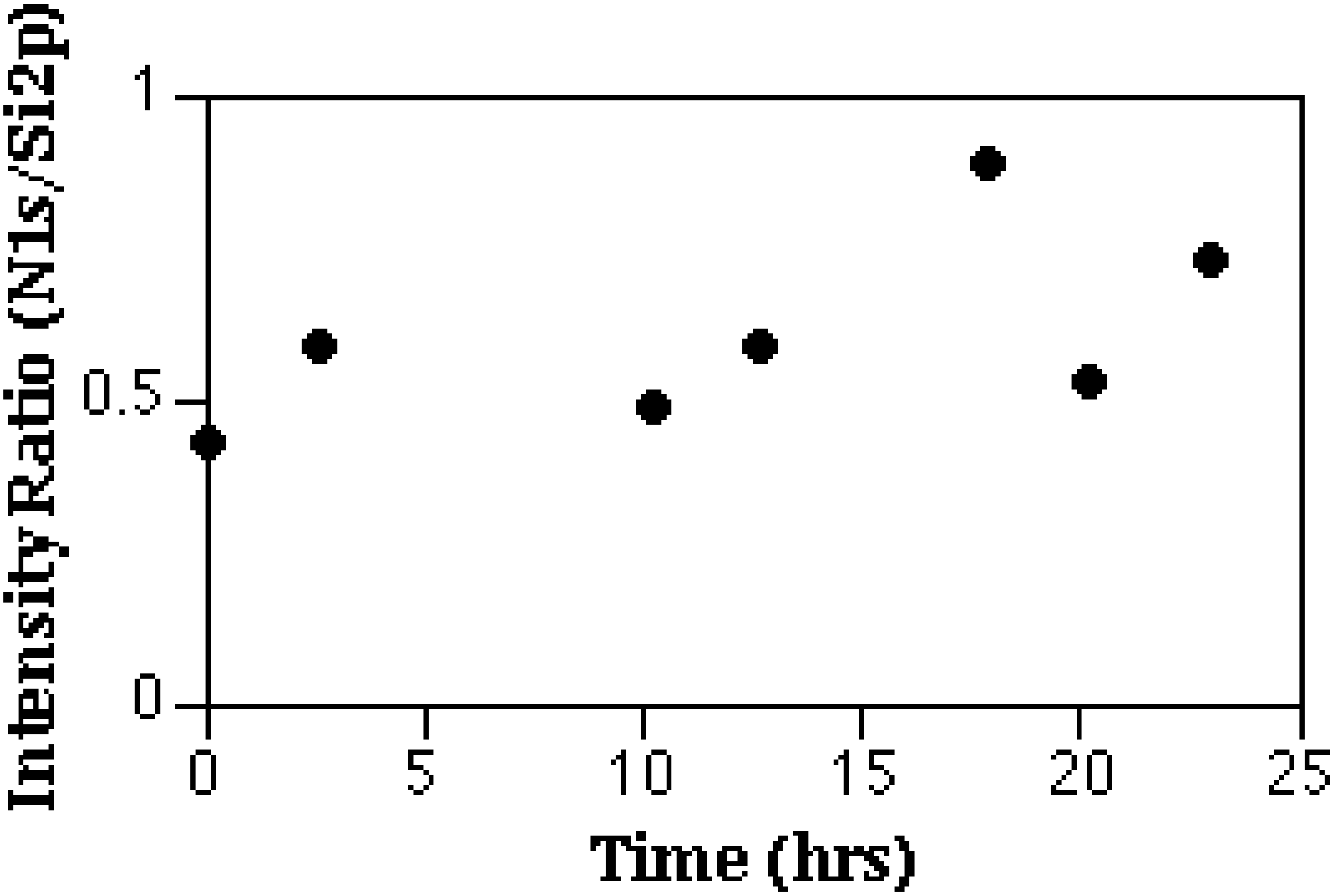

Figure 2-5. Plot of the N1s/Si2p XPS peak intensity ratios for a PEI-coated muscovite substrate vs. exposure time to deionized water. The N1s/Si2p ratio showed no systematic downward trend over time, suggesting that very little, if any, of the adsorbed PEI desorbed.

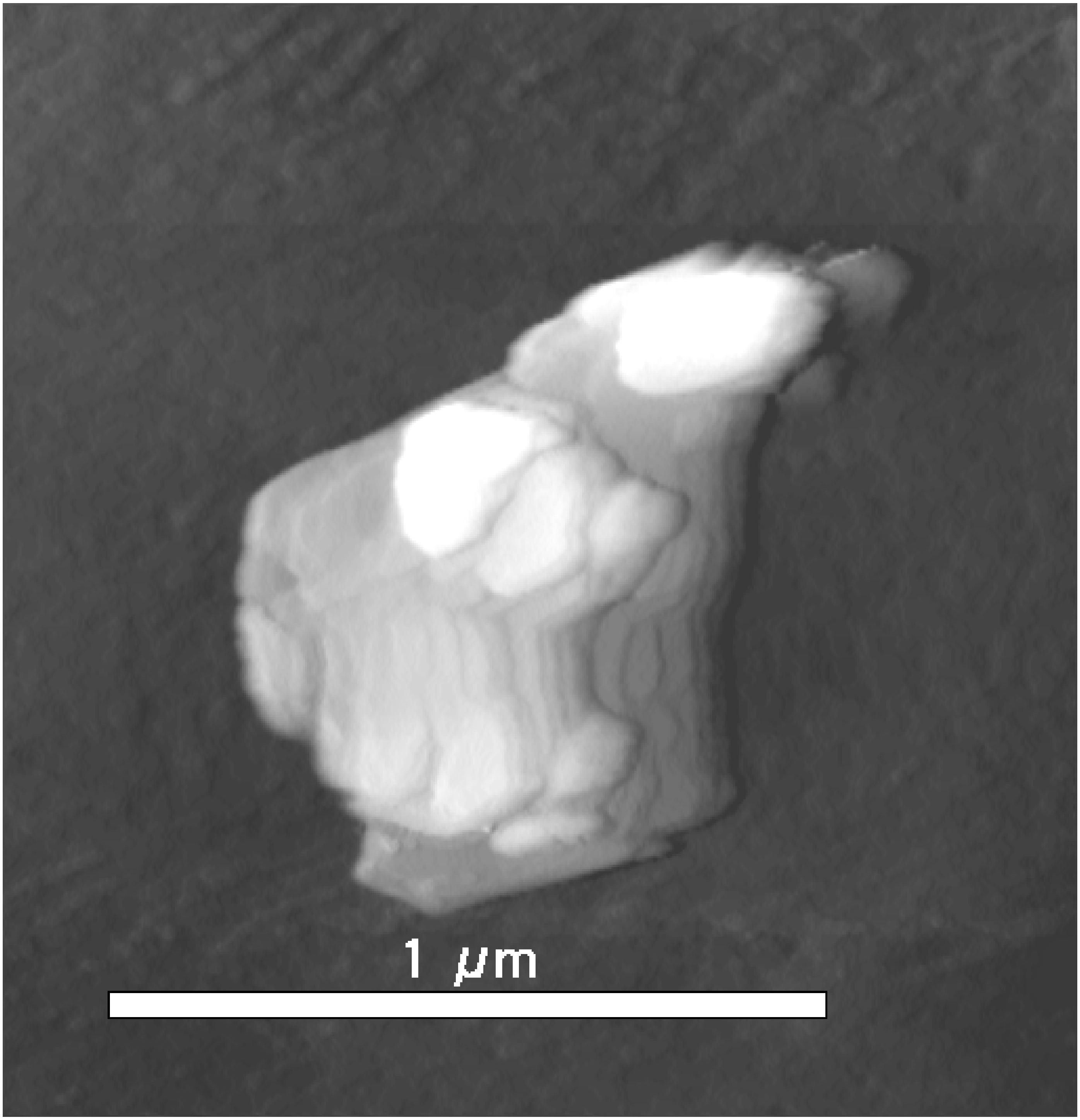

Figure 2-6. TMAFM height image of a kaolinite (KGa-1) particle on a Tempfix substrate under deionized water. Crystallographically controlled, pseudohexagonal angles between 105∞ and 130∞ can easily be distinguished at many of the step edges. Max particle height = 138 nm.

Chapter 3: Measuring Discrete Feature Dimensions In AFM Images With Image SXM

Introduction

In the past decade, a significant number of Earth scientists have successfully employed Atomic Force Microscopy (AFM) to characterize the surface morphology and reactivity of minerals and other environmental particles (for reviews, see Blum and Nagy, 1994; Hochella, 1995; Maurice and Lower, 1997). In this technique, the response of a scanned probe is translated into a digital, 3-dimensional map of a surface. Thus, the spatial dimensions of surface features such as etch pits, as well as small particles deposited on a substrate (e.g. clays) can be measured. The ability of the Atomic Force Microscope to operate under fluids, including aqueous solutions, also allows for the real-time characterization of the rates at which such features and particles grow or dissolve. Some features, such as euhedral etch pits, are conveniently characterized using the standard analysis software that comes with AFM systems, but others have complicated shapes, and require more sophisticated analysis.

Using its built-in macro language, we have customized the Image SXM image analysis environment to measure the perimeter, horizontal area, and volume of discrete surface features and particles in AFM images, obtaining accurate and consistent estimates. Image SXM (Barrett, 1997) is a spin-off of the popular public domain NIH Image analysis software (Rasband and Bright, 1995; Barrett et al., 1995; Liner, 1999), designed especially for the analysis of Scanning Probe Microscopy (SPM), Scanning Electron Microscopy (SEM), and Scanning Auger Microscopy (SAM) images. With respect to SPM images, Image SXM is able to read 3-dimensional image files created by most commercial SPM software packages, and subject them to various analysis routines. Two aspects of this program are especially convenient for the measurement of irregularly-shaped features in AFM images. First, Image SXM allows the user to utilize rectangular, oval, polygonal, and freehand selection tools to define a region of interest

(ROI) of any shape, thus excluding extraneous features. Second, it allows the user to create macros to perform most of the functions of the program automatically, and perform calculations, in a specified sequence.

Users of this software will now be able to quickly obtain reliable measurements of discrete features in AFM images. Such tools allow one to perform tasks which would otherwise be extremely tedious or next to impossible. Examples include calculating reaction rates from time-series images of reacting particles or etch pits with complex shapes (Bosbach et al., 1999; Rufe and Hochella, 1999), and classifying biomolecules and other surface features based on their dimensions (Chen et al., 1996; McMaster et al., 1996).

Algorithms

Perimeter and horizontal area

In order to estimate the perimeter or horizontal area of a discrete feature, the image must be transformed into binary format. That is, a certain height (or pixel intensity) level is chosen as the threshold, and pixels on either side of the threshold are changed either to black or white, depending upon which side of the threshold they fall. The black areas are treated as particles, and the area of each one can be determined by multiplying the number of pixels in the particle by a scaling factor. The perimeter of each particle may be calculated by adding 1 for each edge-touching pixel, and $\sqrt{2}$ for each corner-touching pixel, and then multiplying by a scaling factor (Russ, 1990, pp. 183-185; Russ, 1995, pp. 520-522).

The difficulty in perimeter and horizontal area calculations is deciding at which height level to set the threshold, because, especially in the case of irregularly shaped features, the effect of altering the threshold even slightly can be drastic. In order to estimate consistent values from feature to feature and from image to image, one must decide upon some optimum threshold level at which to make the measurements. Therefore, our Image SXM macros threshold the image at 254 of the 256 possible gray levels (excluding white and black), and calculate the perimeter and area of the particles in the selected area at each setting. The perimeter vs. threshold height curve is then subjected to a 3, 5, 7, or 9 point (user-defined) smoothing routine, and the derivative of the perimeter vs. threshold height curve is calculated at each height level from the smoothed curve. The resulting derivative curve is essentially a map of image complexity vs. threshold setting. That is, perimeter values where the feature boundaries are the least complex will change the least from threshold level to threshold level, and so will produce values near zero in the derivative curve (Russ, 1990, pp. 108-115). Optimum threshold levels are selected where the absolute values of a string of 5 or more consecutive derivative points fall below a user-defined tolerance level.

Volume

The volume of a feature can easily be calculated by first defining a baseline height, and then multiplying the area of the selected ROI by the average pixel height (relative to the baseline height) within the ROI (Russ, 1995, p. 541). This method of volume calculation implicitly assumes that any noise in the image is distributed symmetrically about the true height values. It also ignores effect of AFM tip geometry and other artifacts on the perceived volume, although a user could modify the macro code to account for such things for specific applications.

The volume calculation macros define the baseline height by first creating a histogram of the number of pixels at each height level within the ROI. The histogram is then subjected to a 5-point smoothing routine, after which the height level of the baseline is determined by identifying the maximum of the first large peak from the bottom (in the case of particles) or top (in the case of pits). If there is a significant deviation from the overall baseline in an area within the ROI, a smaller peak in the histogram might interfere with the baseline determination. Therefore, the user is asked to define a minimum (particles) or maximum (pits) height level for the baseline to exclude such anomalies

Directions for Use

Image SXM macros are stored in text files, and are loaded into the program by selecting the "Load Macros" command under the "Special" menu, and selecting the desired file. The macros described here are in a text file named "pavmacro.txt". The following macros are included in the file: 1) "Prepare Temp Window", 2) "Particle Perim-Area", 3) "Pit Perim-Area", 4) "Plot

Particle Perim", 5) "Plot Particle Area", 6) "Plot Particle P-Deriv", 7) "Plot Pit Perim", 8) "Plot Pit Area", 9) "Plot Pit P-Deriv", 10) "Particle Volume", 11) "Pit Volume", and 12) "Plot Smoothed Histogram". This section describes procedures which can be used to utilize these macros to measure discrete features in AFM images.

Image preparation

In preparation for measurement, an image must be subjected to three processes, all of which can be performed using Image SXM or any standard AFM software. First, images must be subjected to a flattening routine, a least-squares polynomial fit to remove unwanted features from the scan lines. This removes variations in the baseline height from scan to scan in an image. Second, if the image is tilted with respect to the x-y plane, a tilt correction routine must be applied. Third, a median filter, which assigns each pixel the median height value of its immediate neighborhood (9 or 25 pixels) must be applied to reduce random noise. While operations such as lowpass filters may flatten out the edges of a feature and thus distort its shape, median filters do not, although some blurring does occur (Russ, 1990, pp. 46-48). Within Image SXM, flattening and tilt correction routines may be found under the "Compensation" category in the "SPM" menu. [Note: It is best to hold the "Shift" key down before using the mouse to pull down the "SPM" menu and select the tilt correction routine. This causes the program to readjust the z-scaling so that objects in the image are not cut off by being moved above or below the original z-scale.] A 3x3 pixel median filter routine can be found under the "Rank Filters" category in the "Process" menu.

Measuring perimeter and area

In order to run macros in Image SXM, one must first choose the "Load Macros" function under the "Special" menu and then select the desired macro text file. The names of the macros in the file then appear in the "Special" menu, and will run when selected.

To measure perimeter/area, one opens the desired image file and then creates a blank temporary image window with dimensions identical to those of the image, by running the "Prepare Temp Window" macro. The image window is automatically brought to the front. One of the selection tools is then used to define a ROI around the feature of interest. The user then runs either the "Particle Perim-Area" or "Pit Perim-Area" macro. The program then measures the perimeter and area of the feature at every height level.

After the perimeter/area calculations have been performed, the user is asked to provide values for the smoothing degree, i.e. the number of points averaged to smooth the perimeter vs. height curve before calculating the derivative. Smoothing degrees of 3, 5, 7, or 9 may be used. The user is also prompted for a perimeter picking tolerance. For instance, a tolerance of 0.005 (the default) means that only perimeter derivative values of 0±0.005 will be considered when the computer picks suitable height levels to measure perimeters and the corresponding areas. (The default values for smoothing degree and tolerance of 7 and 0.005, respectively, usually work well for reasonably simple features within images up to a few µm on a side. A lower smoothing degree might be required if, for instance, the user would like the program to pick a larger number of suitable height levels. A higher tolerance might be desirable if the horizontal area of the image is very large, and hence the derivative reflecting even relatively small changes in the calculated perimeter curve would also be correspondingly larger.) When the tolerance is entered, the program picks any suitable height levels at which to accurately estimate perimeter values, and then prints the corresponding heights and perimeters in the"Info" window. The user is asked whether the results should be saved, and if so the perimeter picks, as well as the area, perimeter, and perimeter derivative values at each height level are saved in a text file in a form easily accessible to a spreadsheet program for further analysis. Whether the file is saved or not, the user will be asked whether the computer should recalculate the results, and if so, the user is prompted for a new smoothing degree and perimeter picking tolerance, after which the derivative curve is recalculated and new perimeter picks are made. The user then has the option of saving the new results file.

In some cases the program will not pick any height levels at which to measure the perimeter, or will not pick any in the specific height region of interest to the user. In that case, the perimeter, area, and perimeter derivative data can be plotted vs. height level by running the "Plot Particle Perim", "Plot Particle Area", "Plot Particle P-Deriv", "Plot Pit Perim", "Plot Pit

Area", and "Plot Pit P-Deriv" macros. These take the data obtained by running the "Particle Perim-Area" or "Pit Perim-Area" macro and create an x-y plot in a separate window. One may obtain the exact coordinates of any point on a plot by running the mouse cursor across the plot window. The x value of the cursor position, and the y value of the plot corresponding to that x value, are displayed in the "Info" window. The user can employ these plots to find the most suitable heights at which to measure perimeter and area by eye.

Often it is useful to obtain the perimeter and area of a feature in a time-series. For instance, the authors have used this software to analyze lateral etch pit growth and clay mineral dissolution in time series of AFM images. Growth/dissolution rates can be measured and related to specific components of the surface area (e.g. the area of step edges). Since the assigned height of the baseline level in an image can vary somewhat due to noise, image drift, etc., it is not useful to pick a height at which to measure the perimeter/area and then measure those values at the same height level throughout the series of images. Rather, it is better to pick a suitable height level to make the measurements in the first image, note the specific feature of the perimeter vs. height plot corresponding to that height level, and then find the same feature in the perimeter vs. height plots in subsequent images to determine where to make the measurements.

Measuring volume

Volume measurements are made by selecting a ROI around the feature of interest, and running either the "Particle Volume" or "Pit Volume" macro. The user is then prompted to define a minimum (particles) or maximum (pits) height level for the baseline. After this is done, the baseline level chosen by the computer and the calculated volume are displayed in the "Info" window. It is useful to then run the "Plot Smoothed Histogram" macro, which creates an x-y plot of the smoothed number of pixels vs. height histogram. Again, by running the mouse cursor across the plot, the user can find the plotted value for the x value of the cursor position, which is displayed in the "Info" window. Using this plot, the user may determine whether the program estimated a reasonable value for the baseline height. If not, the volume macro may be run again, and a minimum or maximum baseline height may be entered to exclude a false result.

Examples

In this section, a few examples will be cited to illustrate both the usefulness of the software described here, and the nature of the results that can be obtained therefrom.

Square pits

Figure 1a shows our first example, which is a synthetic AFM image, created with the drawing and calibration tools included with Image SXM. The base level (i.e. the level above the pits) in this image is at 81 nm. In the center there are two concentric, square pits, the larger one at 48 nm height and the smaller at 11 nm. The larger pit is 2.00 μm on a side, while the smaller is 1.00 μm on a side. After drawing the pit pattern, we also used a macro to add random noise in a normal distribution about the original pixel values. In this case, the standard deviation of the noise distribution about the original pixel values is 5% of the total z-range (black to white,100 nm). The dashed line around the pits marks the selected ROI for our calculations. Figure 1b shows a histogram of the number of pixels in the ROI corresponding to each height level.

Since this is a synthetic image, the values one should expect to measure with the macros are already known. When the "Pit Perim-Area" macro was run (smoothing degree = 7, tolerance = 0.005), the program picked two height levels at which to measure perimeters and areas: 35.3 nm and 68.2 nm. Figure 2 shows plots of the perimeter, perimeter derivative, and area vs. threshold height obtained by running the plotting macros described above. The dashed lines in the figure denote the height levels the program picked. These plots show that the program picked height levels for measurement near the upper edges of the pits, but where the perimeter (and area) values change very little. Figure 3 illustrates this principle even more clearly. Here a cross section of the pits is shown, and again the dashed lines indicate the height levels picked. It is readily seen that heights were chosen near the upper edges of the pits, but just below where the noise in the image would complicate the measurements.

The program should be expected to measure perimeters and areas for the smaller pit in the neighborhood of 4 μm and 1 μm^2, and indeed, the measured values were 3.97 μm and 1.00 μm^2. The measured values for the larger pit, 8.02 μm and 4.00 μm^2, are similarly in agreement with the expected values, 8 μm and 4 μm^2.

When the "Pit Volume" macro was run, it correctly picked the baseline level at 81 nm (see Figure 4), and calculated a pit volume of –0.168 µm^3. The expected value was 0.169 µm^3. Thus, all of the measured values for perimeter, area, and volume are within 1% of the expected values. Certainly the more complicated shapes and imaging artifacts found in real AFM images would degrade the accuracy of these measurements, but this example serves to show that their most limiting factor is likely the quality of the data itself.

Irregularly-shaped clay particle

Figure 5a is an AFM image of a montmorillonite clay particle fixed to a polyethyleneimine-coated mica substrate, taken under deionized water (see Bickmore et al., 1999). The image was subjected to flattening and median filter routines to remove variations in scan line height and random noise, respectively. The baseline height of the image around the particle is ~2 nm, and it exhibits two distinct terraces at ~8 nm and ~14 nm.

When the "Particle Perim-Area" macro was run, the program picked two heights at which to make measurements: 6.7 and 12.9 nm. Figures 5b and 5c show the binarized image, thresholded at these height levels. Careful comparison of these with Figure 5a reveals that if one were to trace the outline of the particle for measurement by eye, the true perimeter and area of the particle would likely be significantly overestimated. Figure 6 shows a cross-section of the particle, with the height levels picked by the computer algorithm marked by dashed lines. This figure illustrates the fact that the measurement routine picks height levels near the top of the terraces, to minimize the error associated with edge-broadening due to the pyramidal shape of the AFM probe tip, but just below where the rounded end of the probe tip, random noise, etc., begin to complicate the image.

The experimental artifacts just mentioned are made apparent in Figure 6, and hence it also serves to illustrate potential sources of error in the volume calculations. Although we cannot be certain of the "true" value of the particle volume, an "expected" volume was approximated using the measured heights and areas of the terraces, and the "Particle Volume" macro was run. Whereas a volume of 1.21×10^{-3} µm^3 was expected, the routine calculated a volume of 1.35×10^{-3} µm^3, representing an error of ~12%. If errors of this magnitude are unacceptable, users may wish to customize this measurement routine (or create new routines) to account for artifacts specific to their images. For instance, the following references describe methods to remove tip-sample interaction artifacts, which may add significantly to the measured volume (Keller, 1991; Keller and Franke, 1993; Bonnet et al., 1994; Markiewicz and Goh, 1994; Markiewicz and Goh, 1995; Wilson et al., 1995; Villarrubia, 1997).

Dissolving mica etch pit – time series

Figure 7 is an animation of a time series of AFM images of some etch pits on a phlogopite mica surface, that are dissolving in pH 2 HCl (see Rufe and Hochella, 1999). A ROI was selected around the largest pit in each of these images, and the "Pit Perim-Area" macro run. Figure 8 consists of perimeter vs. threshold height plots for these images, in sequence from top to bottom. The dashed lines mark the threshold heights the computer program picked to measure perimeter and area values. This figure clearly shows that the baseline height of the image can change significantly in such a sequence, but the feature corresponding to the ideal measurement height in each perimeter vs. threshold height plot is easily identified.

Figure 9 is a plot of the pit volume (calculated by multiplying the measured pit area by the step height of 1.0 nm) vs. time. The lack of scatter in this data illustrates plainly the utility of having measurement tools to estimate accurate and consistent values for discrete feature dimensions in AFM images. In addition, phlogopite mica is a 2:1 phyllosilicate, which is known to dissolve inward from edge surfaces, rather than etching of the basal surfaces. The information gained from subjecting images such as these to the analysis routines described here can be used to obtain dissolution rates for these minerals, normalized to the reactive (edge) surface area. In fact, such information, obtained in a much more tedious fashion, has already been used in this way (Rufe and Hochella, 1999; Bosbach et al., 1999).

Obtaining the software

Links for downloading the latest version of Image SXM and the macros described in this paper from the World-Wide Web can be found at the following address:

http://www.geocities.com/Athens/Parthenon/2671/Macros.html

Acknowledgements

This work was funded by grants from the National Science Foundation (EAR-9527092, EAR-9628023) and the Petroleum Research Fund of the American Chemical Society (PRF 31598-AC2, 34326-AC2). Additional funding was supplied by the National Science Foundation Graduate Fellowship Program and the American Federation of Mineralogical Societies Scholarship Foundation. E.R. would also like to thank K. Rosso for programming instruction during the early stages of this project.

References Cited

Barrett, S.D., Leibsle, F.M., and Dipple, S.J. (1995) Customised image analysis made easy. Microscopy and Analysis, 47, 17-19.

Barrett, S.D. (1997) Image analysis and the internet. Scientific Data Management, 1, 18-25.

Bickmore, B.R., Bosbach, D., Hochella, M.F., Jr., and Charlet, L. (1999) Methods for performing atomic force microscopy imaging of clay minerals in aqueous solutions. Clays and Clay Minerals, 47, 573-581.

Bonnet, N., Dongmo, S., Vautrot, P., and Troyon, M. (1994) A mathematical morphology approach to image formation and image restoration in scanning tunneling and atomic force microscopies. Microscopy Microanalysis Microstructures, 5, 477-487.

Bosbach, D., Charlet, L., Bickmore, B.R., and Hochella, M.F., Jr. (1999) The dissolution of hectorite: In-situ, real-time observations using Atomic Force Microscopy. American Mineralogist, in press.

Chen X.Y., Davies M.C., Roberts C.J., Shakesheff K.M., Tendler S.J.B., Williams P.M. (1996) Dynamic surface events measured by simultaneous probe microscopy and surface plasmon detection. Analytical Chemistry, 68,1451-1455

Hochella, M.F. Jr. (1995) Mineral surfaces: their characterization and their chemical, physical and reactive nature. In Mineral Surfaces (ed. D.J. Vaughan and R.A.D. Pattrick), pp. 17-60. Chapman & Hall.

Keller, D.J. (1991) Reconstruction of STM and AFM images distorted by finite-sized tips. Surface Science, 253, 353-364.

Keller, D.J. and Franke, F.S. (1993) Envelope reconstruction of probe microscopy images. Surface Science, 294, 409-419.

Liner, C.L. (1999) Geophysics and NIH image. Computers and Geosciences, 25, 403-414.

Markiewicz, P. and Goh, M.C. (1994) Atomic Force Microscopy probe tip visualization and improvement of images using a simple deconvolution procedure. Langmuir, 10, 5-7.

Markiewicz, P. and Goh, M.C. (1995) Simulation of Atomic Force Microscope tip-sample/sample-tip reconstruction. Journal of Vacuum Science and Technology, B13, 1115-1118.

Maurice, P.A. and Lower, S.K. (1997) Using Atomic Force Microscopy to study soil mineral reactions. Advances in Agronomy, 62, 1-43.

McMaster T.J., Winfield M.O., Baker A.A., Karp A., Miles M.J., (1996) Chromosome classification by Atomic Force Microscopy volume measurement. Journal of Vacuum Science and Technology, B14, 1438-1443.

Nagy, K.L. and Blum, A.E., Eds. (1994) Scanning Probe Microscopy of Clay Minerals, 239 pp. The Clay Minerals Society.

Rasband, W.S. and Bright, D.S. (1995) NIH Image – A public domain image-processing program for the Macintosh. Microbeam Analysis, 4, 137-149.

Rufe, E. and Hochella, M.F., Jr. (1999) Quantitative assessment of reactive surface area of phlogopite during acid dissolution. Science, 285, 874-876.

Russ, J.C. (1990) Computer-Assisted Microscopy: The Measurement and Analysis of Images, 453 pp. Plenum.

Russ, J.C. (1995) The Image Processing Handbook, 2nd Ed., 674 pp. CRC.

Villarrubia, J.S. (1997) Algorithms for scanned probe microscope image simulation, surface reconstruction, and tip estimation. Journal of Research of the National Institute of Standards and Technology, 102, 425-455.

Wilson, D. L., Kump, K.S., Eppell, S.J., and Marchant, R.E. (1995) Morphological restoration of Atomic-Force Microscopy images. Langmuir, 11, 265-272.

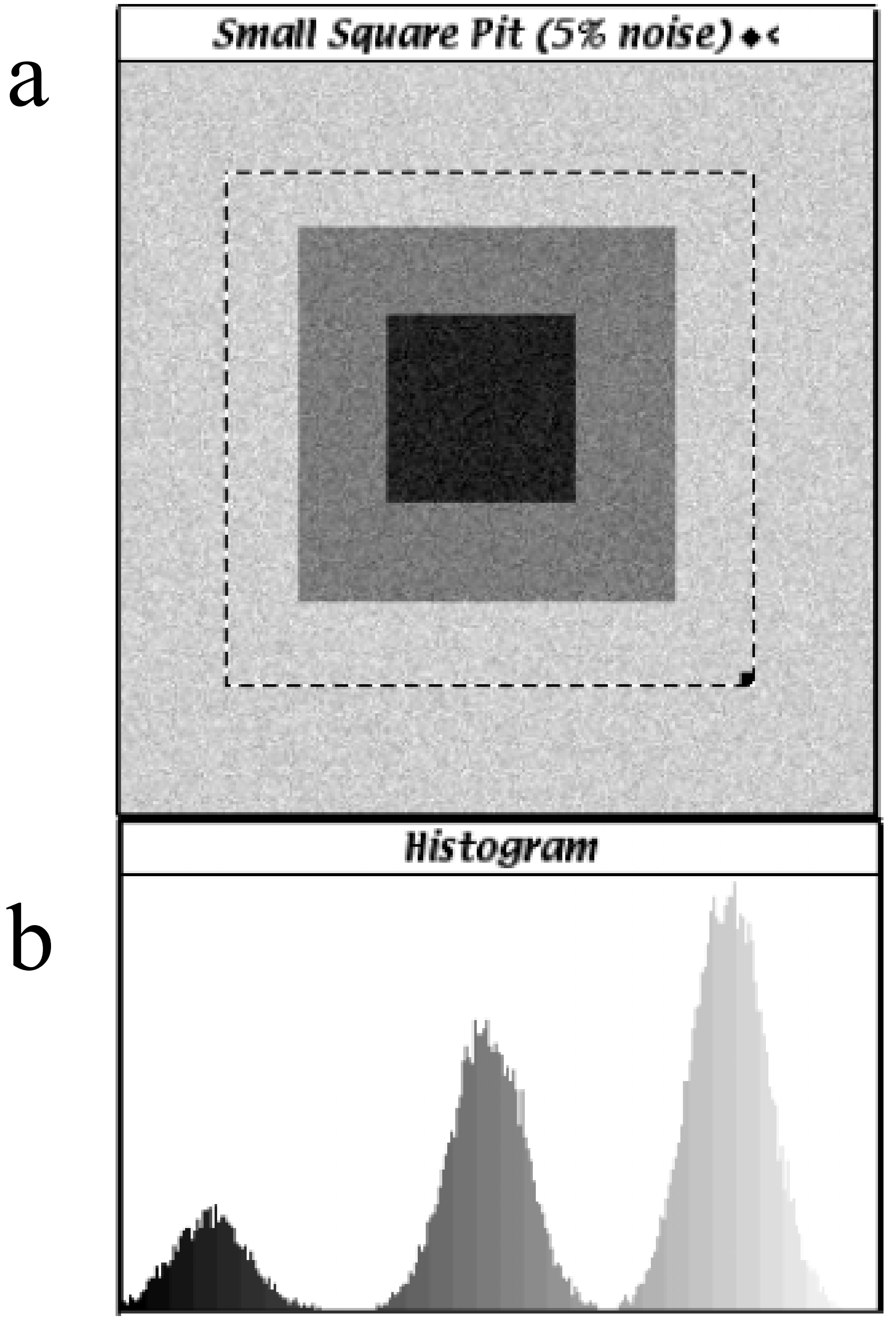

Figure 3-1. a) Synthetic AFM image of two concentric square pits, 1 µm and 2 µm on a side. The z-range of the image (white to black) is 100 nm, and the three terraces are located at 11, 48, and 81 nm. Random noise has been added to the image in a normal distribution about the original pixel values. The dashed line indicates the ROI upon which the macro calculations were performed. b) Histogram of the number of pixels within the ROI corresponding to each grey level. Both a) and b) are digital captures of windows in the Image SXM program, taken during the measurement procedure.

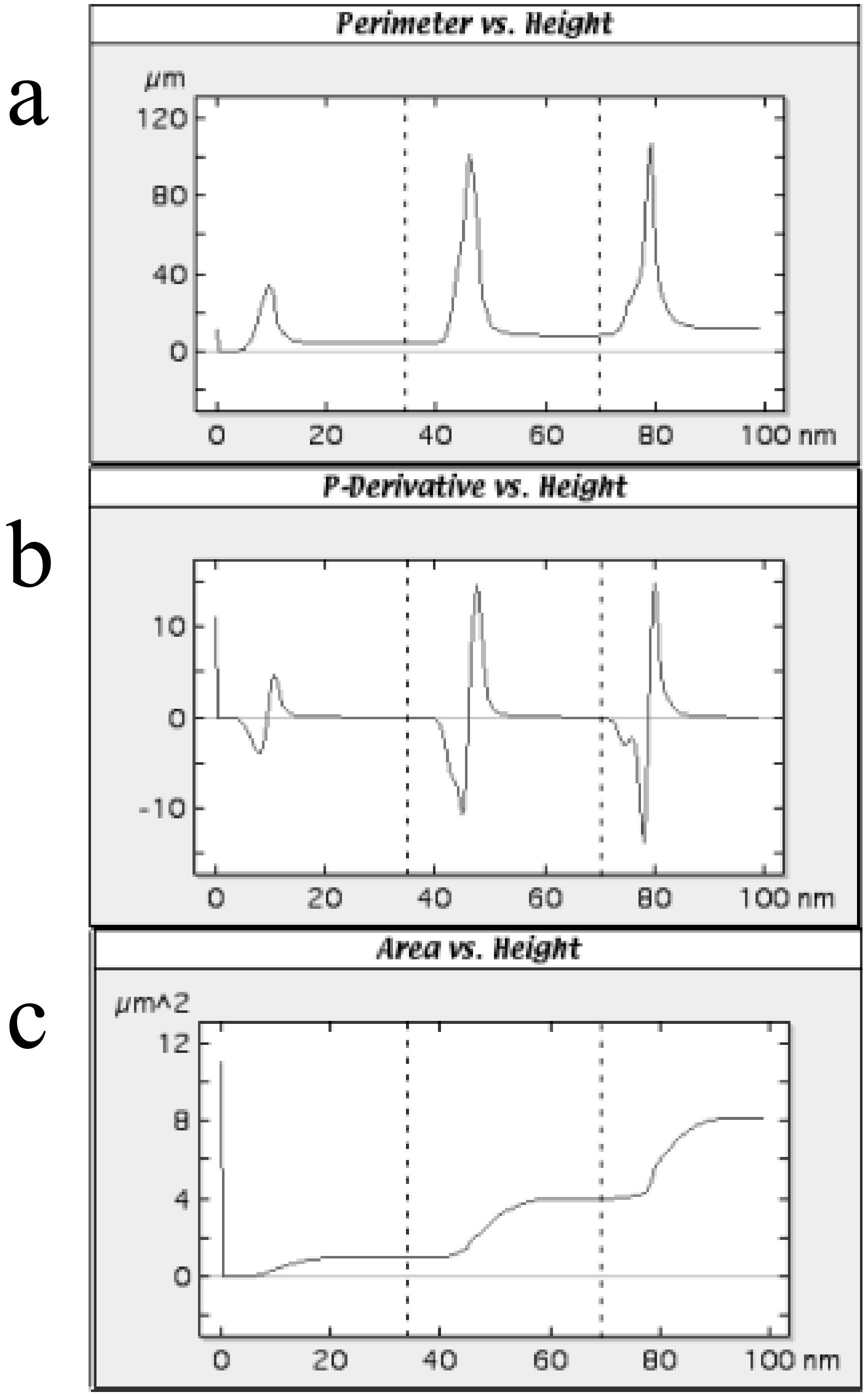

Figure 3-2. a) Plot of perimeter vs. threshold height for the calculations performed on the ROI in figure 1a. Dashed lines represent the threshold heights the program picked as ideal levels to measure perimeter and area. b) Plot of perimeter derivative vs. threshold height. c) Plot of area vs. threshold height. a), b), and c) are digital captures of windows in the Image SXM program, taken during the measurement procedure, with the dashed lines being added afterward.

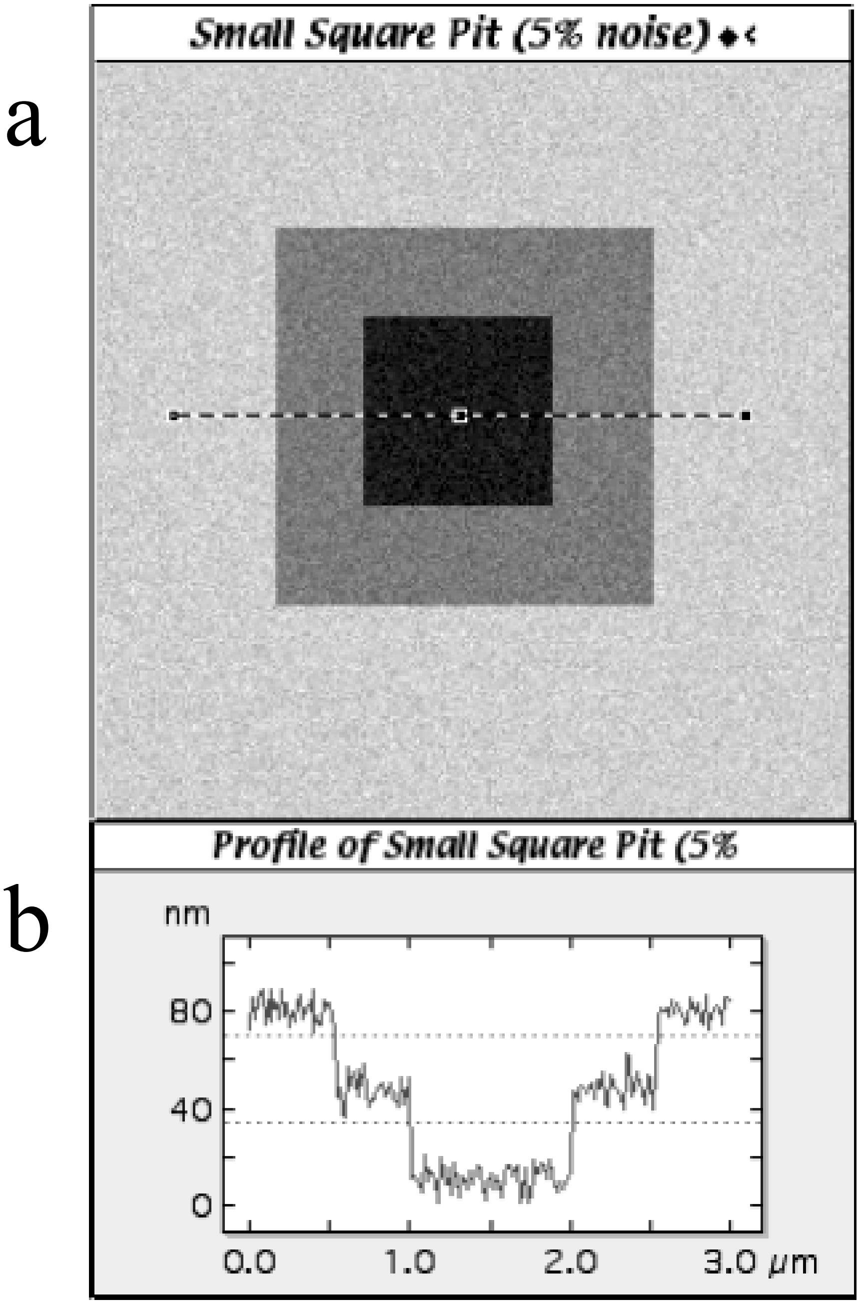

Figure 3-3. The dashed line in a) denotes the area from which the data for the cross section of the square pits plotted in b) is taken. Both a) and b) are digital captures of windows in the Image SXM program, taken during the measurement procedure, with the dashed lines in b) being added afterward.

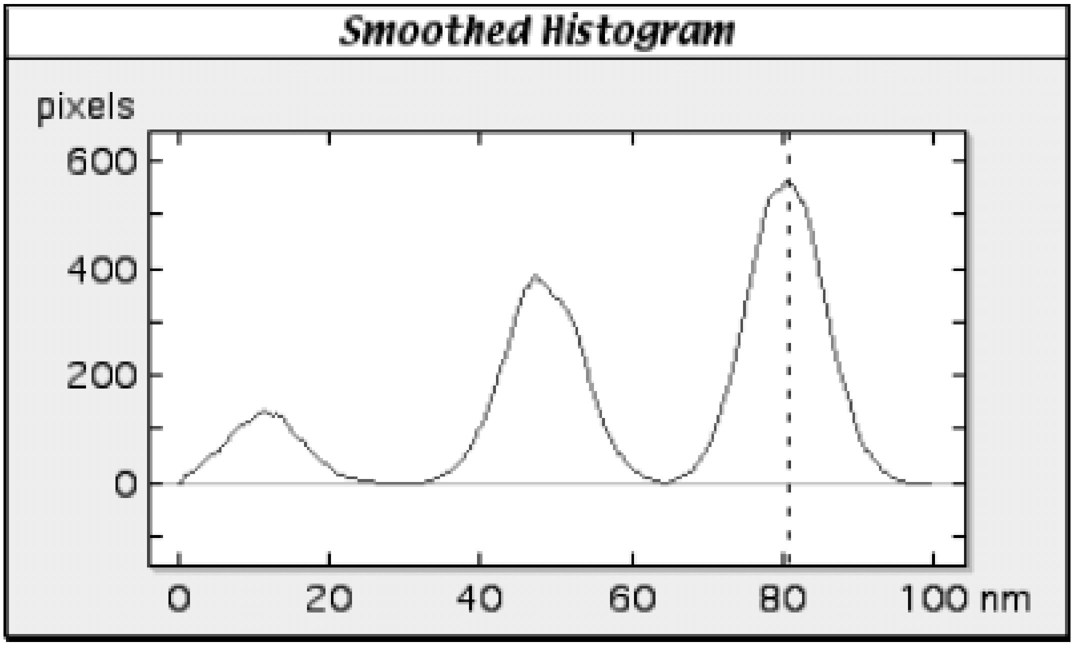

Figure 3-4. Plot of the same histogram as in figure 1b, after being subjected to a five point smoothing routine. The "Pit Volume" macro generated the smoothed histogram, and used it to calculate the "baseline" height (dashed line) from which to calculate the volume of the pits. This figure is a digital captures of the data plot window in the Image SXM program, taken during the measurement procedure, with the dashed line being added afterward.

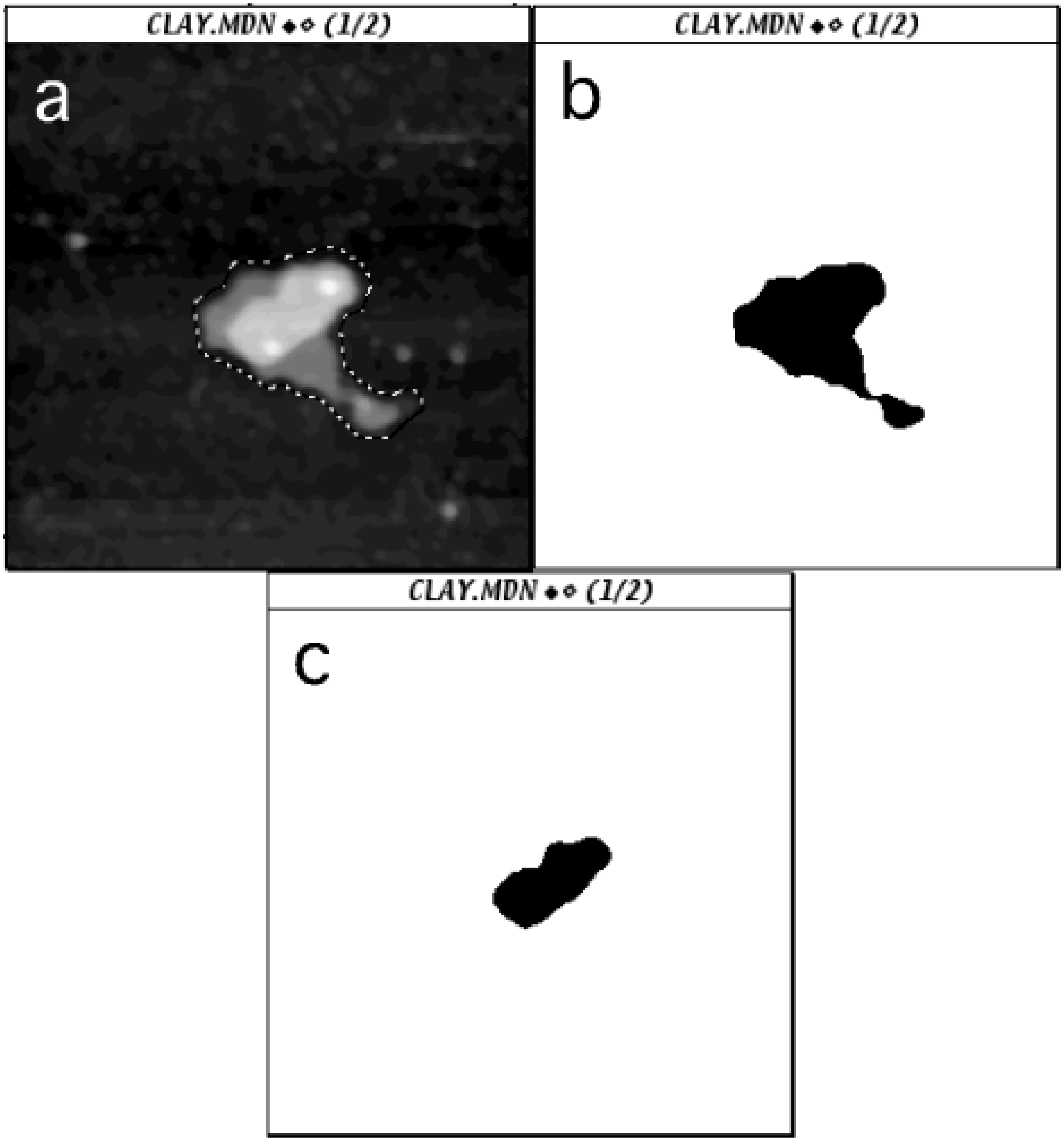

Figure 3-5. a) 1.7 x 1.7 µm AFM image of a montmorillonite clay particle under deionized water. The particle has well-defined terraces at ~8 and ~14 nm height, with the baseline at ~2 nm. The dashed line represents the ROI used for the measurement routines. b) Binarized version of a), thresholded at 6.7 nm, the first level picked by the perimeter/area measurement routine. c) Thresholded at 12.9 nm, the second level picked. a), b), and c) are digital captures of image windows in the Image SXM program, taken during the measurement procedure.

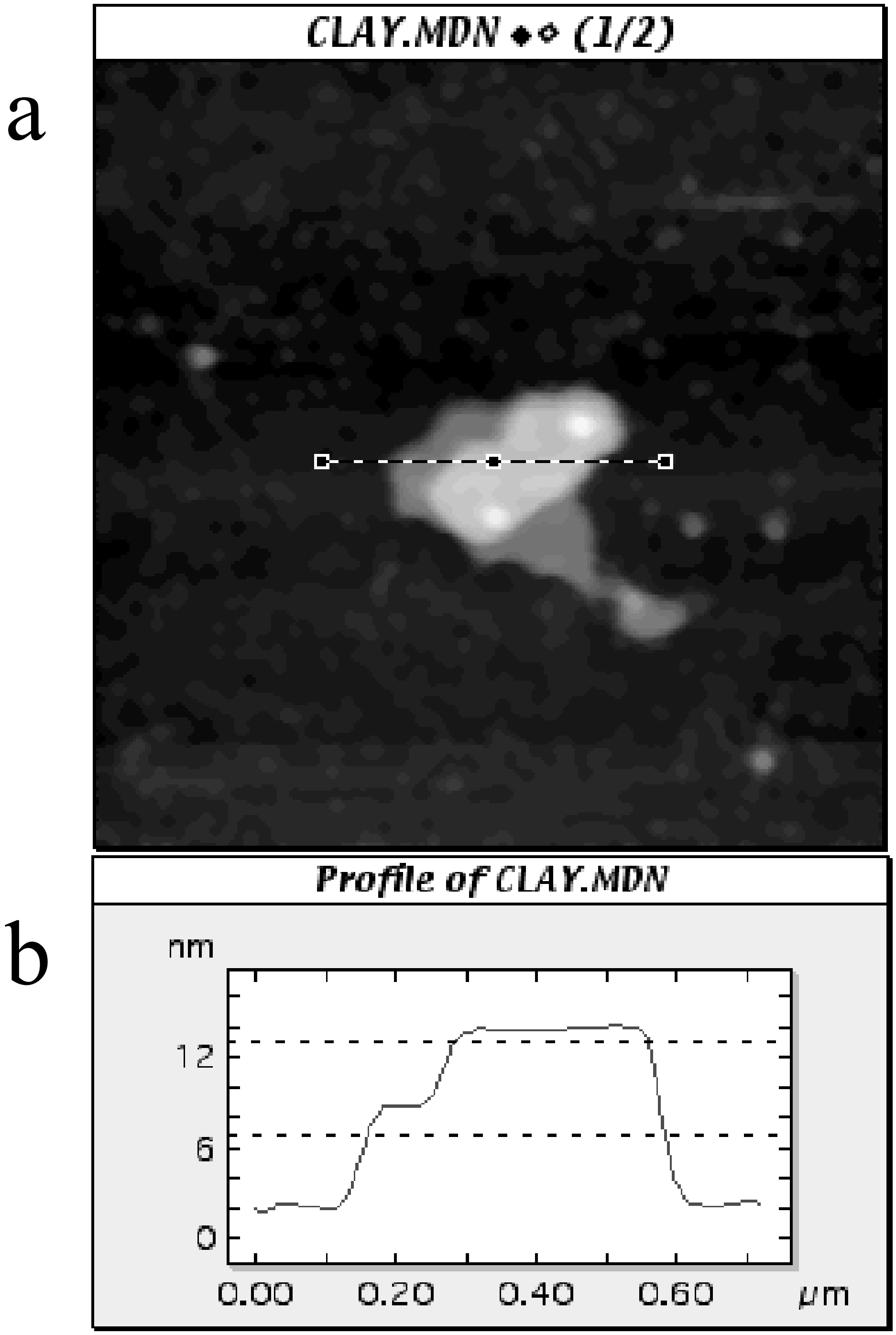

Figure 3-6. The dashed line in a) denotes the area from which the data for the cross section of the montmorillonite clay particle plotted in b) is taken. The dashed lines in b) indicate the threshold levels at which the perimeter and area were measured. Both a) and b) are digital captures of windows in the Image SXM program, taken during the measurement procedure, with the dashed lines in b) being added afterward.

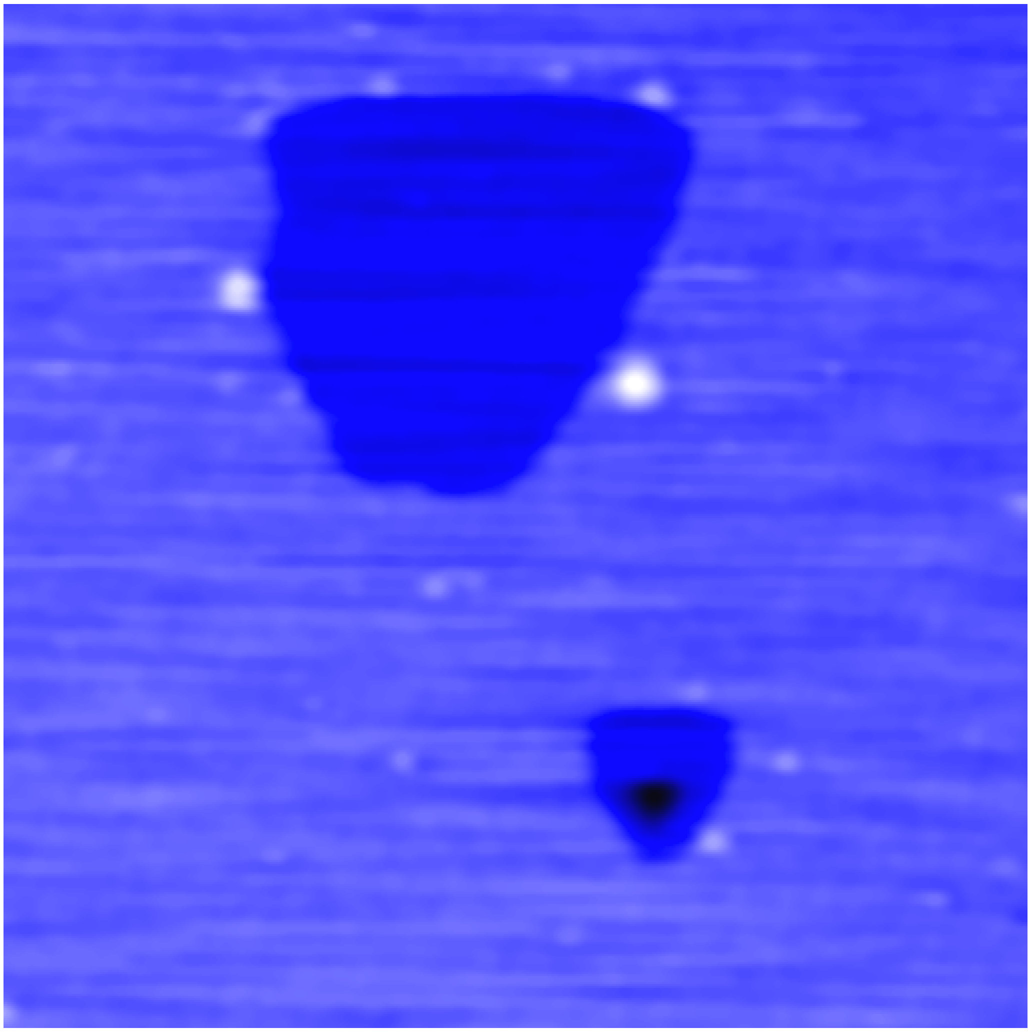

Figure 3-7. Animation of a sequence of four 880 nm x 880 nm AFM images of the surface of a phlogopite mica crystal, taken under pH 2 HCl. The surface was pre-etched with HF, and the images were taken at 0 hrs., 14 hrs., 39 hrs., and 63 hrs. The perimeter and area of the large, 1 nm deep pit at the top of the image were measured through the sequence to determine the volume change of the pit over time. Click on the frame to play the animation, and again to stop.

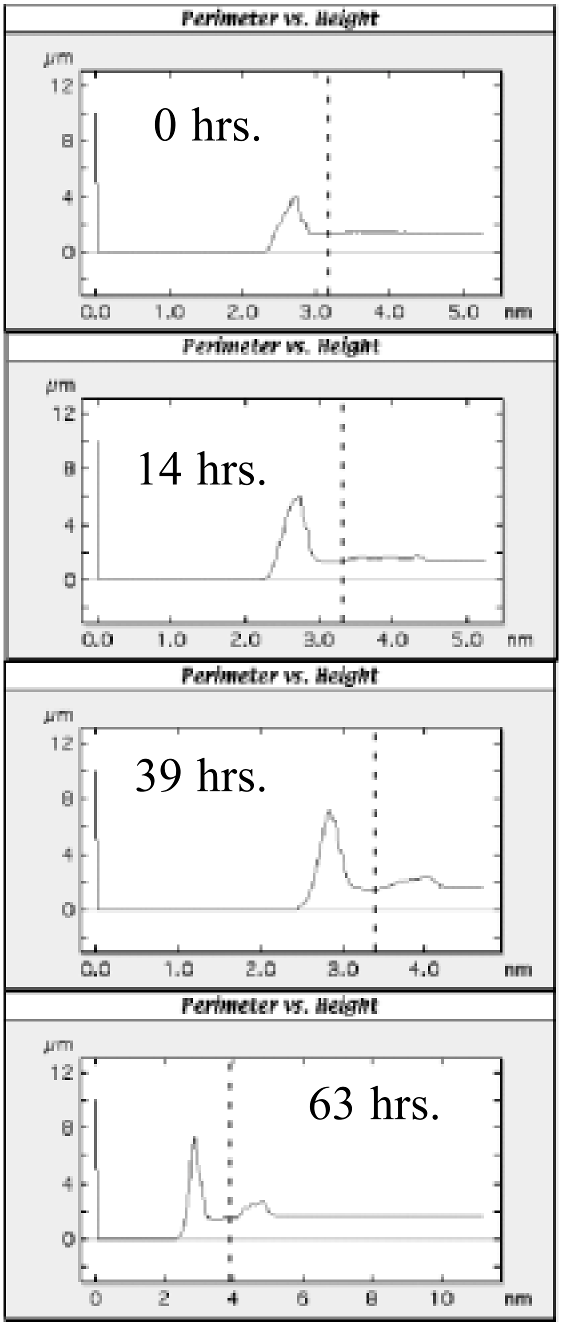

Figure 3-8. Perimeter vs. threshold height plots for the large etch pit near the top of each of the frames in figure 7. Dashed lines indicate the threshold height at which perimeter and area were measured. Clearly the baseline height of the images, and hence the “absolute” height of the ideal measurement threshold vary from frame to frame, due to changing imaging conditions, image drift, etc. However, the flat terrace in the perimeter vs. threshold height plots, corresponding to the edges of the pit, is clearly recognizable in each. a), b), c), and d) are digital captures of data plot windows in the Image SXM program, taken during the measurement procedure, with the dashed lines being added afterward.

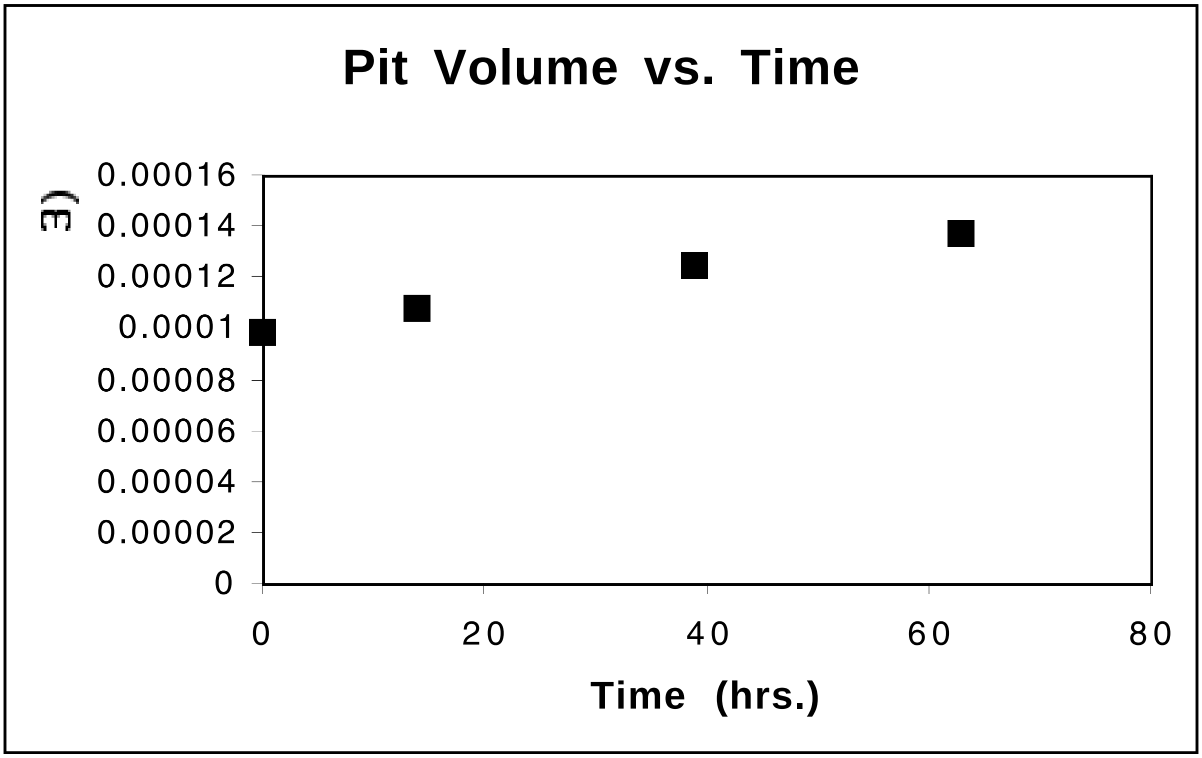

Figure 3-9. Volume vs. time plot for the large pit near the top of the frames in figure 7. The volume was calculated by multiplying the area of the pit by the 1.0 nm step height.

Chapter 4: Edge surface area normalized dissolution rates of biotite and montmorillonite

Introduction

Measurements of mineral dissolution rates have usually been normalized either to BET or geometrically derived surface areas, although it has repeatedly been pointed out that since reactive sites are not necessarily homogeneously distributed on a mineral surface, the total surface area may not be proportional to their number (e.g. Helgeson, 1971; Casey *et al.*, 1988; Hochella, 1995; Brantley and Chen, 1995; Koretsky *et al.*, 1998; Rufe and Hochella, 1999; Bosbach *et al.*, 2000). An excellent example of this phenomenon is provided by the 2:1 phyllosilicates, which have highly anisotropic crystal structures. The majority of the surface area of 2:1 phyllosilicates is normally composed of prominent (001) faces terminated on extremely stable, and hence unreactive, siloxane surfaces. The edge surfaces, on the other hand, are normally terminated by broken strong bonds, and tend to be much more reactive than the basal surfaces (White and Zelazny, 1988; Anderson and Sposito, 1991; Zachara and McKinley, 1993; Bleam, 1993; Turpault and Trotignon, 1994; Charlet *et al.*, 1993; Brady *et al.*, 1996; Rufe and Hochella, 1999; Schlegel *et al.*, 1999; Bosbach *et al.*, 2000; Bickmore *et al.*, 2000). For instance, it is generally accepted that during the early stages of acid hydrolysis, 2:1 phyllosilicates essentially dissolve exclusively at the edge surfaces (Turpault and Trotignon, 1994; Kaviratna and Pinnavaia, 1994; Rufe and Hochella, 1999; Bosbach *et al.*, 2000; Bickmore *et al.*, 2000).

Although the 2:1 phyllosilicates are structurally and chemically very similar to each other, dissolution rates obtained for 2:1 clay minerals, like montmorillonite and illite, in bulk dissolution experiments have often been much slower than rates for other 2:1 sheet silicates, like micas, where larger size fractions were available for study (Nagy, 1995). In this paper we show that the edge surface area (A_e) normalized dissolution rates for several 2:1 phyllosilicates are all very similar, and provide evidence that dissolution rates of clay minerals like montmorillonite measured from solution chemistry may have been depressed due to colloidal effects. This has been accomplished using a newly developed technique for examining clay mineral particles under aqueous solutions by atomic force microscopy (AFM) (Bickmore *et al.*, 1999a).

The dissolution of 2:1 phyllosilicates is an important weathering reaction, and contributes to such processes as the neutralization of acids in the environment and the cycling of soil nutrients. The kinetics of such reactions are also important for acid treatments of oil well bores to locally increase the permeability of reservoir rocks (Eslinger and Pevear, 1988). However, given the difference in reactive surface area and colloidal behavior of different size fractions of these minerals, as well as the differences in the local environments and flow conditions in which they occur, the difficulty inherent in applying macroscopically-derived dissolution rates is apparent. Therefore, the establishment of the kind of baseline rates discussed here may be an essential step in the full description of 2:1 phyllosilicate dissolution kinetics.

Materials and Experimental Methods

Samples and Sample Characterization

Macroscopic crystals of a ferrian biotite (Faraday Twp., Ontario, Canada) were broken up, and then wet ground in a heavy-duty blender for 30 min. The ground sample was dried and sieved to separate out particles larger than 0.5 mm. The ≤ 0.5 mm size fraction was then wet ground for 12 min. in a McCrone micronizing mill (McCrone Scientific Ltd., London, United Kingdom) to produce a large proportion of clay-size particles without inducing a great number of structural defects (Stephens and Tuddenham, 1971; O'Connor and Chang, 1986; Puledda and Paoletti, 1994). The <2 μm fraction of the ground sample was then separated by centrifugation. An oriented mount of the biotite clay was prepared on ceramic tile for powder X-ray Diffraction (XRD) analysis (Rich, 1969), and K-saturated. Amorphous material and secondary phases were not detected in the diffraction pattern (Fig. 1). The chemical formula for the biotite ($(K_{1.95}Na_{0.05})(Al_{0.54}Fe^{3+}_{0.45}Fe^{2+}_{2.94}Mn_{0.12}Mg_{0.62})(Si_{5.67}Al_{2.33})O_{20}(OH)_{2.83}F_{1.15}Cl_{0.02}$), was obtained by analysis of macroscopic flakes with a Cameca SX-50 electron microprobe (Cameca Instruments, Trumbull, Connecticut). The unit cell dimensions used to calculate the molar volume of ferrian biotite (*a*=5.335 Å, *b*=9.239 Å, *c*=10.172 Å, β= 100.11°) were taken from Bailey (1984).

A sample of Wyoming montmorillonite (Source Clays Repository, sample SWy-1) was crushed, and the <2 μm size fraction separated by centrifugation. The clay fraction was then acid washed four times in 0.001 M HCl and Na-saturated. A chemical formula for SWy-1 ($Na_{1.12}(Al_{2.94}Ti_{0.23}Fe^{3+}_{0.32}Fe^{2+}_{0.03}Mg_{0.58})Si_{8.00}O_{20}(OH)_2$) was recalculated based on a 22 O unit cell from data in van Olphen and Fripiat (1979). High resolution thermogravimetric analysis (HRTGA) of the sample (see Fig. 2), using a TA Instruments (New Castle, Delaware) Hi-Res 2950 Thermogravimetric Analyzer, revealed no secondary phases (cf. Koster van Groos and Guggenheim, 1990; Bish and Duffy, 1990). Unit cell dimensions used to calculate the molar volume of montmorillonite (*a*= 5.2 Å, *b*= 9.15 Å, *c*= 10.0 Å, β= 100°) were taken from Deer *et al.* (1992).

Clay Immobilization

The clays were immobilized for *in situ* AFM analysis using variations on one of the techniques described by Bickmore *et al.* (1999a). Polyethyleneimine (PEI) ($(C_2H_5N)_n$, M.W. 1800, Polysciences, Warrington, Pennsylvania) was diluted 1:500 by volume. A small disc of freshly-cleaved muscovite was taped with double-sided tape to a similarly-shaped steel AFM sample puck and immersed in the PEI suspension for ~30 s. The muscovite was then rinsed with a stream of deionized water for 5 min and dried in a 90°C oven for 20 min. A dilute suspension of the clay in deionized H_2O (~0.2 mg clay per 20 ml) was prepared and then dispersed for 1-2 min. with an Artek sonic dismembrator (Dynatech Laboratories, Chantilly, Virginia, model 300) set at ~150 Watts. The dried PEI-coated muscovite was immersed in the clay suspension for 1 min, and then blown dry with a stream of compressed air.

AFM Imaging of the Dissolution Reaction

Imaging of the clay mineral particles was performed in the fluid cell of a MultiMode atomic force microscope (Digital Instruments, Santa Barbara, California), using oxide-sharpened Si_3N_4 tips. Bosbach *et al.* (2000) reported that force–distance curves showed a large attractive peak due to the presence of the PEI coating, whereas on clean mica surfaces in aqueous solution there were not such strong adhesive interactions with the AFM tip. The strong attraction between the AFM tip and the PEI-coated mica substrate resulted in a tip loading force of about 50 – 100 nN, and therefore some clay particles were stripped from the surface during the course of the experiments. Tip-sample interaction can result in enhanced dissolution rates of monolayer steps (Park et al., 1996), and while Bosbach *et al.* (2000) reported that they could detect no relationship between scan speed or AFM feedback control parameters and particle edge dissolution rates for hectorite, Bickmore *et al.* (2000) found that the dissolution rate of nontronite was significantly enhanced by contact mode imaging. Therefore, in this study the dissolution experiments were performed using TappingMode atomic force microscopy (TMAFM), which results in a much weaker tip-sample interaction (Hansma *et al.*, 1994; Johnson, 1995).

Clay particles immobilized on the PEI-coated substrate were first imaged under deionized water, after which HCl solution was injected into the cell. Images were then periodically captured to track the progress of the particle dissolution. Fresh HCl solution was also injected into the cell on average every ~30 min. to avoid the buildup of reaction products in the cell solution. No secondary precipitates were observed during the experiments.

The HCl solutions used were pH 1.0, 1.5, and 2.0. Solutions with higher pH levels were not used, because preliminary experiments indicated that the dissolution reactions were too slow to measure during the time scale of the experiments (up to several hours). Longer experiments could not be performed because the clay particles would not stay stably fixed to the substrate for more than several hours.

The AFM images (see Fig. 3) are constructed from height data, and were subjected to the flattening routine (a *least-squares* polynomial fit to remove unwanted features from the scan lines) included with the Digital Instruments software. Several repetitions of a 3x3 or 5x5 median filter were also applied to the images to remove random noise (Russ, 1995).

Clay Particle Measurement

Analysis of features in the images was accomplished using the freeware Image SXM image analysis program (Barrett, 1997), custom modified with a suite of macros designed for the measurement of the perimeter, horizontal area, and volume of discrete features in AFM images (Bickmore *et al.* 1999b).

It was necessary to extract dissolution rates for single 2:1 phyllosilicate particles normalized to A_e from the AFM time series data, taking into account the fact that edge surface area may change over time. To obtain these rates, the perimeter and horizontal area of each particle in a time series of images were measured at an optimum height near its base. Both values were multiplied by the unit cell height (d_{001}) of the mineral to obtain the A_e and volume of a unit cell thick slice of the particle over time. Where the automated algorithms were not sufficient (usually with very thin particles), a Sobel edge detection algorithm (Russ, 1995) was applied to the image, and the perimeter and area of the particles were measured with the polygon measurement tool in Image SXM.

Rate Calculations

In order to take into account the changing A_e of the particle slices, they were mathematically treated as plates shrinking from their edges. It can be shown that the A_e of any plate shape is related to its volume by

$$A_e = bV^{1/2} \tag{1}$$

where b is some constant unique to each shape, and V is the volume of the plate. (That b is constant for a particular shape, regardless of size, is readily seen for simple examples like circular or square plates. In the case of a circular plate, $b = 2\sqrt{h\pi}$, and in the case of a square plate, $b = 4\sqrt{h}$, where h is the height of the plate.) If we assume a first-order rate law with respect to A_e, then

$$\frac{dn}{dt} = kA_e = kbn^{1/2}V_m^{\ 1/2} = Cn^{1/2} \tag{2}$$

where n is the number of moles mineral present in the slice, t is time, k is the zero-order dissolution rate constant, V_m is the molar volume of the mineral, and C is a constant, where

$$C = kbV_m^{1/2}. \tag{3}$$

The value of b was calculated by plotting A_e vs. $V^{1/2}$ for a time series of a slice of a dissolving particle, and obtaining the slope of a linear regression of the data, forced through the origin. This approach implicitly assumes that the shape of the particle stays relatively constant during the dissolution process, but this turns out to be a fairly good assumption, given that the regressions of the A_e vs. $V^{1/2}$ data usually produced excellent fits (see Fig. 4).

The next step was to obtain a value for C. Rearranging equation (2), we find,

$$\frac{dn}{n^{1/2}} = Cdt\,. \tag{4}$$

Integrating

$$\int_{n_0}^{n} \frac{dn}{n^{1/2}} = C\int_0^t dt \tag{5}$$

(where $n_0 = n$ at $t = 0$) and rearranging, we obtain

$$Ct = 2n^{1/2} - 2n_0^{\;1/2}. \tag{6}$$

C can be obtained by plotting ($2n^{1/2} - 2n_0^{\;1/2}$) vs. t for a time series of a dissolving particle slice, and obtaining the slope of a linear regression of the data, forced through the origin.

The predicted values of *n* over time were obtained by rearranging equation (6) to obtain

$$n = \left(\frac{Ct + 2n_0^{1/2}}{2}\right)^2. \tag{7}$$

The approach outlined above necessarily forces the predicted *n* values through n_0,, so in order to produce a better fit of the data, the calculated value of *C* and the measured value of n_0 were used as first approximations, and then both terms were varied using the "solver" function in Microsoft Excel to obtain a least-squares best fit of the data (see Fig. 5). The dissolution rate, *k*, was then calculated by rearranging equation (3) to obtain

$$k = \frac{C}{bV_m^{1/2}} \tag{8}$$

utilizing the optimized value of *C*.

The rates obtained from the measurements on all particles were averaged for each mineral at each pH level. There was often considerable scatter in the data points--more than an order of magnitude—and in fact some particles dissolved too slowly to measure any dissolution during the time scale of the experiments. Therefore, where no significant dissolution was observed, a dissolution rate of 0 was recorded and averaged with the rest of the data points at each pH level.

Results

The measured dissolution rates for biotite and montmorillonite are reported in Table 1. Meaningful rate data were collected up to pH 2.0 for biotite and pH 1.5 for montmorillonite. Given the size range of the particles measured, the amount of uncertainty in the measurements, and the time scale of these experiments, we estimate that the lowest measurable A_e-normalized rate for these particles would be ~2 x 10^{-9} mol/m^2•s. Rufe and Hochella (1999) were able to measure dissolution rates for phlogopite etch pits on the order of ~10^{-10} mol/m^2•s because they were able to run experiments for several days, rather than a few hours. Consistent with this, preliminary experiments on phlogopite and nontronite clay particles, conducted for this study, revealed no measurable dissolution.

The data collected at pH 1.0, 1.5, and 2.0 for biotite show no consistent trend, but the error bars for all three data points collected overlap. Indeed, the error bars for the montmorillonite dissolution rate data at pH 1.0 and 1.5 overlap each other, and overlap the error bars for the biotite dissolution rates reported here. Therefore, this sort of microscopic data is not likely to be useful for establishing pH dependence, but it should be useful to constrain the A_e-normalized dissolution rates within certain limits. In the cases of the samples examined here, we may estimate the rates at ~10^{-8} mol/m^2•s.

Discussion

Comparison with other A_e-normalized rates

A_e-normalized dissolution rates of 2:1 phyllosilicates in the pH range of interest (pH 1-2) can be taken from three other studies for comparison (see Fig. 6). (All rates are reported here in mol/m^2•s, based on a 22 O unit cell for each mineral.) First, Turpault and Trotignon (1994) performed dissolution experiments on sized single crystals of biotite, with varying amounts of edge and basal surface area, in pH 1.08 HNO_3. Their data has been recalculated to obtain an A_e-normalized rate of 4.5 ± 3.5 x 10^{-8} mol/m^2•s (95% confidence). (Malmström and Banwart (1997) report a personal communication with L. Trotignon, indicating that the data reported by Turpault and Trotignon had been shifted upward by a factor of 10. This has been taken into account in our recalculation.) Second, Rufe and Hochella (1999) performed *in situ* TMAFM on phlogopite etch pits at pH 2.0, and reported an A_e-normalized dissolution rate of 3.7 ± 1.4 x 10^{-10} mol/m^2•s (95% confidence, error recalculated for this study). Third, Bosbach *et al.* (2000) performed *in situ* AFM (contact mode) on hectorite (a trioctahedral, magnesian smectite), and reported an A_e-normalized rate of 7.3 ± 4.5 x 10^{-9} mol/m^2•s (95% confidence).

At pH 2.0, the dissolution rate for biotite reported here (8.2 ± 4.4 x 10^{-9} mol/m^2•s) is statistically indistinguishable from the rate reported by Bosbach *et al.* (2000) for hectorite (7.3 ± 4.5 x 10^{-9} mol/m^2•s). One would expect the dissolution rates of trioctahedral 2:1 phyllosilicates to be similar, but the pH 2.0 rates for biotite and hectorite are ~21-22x faster than that reported by Rufe and Hochella (1999) for phlogopite. However, reported pH 2.0 dissolution rates measured by solution chemistry (Kalinowski and Schweda, 1996; Malmström and Banwart, 1997) show that biotite dissolves ~3.6-7.4x faster than phlogopite. Furthermore, Rufe and Hochella (1999) measured the dissolution rates of nearly euhedral etch pits, and Bosbach *et al.* (2000) found that broken hectorite edges appeared to dissolve ~6x faster than euhedral edges. Therefore, it can be estimated that the A_e-normalized dissolution rate of biotite, measured from dissolving ground particles, ought to be ~22-44x faster than that measured for the dissolution of euhedral phlogopite etch pits, in good agreement with observation.

The measured rate of biotite dissolution at pH 1.0 (6.1 Ò3.0 x 10^{-9} mol/m^2•s) is only ~7.5x slower than that calculated from the data of Turpault and Trotignon (1994) at pH 1.08 (4.5 ± 3.5 x 10^{-8} mol/m^2•s), and in fact, the error bars for the two rates nearly overlap. In addition, Turpault and Trotignon admittedly underestimated A_e for their sized biotite crystals by calculating it geometrically, so a more accurate estimate of A_e for their samples would likely render the two rates statistically indistinguishable. This close correspondence is impressive given that completely different experimental methods were used to extract the rates.

The montmorillonite dissolution rates reported here (pH 1.0: 1.2 Ò0.5 x 10^{-8} mol/m^2•s; pH 1.5: 8.9 Ò4.8 x 10^{-9} mol/m^2•s) are also statistically indistinguishable from the biotite and hectorite rates. At first glance this might seem unexpected since montmorillonite is dioctahedral, and dioctahedral muscovite mica has been observed to dissolve ~100x more slowly than biotite

(Kalinowski and Schweda, 1996). However, Bickmore *et al.* (2000) showed, based on *in situ* AFM observations of nontronite dissolution, that dioctahedral phyllosilicates dissolve much more quickly at defect sites and broken edges than at euhedral edges. Reaction fronts at defects and broken edges dissolve quickly until becoming pinned along the directions of the euhedral edge faces. This was explained in terms of the availability of reactive sites at these edges, i.e. underbonded oxygens connecting the octahedral and tetrahedral sheets. Therefore, a well-crystalline dioctahedral mineral such as muscovite would likely dissolve very slowly, since the reaction front would stabilize along euhedral surfaces. However, a poorly-crystalline dioctahedral mineral like montmorillonite would likely dissolve much more quickly, since the crystal form is anhedral, and the structure has abundant defects.

Comparison with dissolution rates measured from solution chemistry

It is also useful to compare the A_e-normalized dissolution rates measured for the biotite and montmorillonite samples to dissolution rates for these minerals measured from solution chemistry. Given the state of knowledge about the dissolution process of these minerals in acid solutions, the differences in the rates may then be rationalized in terms of the rate-controlling factors.

Biotite

In order to compare A_e-normalized rates to most of those reported in the literature, which are usually normalized to some measure of the total mineral surface area, an estimate of the proportion of A_e to the total surface area must be made. In the case of biotite, only Turpault and Trotignon (1994) reported both the total surface area and A_e of the macroscopic biotite flakes they dissolved. In their case, the proportion of A_e ranged from 0.1 to 11% (average ~1.2%), although they likely underestimated A_e. Kalinowski and Schweda (1996) ground their biotite sample in a micronizing mill and noted that SEM characterization of the ground material "revealed that the major fraction consisted of particles with about 10-20 µm edge length and very much smaller thickness." Sutheimer *et al.* (1999) used AFM to measure the aspect ratio of kaolinite (a 1:1 phyllosilicate clay mineral) and estimated the proportion of edge surface area at ~17-22%. However, kaolinite clay particles are neoformed and are often relatively thick for a clay mineral, whereas grinding tends to shear phyllosilicates preferentially along basal planes (Acker and Bricker, 1992), so ground particles of biotite would likely tend to be thinner. Given the above information, we estimate the proportion of A_e for the biotite samples used in the studies considered here to be no more than ~10%, for the purpose of comparison with our A_e-normalized rate data.

The A_e-normalized biotite dissolution rates obtained in this study are ~75-400x the BET surface area normalized rates reported by Kalinowski and Schweda (1996) and Malmström and Banwart (1997) for comparable pH levels (Fig. 7). Assuming an A_e of 10% of the total surface area, a difference of only 10x can be explained by the normalization to different measures of surface area. However, biotite is known to dissolve with a high initial rate, and the experiments reported here lasted only up to several hours. The A_e-normalized rate (pH 1.08) recalculated from the data of Turpault and Trotignon (1994) is very similar to the pH 1 rate reported here, and should also be interpreted as an "initial" rate. Their experiments lasted only 75 h and rates were calculated using the total Si released in a batch reactor in the final solution.

Kalinowski and Schweda (1996) list four reasons for time dependence of dissolution rates. First, crushed particles may have a high density of high energy sites on the surface. Second, ultrafine particles not removed after crushing may dissolve preferentially. Third, the reactive surface area may change over time during the dissolution process. Fourth, nonstoichiometric dissolution is known to create a leached layer at the edges of biotite particles, and diffusion of ions through this layer may control the reaction rate. Given that the rates reported here were calculated with respect to single dissolving particles and normalized to A_e, the preferential dissolution of ultrafine particles is not applicable. Similarly, while the reactive surface area of biotite particles certainly may change during the course of the dissolution reaction, such a change would not be anywhere near the magnitude needed to explain the differences in the rates discussed here. No doubt there are a higher abundance of "strained" sites on the surfaces of ground biotite particles, and this factor likely had some effect, at least initially. However, the primary factor responsible for the depression of the dissolution rates measured from solution chemistry relative to the A_e-normalized rates reported in this study, is likely the development of leached layers around the edges of the biotite particles in the longer term solution studies.

In the case of biotite, interlayer K and octahedral cations are preferentially dissolved from the edges of the particles in acid solutions, leaving a silica-rich leached layer. These leached layers can grow quite large, e.g. Turpault and Trotignon (1994) altered a macroscopic flake of biotite in pH 1.08 HNO_3 for 8 months, and found an altered zone ~500 µm thick around the edge. The outer ~100 µm appeared to be completely leached, hydrated silica. After only 28.5 h, the altered zone on another biotite flake was ~50 µm thick. On the other hand, the biotite particles dissolved in conjunction with this study were all <2 µm in diameter, so any leached layers that could have formed on their edges would necessarily have been much smaller than those formed on larger particles like the 10-20 µm diameter grains studied in Kalinowski and Schweda's (1996) experiments. Consequently, even if the experiments reported here had been of much longer duration, A_e-normalized dissolution rates of clay-size biotite particles would probably never be as slow as those measured for much larger particles.

There is reason to believe that the rate of leaching controls the dissolution rate of 2:1 phyllosilicates, even with respect to Si release. For example, the mica minerals biotite, phlogopite, and muscovite all have essentially identical tetrahedral sheets, with 6 Si and 2 Al per formula unit. However, muscovite dissolution rates normalized to Si release are nearly 2 orders of magnitude slower than biotite dissolution rates (Kalinowski and Schweda, 1996). Since muscovite dissolves nearly stoichiometrically, while biotite can develop large leached rims, it may be inferred that the Si in the leached material is more soluble than that in the pristine mineral. Therefore, the rate of octahedral leaching must control the rate of Si release, and the rate of leaching is very likely controlled by diffusion of ions through the leached layer.

If diffusion through the leached layer is the rate-controlling factor in biotite dissolution over the long term, the release rates of the various elements in biotite need to be characterized in terms of the particle size distribution and proportion of edge surface area. Until some attempt is made to accurately estimate these parameters, we can expect very little progress to be made in modeling biotite dissolution and similar reactions.

Montmorillonite

In the case of montmorillonite, we can directly compare the rates reported here with those obtained in the experiments of Zysset and Schindler (1996), who dissolved an identical sample (SWy-1), saturated with K$^+$, over a range of pH. Their data has been recalculated in terms of mol/m^2•s, normalized to total surface area as measured with the EGME method (661.5 m^2/g, Eltantawy and Arnold, 1973) Techniques such as EGME measure both the outer and interlayer surface area of expanding clays, whereas BET measures the outer surface area of clay tactoids. Since the distribution of clay platelets, and hence the BET surface area, can vary drastically with factors such as cation saturation (Rutherford *et al.*, 1997), and may have no relationship to the distribution of particles in suspension, BET surface areas are of little use for expanding clays like montmorillonite. At pH 1.0, the montmorillonite dissolution rate reported here (1.2 Ò0.5 x 10^{-8} mol/m^2•s) is ~26,000x faster than that reported by Zysset and Schindler (1996) for SWy-1 in pH 1.0, 0.03 M KCl solution (4.6 x 10^{-13} mol/m^2•s). At pH 1.5, the rate reported here (8.9 Ò4.8 x 10^{-9} mol/m^2•s) is ~28,000x faster than the pH 1.5 rate reported by Zysset and Schindler (3.2 x 10^{-13} mol/m^2•s) (see Fig. 8).

The measured proportions of A_e to total surface area for the montmorillonite sheets measured in these experiments ranged from 0.2-2% (avg. 1%). This estimate is likely biased toward larger than average particles, however, so the true proportion of A_e may be higher. However, it seems unlikely that it would be any lower than 1%. Therefore, one might expect the rates to differ by only a factor of ~100x, if the difference in surface area normalization is the only factor taken into account.

With biotite, a rate difference of 7.5-40x was explained in terms of strained surface sites and the development of leached layers around the edges of reacting particles. However, in the case of montmorillonite, a rate difference of at least 260-280x cannot be explained in this way. First, while strained surface sites may have played a minor role in enhancing the A_e-normalized dissolution rate, the effect should have been less than for biotite. Whereas the biotite grains had been ground in a micronizing mill, the montmorillonite was gently crushed in a mortar and pestle, and the clay fraction separated by sedimentation. Second, Zysset and Schindler (1996) found the dissolution of montmorillonite to be very nearly congruent, so even if leached layers were formed around the edges of particles, the effect should not have been as pronounced as with biotite.

On the other hand, the depression of the montmorillonite dissolution rates as measured by solution chemistry can be explained by appealing to the colloidal behavior of the mineral. Under the solution conditions used by Zysset and Schindler (1996), the montmorillonite sample was very likely flocculated, and perhaps only the surface area available at the outside of the particle aggregates was effectively available for the dissolution reaction (cf. Hochella and Banfield, 1995). Zysset and Schindler dissolved their montmorillonite in solutions with a KCl background electrolyte concentration as low as 0.03 M, or 30 mM, and the sample was pre-saturated with K^+. Van Olphen (1992) reports that the onset of flocculation for a similarly dilute suspension of Na-saturated montmorillonite occurred at ~17 mM NaCl, which is less than the lowest concentration of KCl used by Zysset and Schindler (1996). However, K^+ is a significantly more effective flocculating agent than Na^+ (Neumann and Sansom, 1970). Furthermore, some of the experiments reported by Zysset and Schindler (1996) were reported earlier by Fürrer *et al.* (1993), who performed both batch and flow-through experiments. During the flow-through experiments, the montmorillonite sample was observed to form a gel inside the reactor, and the dissolution rates were observed to be depressed with respect to the batch experiments. Another point to note is that Nagy (1995) has recalculated the montmorillonite dissolution data of Heydemann (1966) over a large pH range (pH 3-10) at 25 °C, to obtain rates of ~10^{-15}-10^{-16} mol/m^2•s. These rates are 2-3 orders of magnitude slower than those reported by Zysset and Schindler (1996) under similar conditions, and perhaps Heydemann's samples were flocculated to a greater degree. Otherwise, it would be difficult to explain such a large difference in the dissolution rates by appealing to differences between the samples of montmorillonite. Clearly, the degree of flocculation can affect the dissolution rate of clay, and the montmorillonite samples used by Zysset and Schindler (1996) were most likely significantly flocculated. The same is suspected of the montmorillonite samples used by Heydemann (1966). Therefore, if this reaction is to be accurately modeled in nature, the aggregation conditions of the mineral must be taken into account.

Summary and Conclusions

A new technique has been used to track the dissolution of single, clay-size biotite and montmorillonite particles using *in situ* atomic force microscopy, in order to obtain dissolution rates normalized to edge surface area (A_e). Initial dissolution rates, normalized to A_e, have been measured for both minerals between pH 1-2. While these rates are not constrained well enough to be useful for assigning pH dependence, etc., they have been determined to be $\sim 10^{-8}$ mol/m^2•s, and therefore can be compared to the dissolution rates of these and other minerals reported in the literature. These rates compare very favorably to other A_e-normalized rates reported in the literature, but appear to be enhanced with respect to total surface area normalized rates measured from solution chemistry, even when the proportion of A_e is taken into account. In the case of biotite, this difference is easily explained by means of disturbed edge surfaces on the ground particles and the formation of leached layers at the edges, due to the preferential release of elements. However, the enhancement of the A_e-normalized montmorillonite rates is far too great to explain in this manner, especially considering that one would expect the effects of disturbed edges and leached layers to be much more pronounced for the ground biotite particles. This difference can be explained, on the other hand, if it is taken into account that the montmorillonite samples were very likely flocculated in the dissolution experiments reported in the literature.

These results graphically illustrate the need for careful estimation of the proportion of edge surface area and the aggregation conditions of 2:1 phyllosilicate samples during experiments aimed at determining dissolution rates. Both factors have been shown to bear directly on the problem of "reactive surface area," or the proportion of the mineral surface effectively available for the reaction of interest, and the dissolution reaction cannot be realistically modeled without taking them into account.

Acknowledgements

We thank Don Rimstidt for the montmorillonite sample. The biotite sample was provided by the Virginia Tech Museum of Geological Sciences (sample HB 1116). Theoretical assistance from Don Rimstidt and Chris Tadanier was especially helpful. BB, MH, and ER are grateful for the support of the National Science Foundation (EAR-9628023, EAR-9902996, and the Graduate

Student Fellowship program) and the Petroleum Research Fund administered by the American Chemical Society (ACS-PRF 31598-AC2). DB and LC are grateful for financial support by the Deutscher Akademischer Austauschdienst and the French Ministery of Foreign affairs.

References Cited

Acker, J.G. and Bricker, O.P. (1992) The influence of pH on biotite dissolution and alteration kinetics at low temperature. Geochimica et Cosmochimica Acta, 56, 3073-3092.

Anderson, S.J. and Sposito, G. (1991) Cesium-adsorption method for measuring accessible structural surface charge. Soil Science Society of America Journal, 55, 1569-1576.

Bailey, S.W., Ed. Micas. Reviews in Mineralogy 13. Mineralogical Society of America.

Barrett, S.D. (1997) Image analysis and the internet. Scientific Data Management, 1, 18-25.

Bickmore, B.R., Hochella, M.F., Jr., Bosbach, D., and Charlet, L. (1999a) Methods for performing Atomic Force Microscopy imaging of clay minerals in aqueous solutions. Clays and Clay Minerals, 47, 573-581.

Bickmore, B.R., Rufe, E., Barrett, S.D., and Hochella, M.F., Jr. (1999b) Measuring discrete feature dimensions in AFM images with Image SXM. Geological Materials Research, 1, n.5. See http://gmr.minsocam.org

Bickmore, B.R., Bosbach, D., Hochella, M.F., Jr., Charlet, L., and Rufe, E. (2000) In situ atomic force microscopy study of hectorite and nontronite dissolution: Implications for phyllosilicate edge structures and dissolution mechanisms. American Mineralogist, submitted.

Bish, D.L. and Duffy, C.J. (1990) Thermogravimetric analysis of minerals. In Thermal analysis in clay science, CMS workshop lectures vol. 3 (ed. J.W. Stucki, J.W., D.L. Bish, and F. A. Mumpton), pp. 95-157. The Clay Minerals Society.

Bleam, W.F. (1993) Atomic theories of phyllosilicates: Quantum chemistry, statistical mechanics, electrostatic theory, and crystal chemistry. Reviews of Geophysics, 31, 51-73.

Bosbach D, Charlet L, Bickmore BR, Hochella, MF, Jr. (2000) The dissolution of hectorite: In-situ, real-time observations using Atomic Force Microscopy. American Mineralogist, in press.

Brady, P.V., Cygan, R.T., and Nagy, K.L. (1996) Molecular controls on kaolinite surface charge. Journal of Colloid and Interface Science, 183, 356-364.

Brantley, S.L. and Chen, Y. (1995) Chemical weathering rates of pyroxenes and amphiboles. In Chemical Weathering Rates of Silicate Minerals, Reviews in Mineralogy 31 (ed. A.F. White and S.L. Brantley), pp. 119-172. Mineralogical Society of America.

Charlet, L., Schindler, P.W., Spadini, L., Furrer, G., Zysset, M. (1993) Cation adsorption on oxides and clays—the Aluminum case. Aquatic Sciences, 55, 291-303.

Casey, W.H., Carr, M.J., and Graham, R.A. (1988) Crystal defects and the dissolution kinetics of rutile. Geochimica et Cosmochimica Acta, 52, 1545-1556.

Deer, W.A., Howie, R.A., and Zussman, J. (1992) An Introduction to the Rock-Forming Minerals, 2nd edition. Longman Scientific & Technical.

Eltantawy, I.M. and Arnold, P.W. (1973) Reappraisal of the ethylene glycol monoethyl ether (EGME) method for surface area estimations of clays. Journal of Soil Science, 24, 232-238.

Eslinger, E. and Pevear, D. (1988) Clay Minerals for Petroleum Geologists and Engineers, SEPM Short Course Notes No. 22. Society of Economic Paleontologists and Mineralogists.

Furrer, G., Zysset, M., and Schindler, P.W. (1993) Weathering kinetics of montmorillonite: Investigations in batch and mixed-flow reactors. In Geochemistry of Clay-Pore Fluid Interactions (ed. D.A.C. Manning, P. L. Hall, and C.R. Hughes). Chapman & Hall.

Hansma, P.K., Cleveland, J.P., Radmacher, M., Walters, D.A., Hillner, P.E., Bezanilla, M., Fritz, M., Vie, D., Hansma, H.G., Prater, C.B., Massie, J., Fukunaga, L., Gurley, J., and Elings, V. (1994) Tapping mode atomic force microscopy in liquids. Applied Physics Letters, 64, 1738-1740.

Helgeson, H.C. (1971) Kinetics of mass transfer among silicates and aqueous solutions. Geochimica et Cosmochimica Acta, 35, 421-469.

Heydemann, A. (1966) Über die chemische Verwitterung von Tonmineralen (Experimentelle Untersuchungen). Geochimica et Cosmochimica Acta, 30, 995-1035.

Hochella, M.F. Jr. (1995) Mineral surfaces: Their characterization and their chemical, physical and reactive nature. In Mineral Surfaces (ed. D.J. Vaughan and R.A.D. Pattrick), pp. 17-60. Chapman & Hall, London.

Hochella, M.F. Jr., and Banfield, J.F. (1995) Chemical weathering rates of silicates in nature: A microscopic perspective with theoretical considerations. In Chemical Weathering Rates of Silicate Minerals, Reviews in Mineralogy 31 (ed. A.F. White and S.L. Brantley), pp. 353-406. Mineralogical Society of America.

Johnson, C.A. (1995) Applications of scanning probe microscopy part 4: AFM imaging in fluids for the study of colloidal particle adsorption. American Laboratory, 27, 12.

Kalinowski, B.E., Schweda, P. (1996) Kinetics of muscovite, phlogopite, and biotite dissolution and alteration at pH 1-4, room temperature. Geochim Cosmochim Acta, 60, 367-385.

Koretsky, C.M., Sverjensky, D.A., Sahai, N. (1998) A model of surface site types on oxide and silicate minerals based on crystal chemistry: Implications for site types and densities, multi-site adsorption, surface infrared spectroscopy, and dissolution kinetics. American Journal of Science, 298, 349-438.

Koster van Groos, A.F. and Guggenheim, S. (1990) High-pressure differential thermal analysis: Application to clay minerals. In Thermal analysis in clay science, CMS workshop lectures vol. 3 (ed. J.W. Stucki, D.L. Bish, and F.A. Mumpton), pp. 49-94. The Clay Minerals Society.

Malmström, M. and Banwart, S. (1997) Biotite dissolution at 25 °C: The pH dependence of dissolution rate and stoichiometry. Geochimica et Cosmochimica Acta, 61, 2779-2799.

Nagy, K.L. (1995) Dissolution and precipitation kinetics of sheet silicates. In Chemical Weathering Rates of Silicate Minerals, Reviews in Mineralogy 31 (ed. A.F. White and S.L. Brantley), pp. 173-233. Mineralogical Society of America.

Neumann, B.S. and Sansom, K.G. (1970) The study of gel formation and flocculation in aqueous clay dispersions by optical and rheological methods. Israel Journal of Chemistry, 8, 315-322.

O'Connor, B.H. and Chang, W.-J. (1986) The amorphous character and particle size distributions of powders produced with the micronizing mill for quantitative X-ray powder diffractometry. X-Ray Spectrometry, 15, 267-270.

Park, N.-S., Kim, M.-W., Langford, S.C. & Dickinson, J.T. (1996) Atomic layer wear of single-crystal calcite in aqueous solution using scanning force microscopy. Journal of Applied Physics, 80, 2680-2686.

Puledda, S. and Paoletti, L. (1994) Study the effect of comminution on the diffractometric response of chrysotile contained in a bulk sample. Annals of Occupational Hygiene, 38, 59-65.

Rich, C.I. (1969) Suction apparatus for mounting clay specimens on ceramic tile for x-ray diffraction. Soil Science Society of America Proceedings, 33, 815-816.

Rufe, E. and Hochella, M.F., Jr. (1999) Quantitative assessment of reactive surface area of phlogopite dissolution during acid dissolution. Science, 285, 874-876.

Russ, J.C. (1995) The image processing handbook, 2nd ed.. CRC.

Rutherford, D.W., Chiou, C.T., and Eberl, D.D. (1997) Effects of exchanged cation on the microporosity of montmorillonite. Clays and Clay Minerals, 45, 534-543.

Schlegel, M.L., Manceau, A., Chateigner, D., and Charlet, L. (1999) Sorption of metal ions on clay minerals: I. Polarized EXAFS evidence for the adsorption of Co on the edges of hectorite particles. Journal of Colloid and Interface Science, 215, 140-158.

Stephens, J.D. and Tuddenham, W.M. (1971) Infrared analysis of minerals. American Laboratory, 3, n. 11, 8-13.

Sutheimer, S., Maurice, P., and Zhou, Q. (1999) Dissolution of well and poorly crystallized kaolinites: Al speciation and effects of surface characteristics. American Mineralogist, 84, 620-628.

Turpault M.-P. Trotignon L. (1994) The dissolution of biotite single crystals in dilute HNO_3 at 24°C: Evidence of an anisotropic corrosion process of micas in acidic solutions. Geochimica et Cosmochimica Acta, 58, 2761-2775.

van Olphen, H. (1992) Particle associations in clay suspensions and their rheological implications. In Clay-Water Interface and its Rheological Implications, CMS Workshp Lectures vol. 4 (ed. N. Güven and R.M. Pollastro), pp. 191-210. The Clay Minerals Society.

van Olphen, H. and Fripiat, J.J., eds. (1979) Data Handbook for Clay Materials and Other Non-metallic Minerals. Pergamon.

White, G.N. and Zelazny, L.W. (1988) Analysis and implications of the edge structure of dioctahedral phyllosilicates. Clays and Clay Minerals, 36, 141-146.

Zachara, J.M. and McKinley, J.P. (1993) Influence of hydrolysis on the sorption of metal cations by smectites: Importance of edge coordination reactions. Aquatic Sciences, 55, 250-261.

Zysset, M. and Schindler, P.W. (1996) The proton promoted dissolution kinetics of K-montmorillonite. Geochimica et Cosmochimica Acta, 60, 921-931.

<table>
<tr><th></th><th>pH 1.0</th><th>pH 1.5</th><th>pH 2.0</th></tr>
<tr><td>Biotite</td><td>6.1 Ò3.0 x 10^{-9}</td><td>1.1 Ò0.6 x 10^{-8}</td><td>8.2 ± 4.4 x 10^{-9}</td></tr>
<tr><td>Montmorillonite</td><td>1.2 Ò0.5 x 10^{-8}</td><td>8.9 Ò4.8 x 10^{-9}</td><td>N/A</td></tr>
<tr><td colspan="4">All rates are reported in units of mol/m^2•s, where mol refers to moles of dissolved mineral, based on a 22 O formula, and m^2 refers to A_e.</td></tr>
</table>

Table 4-1. Dissolution rates of biotite and montmorillonite, normalized to edge surface area (A_e). Error estimations represent 95% confidence intervals.

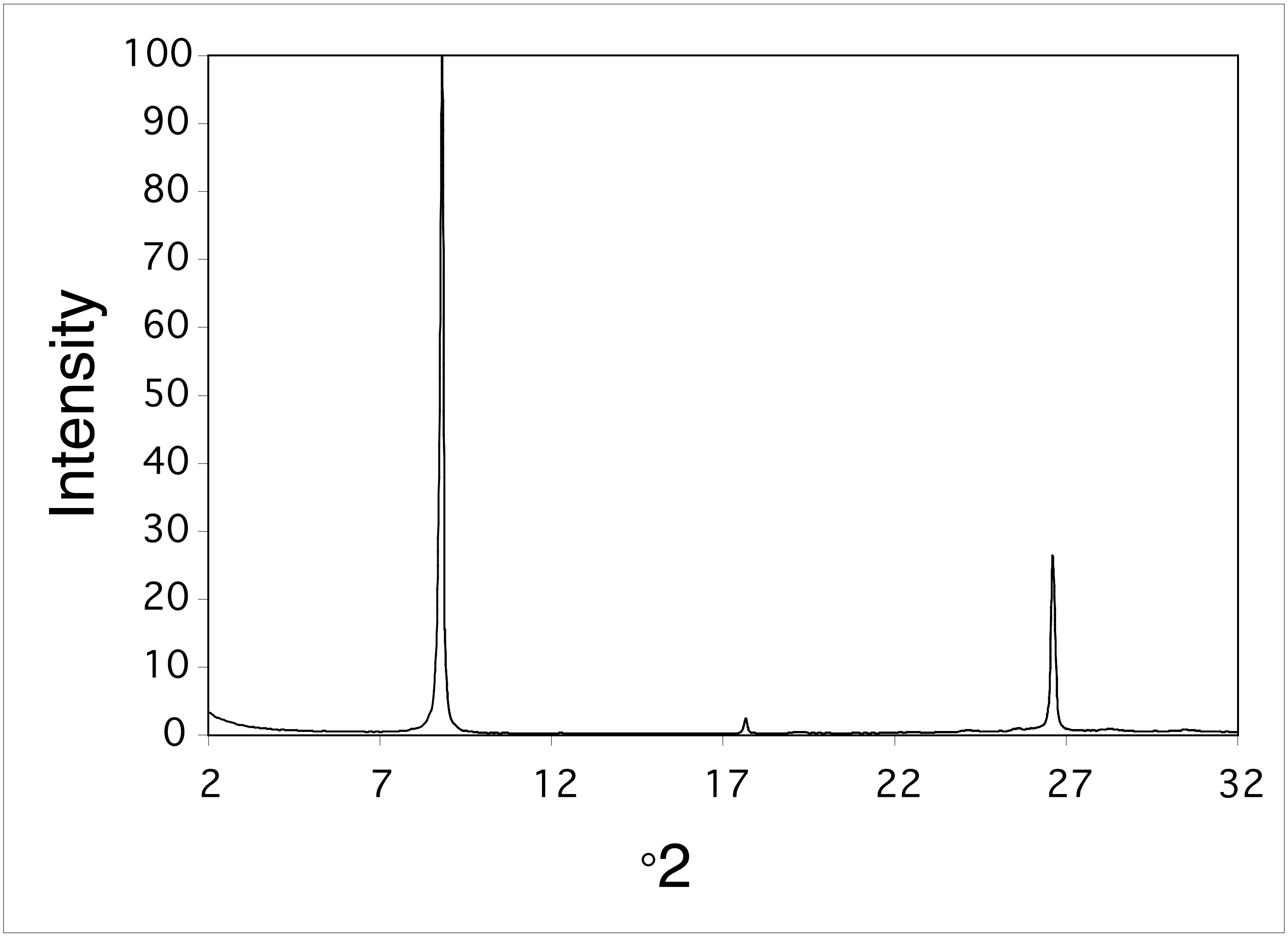

Figure 4-1. Powder XRD pattern for the clay fraction of the micronized biotite sample. The sharpness of the peaks shows that the grinding process did not create a significant amount of amorphous material.

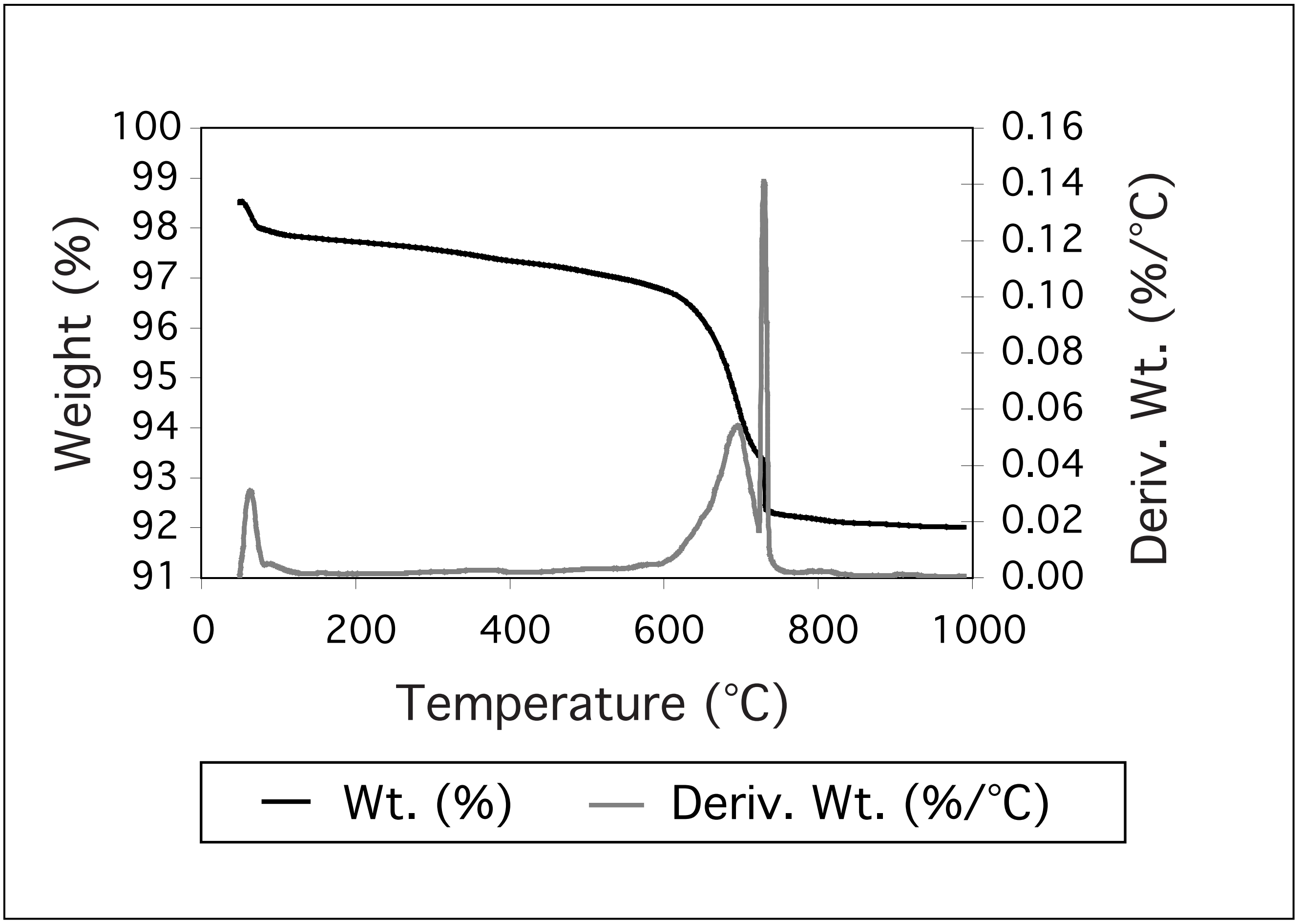

Figure 4-2. Weight loss and derivative weight loss curves for the SWy-1 montmorillonite sample, collected using high resolution thermogravimetric analysis (HRTGA). No secondary phases could be detected. Compare similar plots in Koster van Groos and Guggenheim (1990) and Bish and Duffy (1990).

Figure 4-3. TMAFM images of a particle of montmorillonite before and after 170 min. exposure to pH 1.5 HCl. The step height at the edge of the particle is 2.7 nm, and clearly the particle has dissolved inward from the edges. Scale bar = 1 μm.

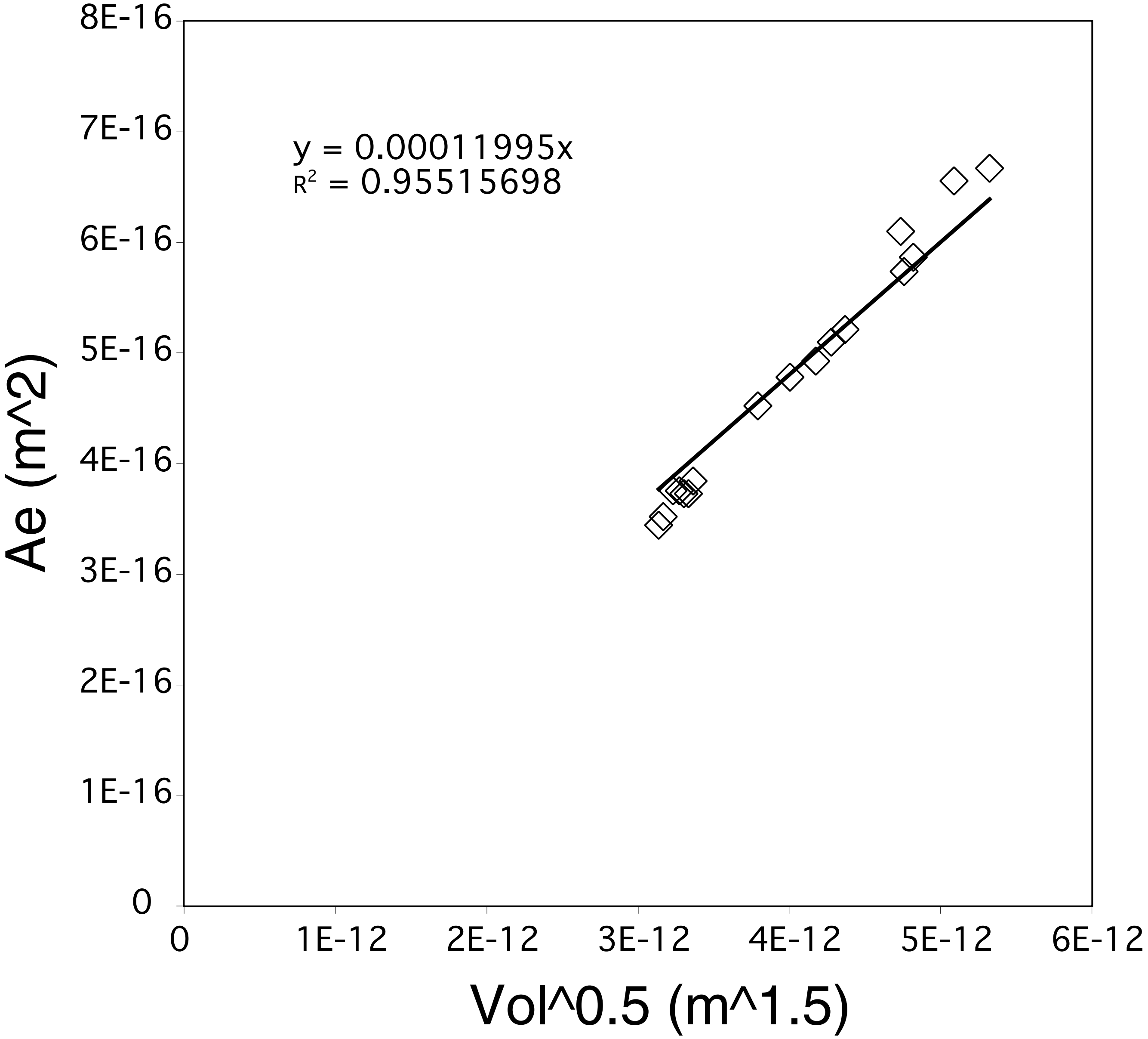

Figure 4-4. Plot of Ae vs. V1/2 for a montmorillonite particle dissolving at pH 1. The regression line is forced through the origin, still producing an excellent fit of the data. This shows that it is reasonable to assume that the shapes of clay particles stay essentially constant as they dissolve inward from the edges. The slope of the line is used as the b parameter in the calculation of Ae-normalized rates using the shrinking plate model. This parameter effectively serves as a mathematical description of the shape of the platy particle.

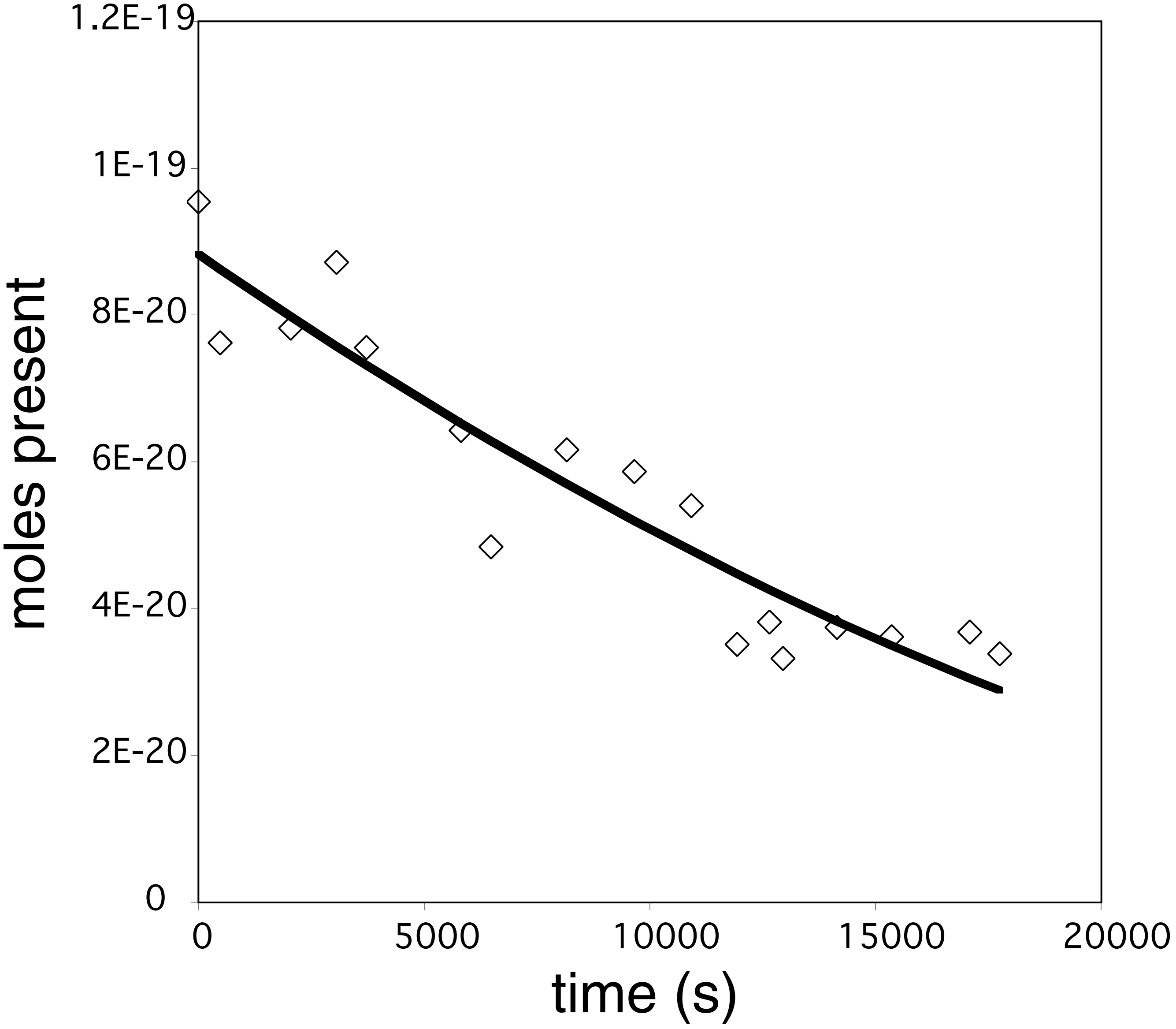

Figure 4-5. Plot of the number of moles present in a montmorillonite particle (the same particle discussed in Fig. 4-4) dissolving in pH 1.0 HCl over time. The diamonds are data points collected from AFM images, and the curved line represents the predicted evolution of the particle, using the shrinking plate model.

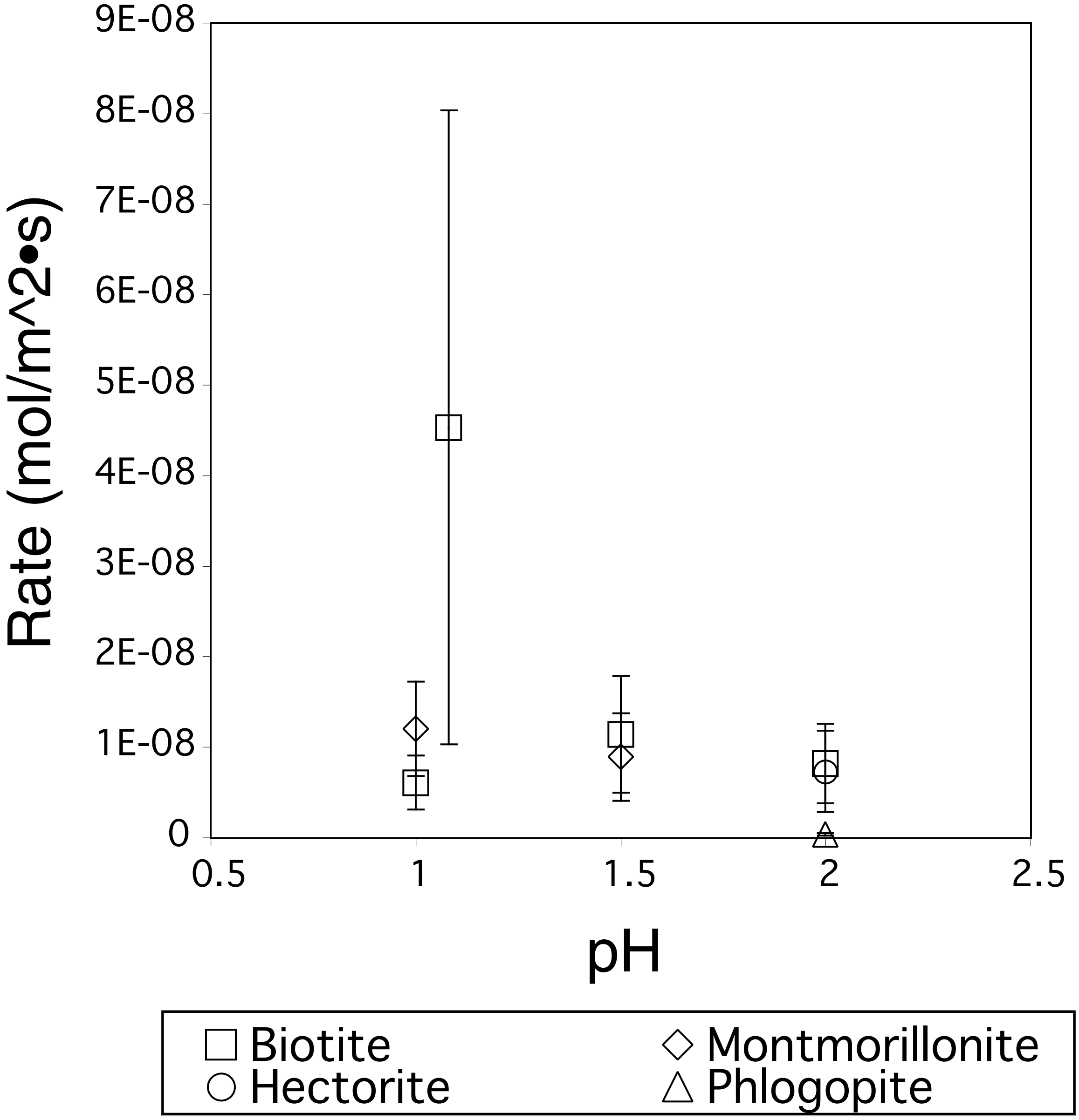

Figure 4-6. Ae-normalized dissolution rates for several 2:1 phyllosilicates in the pH range of interest (pH 1-2). Data for biotite and montmorillonite were taken from this study, except the biotite dissolution rate at pH 1.08, which was recalculated from the data of Turpault and Trotignon (1994). The hectorite rate was taken from Bosbach et al. (2000), and the phlogopite rate was taken from Rufe and Hochella (1999).

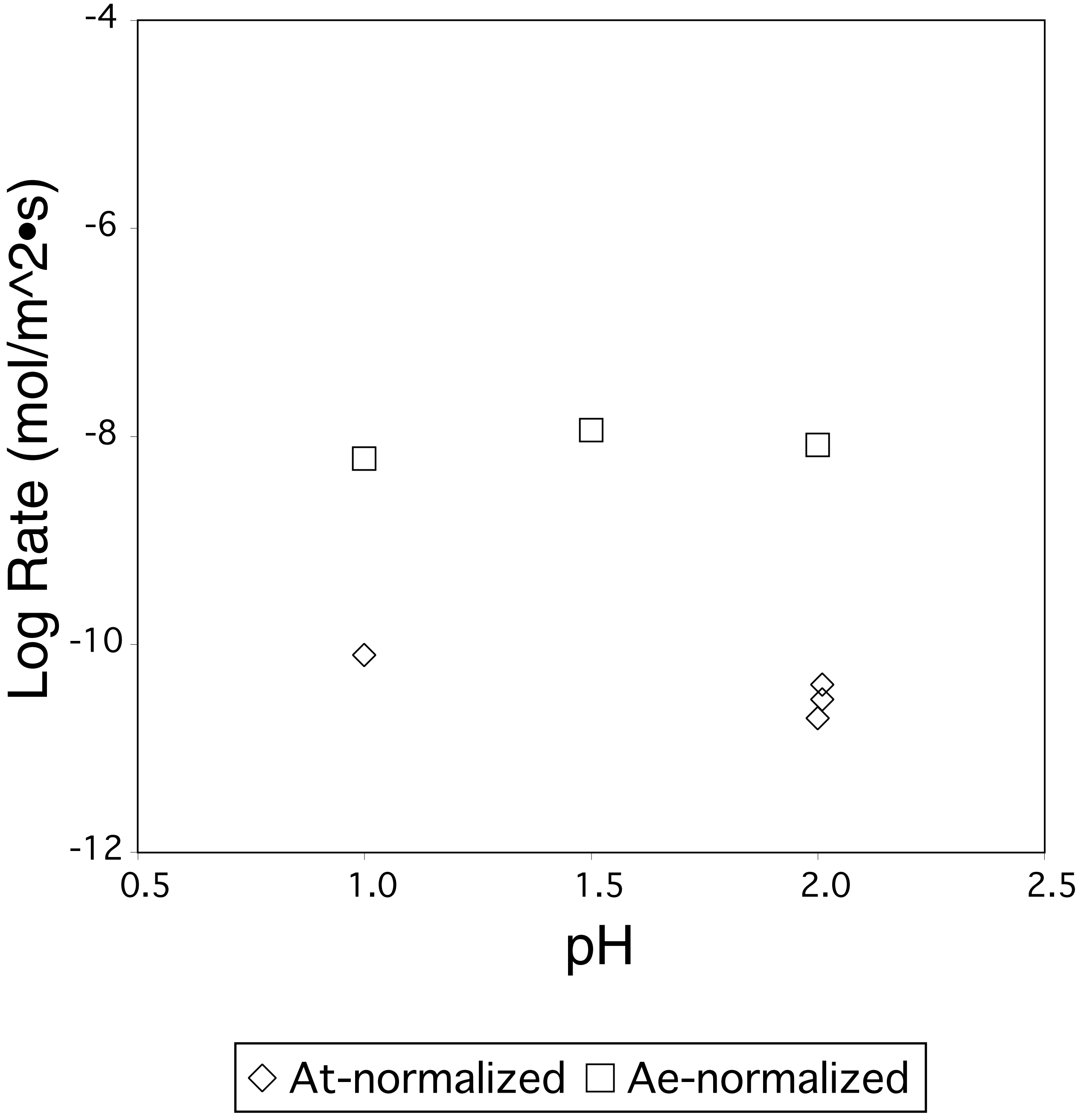

Figure 4-7. Ae-normalized biotite dissolution rates reported in this study, and BET-normalized (At) rates from Kalinowski and Schweda (1996) and Malmström and Banwart (1997). The Ae-normalized rates are ~75-400x the Ab-normalized rates. This difference can be explained in terms of the proportion of Ae, high energy sites at freshly ground edges, and the formation of leached layers.

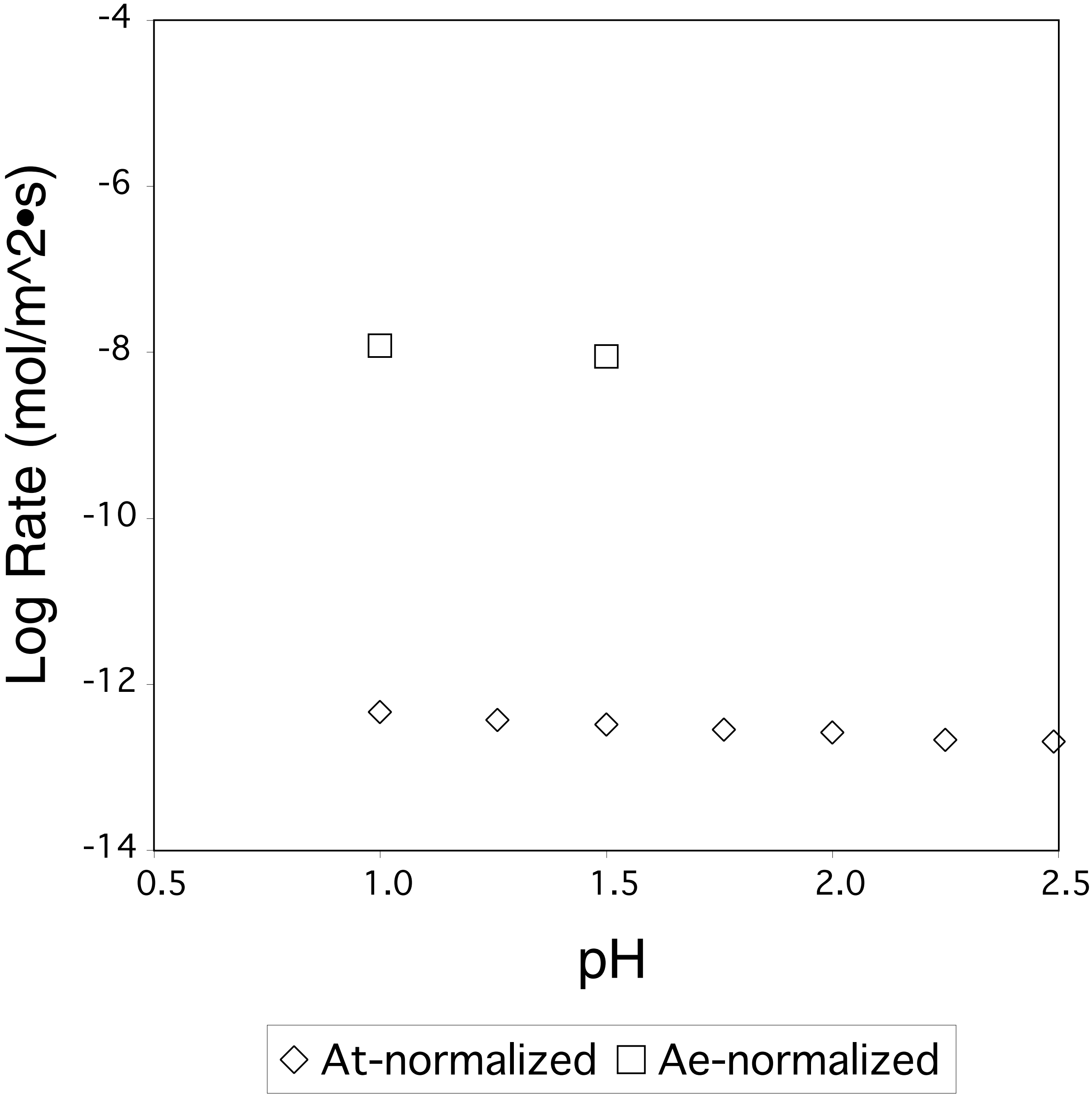

Figure 4-8. Ae-normalized montmorillonite dissolution rates reported in this study, and EGME-normalized (At) rates from Zysset and Schindler (1996). The Ae-normalized rates are ~26,000-28,000x the At-normalized rates. This difference cannot be explained in terms of the proportion of Ae, high energy sites at freshly ground edges, and the formation of leached layers, but can be explained if it is taken into account that the samples dissolved by Zysset and Schindler were likely flocculated in the reactor.

Chapter 5: Hectorite and Nontronite Dissolution: Implications For Phyllosilicate Edge Structures and Dissolution Mechanisms

Introduction

Atomic Force Microscopy (AFM) has proven to be a powerful tool to explore various aspects of the structure, microtopography, and surface reactivity of minerals (see Nagy and Blum, 1994; Hochella, 1995; Hochella *et al.*, 1998). Perhaps its greatest strength, from a geochemical perspective, has been the ability to make quantitative measurements of changing surface microtopography *in situ*, as minerals react in aqueous solutions (Drake *et al.*, 1989; Hillner *et al.*, 1992; Dove and Hochella, 1993; Bosbach and Rammensee, 1994; Dove and Chermak, 1994; Junta and Hochella, 1994; Bosbach *et al.*, 1995; Putnis *et al.*, 1995; Bosbach and Hochella, 1996; Bosbach *et al.*, 1996; Grantham and Dove, 1996; Liang *et al.*, 1996; Junta-Rosso *et al.*, 1997; Bosbach *et al.*, 1998; Teng *et al.*, 1998; Rufe and Hochella, 1999). Such observations often bring to light the fact that some mineral faces are more reactive than others, and given a model of the crystallographic structure of these faces, one can sometimes infer the dominant mechanism(s) of the surface reaction in question (e.g. Liang *et al.*, 1996; Bosbach *et al.*, 1998; Rufe and Hochella, 1999).

Due to the extreme anisotropy of their structures, phyllosilicate surfaces have been shown to exhibit strong differential reactivity (Schofield and Samson, 1953; White and Zelazny, 1988; Anderson and Sposito, 1991; Zachara and McKinley, 1993; Bleam, 1993; Turpault and Trotignon, 1994; Brady *et al.*, 1996). However, until recently the applicability of *in situ* AFM techniques to phyllosilicate surface reactivity has been limited due to two major factors. First, phyllosilicates are generally characterized by only one cleavage plane – perfect cleavage along the (001) basal surface. While other faces often occur as preferred growth surfaces, in the case of macroscopic phyllosilicate crystals (e.g. micas) these are usually too narrow or rough for AFM analysis. Zones of mechanical weakness within micas run parallel to the preferred growth faces

(Bloss *et al.*, 1959; Klein and Hurlbut, 1993), but the small-scale step features generated by cleaving these minerals are generally not euhedral, and hence the "edge" faces available for examination by AFM are randomly-oriented surfaces. This makes possible the comparison of the reactivity of non-specific edge surfaces with that of the basal planes, but since the structures of the randomly-oriented surfaces are not strictly crystallographically constrained, specific mechanistic information is more difficult to infer. Rufe and Hochella (1999) recently overcame this problem to some extent by pre-etching phlogopite surfaces with HF, in order to examine the dissolution behavior of etch pits in HCl and deionized H_2O with *in situ* AFM. The etch pits were essentially euhedral along the preferred growth faces, and similar features have been generated on various mica surfaces by etching with either HF or fused alkalis (Pandya and Pandya, 1959; Patel and Ramanathan, 1962). Second, although clay minerals (phyllosilicates with a Stokes settling diameter of <2 μm) often exhibit euhedral growth faces at their edges, small enough to examine with AFM, it has been difficult to immobilize such tiny particles on a suitable substrate for *in situ* analysis (Dove and Chermak, 1994). However, Bickmore *et al.* (1999a) recently described methods for the immobilization of clay minerals for *in situ* AFM analysis under various solution conditions, and Bosbach *et al.* (1999) have applied one of these techniques to examine the dissolution behavior of single crystallites of hectorite clay in HCl.

In this paper, we compare the results of Bosbach *et al.* (1999) on hectorite dissolution with the *in situ* AFM nontronite dissolution results of this study. We relate the observed differential reactivity of the crystal faces to models of the atomic structure of phyllosilicate edge faces, and determine which one best explains our data. Within the framework of the chosen model of the edge surface structure, we then relate our results to current models of the proton-promoted dissolution of phyllosilicates, and determine which one best accounts for the data obtained in this and other studies.

The structure and reactivity of phyllosilicate surfaces is of fundamental importance for the understanding of ion mobility in the near-surface environment, permeability reduction in reservoir rocks, and many other geochemical processes (e.g. Sposito, 1984; Eslinger and Pevear, 1988). *In situ* AFM imaging of reactions on phyllosilicate surfaces presents the possibility of acquiring information about these topics that would, at best, be very difficult to obtain via other experimental methods now available.

Materials and Methods

Samples

Hectorite.

A sample of hectorite (SHCa-1, Hector, California) was obtained from the Clay Minerals Society Source Clay Repository. Hectorite $Na_{0.80}(Mg_{5.30}Li_{0.70})(Si_{7.90}Al_{0.10})O_{20}(OH)_4$ (Schlegel *et al.*, 1999) is a trioctahedral, magnesian smectite with some Li substituting for Mg in the octahedral layer. The <2 μm fraction of the sample material was collected, sodium saturated, acid washed, and treated with dithionate-citrate-bicarbonate and H_2O_2 solutions. A more complete description of the preparation and characterization procedures can be found in Schlegel *et al.* (1999).

The hectorite crystallites are predominantly lath-shaped, the long edges representing (010) surfaces, and the short edge surfaces representing (110), $(1\bar{1}0)$, (100), or broken edges (Oberlin and Méring, 1966; Güven, 1988; Bosbach *et al.*, 1999).

Nontronite

We obtained the nontronite sample from Ward's (nontronite #33A, Garfield, Washington). Garfield nontronite $Na_{0.96}(Fe^{3+}_{3.96}Mg_{0.02}Ti_{0.02})(Si_{6.94}Al_{1.06})O_{20}(OH)_4$ (Bonnin *et al.*, 1985) is a dioctahedral smectite with the montmorillonite structure (Eggleton, 1977; Besson *et al.*, 1982; Besson *et al.*, 1983; Bonnin *et al.*, 1985; Manceau *et al.*, 1998). The sample was crushed in a mortar and pestle, suspended in 500 ml of deionized H_2O, and blended in a Waring heavy-duty blender for several minutes. Large fragments were allowed to settle out of the suspension, and the supernatant was decanted. The < 2 μm fraction of the suspension was separated by centrifugation. In order to remove associated Fe oxides (predominantly goethite, see Güven, 1991; Murad, 1987), the < 2 μm fraction was carefully subjected to several sedimentation cycles in deionized H_2O (Manceau *et al.*, 1998). The sample was then acid washed 4 times by shaking for one hour in pH 3.0 HCl, and centrifuging. It was then Na-saturated. Approximately 280 mg of the purified sample was mounted on a ceramic tile for powder X-ray Diffraction analysis (Rich, 1969), and no secondary phases were detected.

The Garfield nontronite crystallites are predominantly lath-shaped (Güven, 1991), the long edges representing (010) faces (Grim and Güven, 1978; Güven, 1991), and the short edges representing (110), $(1\bar{1}0)$ (White and Zelazny, 1988), (100), or broken edge faces.

Clay immobilization

The clays were immobilized for *in situ* AFM analysis using variations on one of the techniques described by Bickmore *et al.* (1999a). The exact procedure used for the hectorite sample is described by Bosbach *et al.* (1999). With the nontronite sample, polyethyleneimine $(C_2H_5N)_n$ (M.W. 1800, Polysciences, Warrington, Pennsylvania) was diluted 1:500 by volume. A small disc of freshly-cleaved muscovite was taped with double-sided tape to a similarly-shaped steel AFM sample puck and immersed in the suspension for ~30 s. The muscovite was then rinsed with a stream of deionized water for 5 min and dried in a 90°C oven for 20 min. A dilute suspension of the clay in deionized H_2O (~0.2 mg clay per 20 ml) was prepared and then dispersed for 1-2 min. with an Artek sonic dismembrator (Dynatech Laboratories, Chantilly, Virginia, model 300) set at ~150 Watts. The dried PEI-coated muscovite was immersed in the clay suspension for 1 min, and then blown dry with a stream of compressed air.

AFM imaging

Imaging of both the hectorite and nontronite crystallites was performed in the fluid cell of a MultiMode atomic force microscope (Digital Instruments, Santa Barbara, California). Hectorite imaging was performed with pyramidal Si_3N_4 tips, while nontronite imaging was performed with oxide-sharpened Si_3N_4 tips. Bosbach *et al.* (1999) reported that force–distance curves showed a large attractive peak due to the presence of the PEI coating, whereas on clean mica surfaces in aqueous solution there were not such strong adhesive interactions with the AFM tip. This sometimes made it difficult to collect stable images in TappingMode (TMAFM), so contact mode was exclusively used to observe the hectorite dissolution reactions. The strong attraction between the AFM tip and the PEI-coated mica substrate resulted in a tip loading force of about 50 – 100 nN, and therefore some hectorite particles were stripped from the surface during the course of the experiments. Tip-sample interaction can result in enhanced dissolution rates of monolayer steps (Park et al., 1996), but Bosbach *et al.* (1999) reported that they could detect no relationship between scan speed or AFM feedback control parameters and particle edge dissolution rates. Similarly, we have performed some nontronite dissolution experiments in TMAFM, which results in a much weaker tip-sample interaction (Hansma *et al.*, 1994; Johnson, 1995). However, we found that contact-mode imaging did, in fact, enhance the nontronite dissolution rate in a very specific manner, which will be discussed below.

Bosbach *et al.* (1999) imaged the hectorite under deionized water, and then pH 2.0 HCl was injected into the cell, after which dissolution was observed. The same procedure was used with the nontronite, although pH 1.5-2.0 HCl solutions were used.

The AFM images are constructed from height data, and were subjected to the flattening routine (a *least-squares* polynomial fit to remove unwanted features from the scan lines) included with the Digital Instruments software. 5-10 repetitions of a 3x3 median filter were also applied to the images to remove random noise (Russ, 1995). Analysis of features in the images was accomplished using the ImageSXM image analysis program (Barrett, 1997).

Crystal structure modeling

The crystal structures and surface planes of hectorite and nontronite were modeled using the CrystalMaker© program for the Macintosh (Palmer, 1996; cf. Koretsky *et al.*, 1998). Data used to generate models of the nontronite structure were taken from Besson *et al.* (1983) and Bonnin *et al.* (1985). The unit cell parameters used to calculate site densities for nontronite are a=5.28 Å, b=9.14 Å, c=10.1 Å, and β=99°. Atomic coordinates for hectorite were obtained from Oberlin and Méring (1966), as were the a and b parameters. The β angle was estimated at 99°, in agreement with the discussion of smectite minerals in Deer *et al.* (1992). Given the above, the c cell parameter was adjusted to produce a d_{001} spacing of 9.65 Å, as measured for dehydrated Na-hectorite by Kadi-Hanifi and Méring (1972). Thus, the unit cell parameters chosen for hectorite are a=5.25 Å, b=9.09 Å, c=9.77 Å, and β=99°.

The site densities on the (010), (110), and $(1\bar{1}0)$ faces of hectorite and nontronite were calculated by counting the number of sites per planar cell for the (hkl) in question. The planar cell areas were calculated by taking the cross product of the vectors defining the parallelogram which outlines a planar cell on that face (Boisen and Gibbs, 1985). Given the above, the unit cell face areas for nontronite are $A_{(010)} = 0.527$ nm^2, and $A_{(110)} = A_{(1\bar{1}0)} = 1.063$ nm^2, and the unit cell face areas for hectorite are $A_{(010)} = 0.507$ nm^2, and $A_{(110)} = A_{(1\bar{1}0)} = 1.080$ nm^2.

Results and Discussion

Differential reactivity of crystal faces

Hectorite dissolution

Bosbach *et al.* (1999) report that the dissolution of the hectorite laths appeared to occur exclusively at the edge surfaces during the time scale of the experiments (up to several hours). A continuous decrease in particle volume occurred. The particle length/width ratio did not change significantly during the dissolution process, which, given the morphology of the crystallites, suggested that the average dissolution rate at the ends of the laths (usually broken edges) was about 6 times faster than at the lath sides, which were generally euhedral (010) faces. Even euhedral edges of the laths appeared to “roughen” slightly over time (see Fig. 1). The basal (001) surfaces did not appear to participate in the reaction.

Nontronite dissolution

The nontronite also appeared to dissolve exclusively from the edges during the time scal of these experiments (up to 5 hours). Particle heights for several flat laths were measured over time during contact mode dissolution experiments using smoothed height histograms of the area of the image around each particle (Bickmore *et al.*, 1999b), and it was found that the particle height did not significantly change over time. For instance, height measurements over time for several very flat nontronite laths, observed in various dissolution experiments, are plotted in Fig. 2. Significant dissolution of all these particles was observed at the edges, but the particle heights did not change appreciably over time except for the two tallest particles in the plot, off of which approximately 5 Å of detrital material was immediately cleared, and then no further height change was observed. Similarly, no etch pits were observed to form on the basal surfaces of the laths. The average measured particle heights for the laths analyzed for Fig. 2 generally were 3.3-3.5 nm, and one was ~1.7 nm. These values are consistent with 2 or 1 unit cell high particles, respectively, since the height of one T-O-T layer (0.9-1 nm) plus the height of a monolayer of PEI (0.6 ±0.3 nm) (Bickmore *et al.*, 1999a; Bosbach *et al.*, 1999) would be approximately 1.2-1-9 nm, and the added height of another T-O-T layer plus a Na-saturated interlayer (0.5-1 nm) (**) would result in a particle height of 2.7-3.9 nm.

Very little dissolution even at the edge surfaces of the nontronite laths was observed in TMAFM, except where ragged edges seemed to straighten somewhat so that the edges more exactly paralleled the euhedral edge faces.

In contact mode, however, the dissolution at the edges was enhanced in two ways. First, due to the large tip-sample attraction, long, thin portions of the laths were sometimes broken off by the AFM tip, creating a high-energy, randomly oriented surface. Second, the tip sometimes appeared to “nick” the edges of the particles, again creating a high-energy, randomly oriented defect surface. Both the broken edges and the defect sites dissolved very quickly, until the dissolution front became pinned parallel to the (010), (110), and $(1\bar{1}0)$ edges. In rare cases, (100) growth surfaces were observed, which sometimes appeared to be stable under acid conditions. However, the reaction fronts at broken edges and defect sites were never observed to stabilize along the (100) plane. This behavior is clearly illustrated in Fig. 3, which is a time series of AFM images taken during the dissolution of several nontronite crystallites in pH 2.0 HCl. The dissolution behavior of the two laths near the center of the images is especially relevant. Fig. 3a was taken under deionized water, while Fig. 3b was taken just 6 min. after injection of the acid. At 6 min. exposure, the outline of the laths appear to have “sharpened” along the (010), (110), and $(1\bar{1}0)$ faces. At 38 min. exposure (Fig. 3c), the probe tip appears to have nicked the top lath at point A, and the dissolution front has retreated to the point where it has started to approximate the euhedral face angles. Similarly, the tip appears to have nicked the bottom lath at point B, and the dissolution front there has proceeded inward and then been pinned along the euhedral face planes. After 60 min. exposure (Fig. 3d), the outline of the top lath appears to have remained fairly stable, whereas the probe tip appears to have broken off the end of the bottom lath at point

C, and nicked it at point D, after which the dissolution fronts in these areas proceeded inward until they again became pinned parallel to the directions of the euhedral faces.

Edge vs. basal reactivity

As noted above, the basal surfaces of neither the hectorite nor the nontronite particles appeared to significantly participate in the dissolution reactions within the time scale of these experiments (up to several hours). This is to be expected, since the basal surfaces are characterized exclusively by charge-satisfied and extremely stable siloxane bonds, whereas the edge surfaces are characterized by broken bonds and a well-known tendency to form inner-sphere complexes with protons and other cations (e.g. White and Zelazny, 1988; Zachara and McKinley, 1993; Charlet *et al.*, 1993; Schlegel *et al.*, 1999). Similarly, Turpault and Trotignon (1994) dissolved macroscopic flakes of biotite of known dimensions in pH 1.08 HNO_3 at 24 °C, and demonstrated that the edge surfaces were approximately 250 times more reactive than the basal surfaces. In addition, Rufe and Hochella (1999) performed *in situ* TMAFM acid dissolution experiments on pre-etched phlogopite surfaces, and found that the dissolution reaction in its early stages occurs via retreat of monolayer edge steps while basal surfaces remain stable. Based on ^{19}F MAS NMR data, Kaviratna and Pinnavaia (1994) inferred that the acid hydrolysis of fluorohectorite proceeded almost exclusively at the edge surfaces, and only in its late stages at the basal surfaces. Since our experiments lasted no more than several hours, our data are consistent with these studies, and also with the general consensus over several decades that the acid hydrolysis of 2:1 phyllosilicates essentially proceeds exclusively at the edge surfaces through most of the reaction (see Nagy, 1995, and references therein).

Hectorite vs. nontronite edge reactivity

The difference in reactivity between the hectorite and nontronite edge faces is very interesting. Whereas the nontronite edges appeared to straighten, to more closely parallel the euhedral face planes, the hectorite edges roughened over time. Whereas the nontronite edges dissolved much faster at broken edges and defect sites (whether tip-induced or not), and the reaction fronts eventually became pinned at the euhedral face plane angles, the hectorite edges all appeared to dissolve at relatively similar rates.

Given these observations, we can draw two important conclusions. First, the active sites at the hectorite edges are all similar in their reactivity. While broken edges may have some especially reactive sites, which enhance their step retreat rate somewhat, the reactivity of the euhedral edges was comparable. The fact that the euhedral edges appeared to roughen over time graphically illustrates that their reactivity is similar to non-euhedral faces. Second, for some reason the active sites at the nontronite euhedral edges are much, much less reactive than those at broken edges and defects. It was pointed out that the AFM tip appeared to generate defect sites at the edges, which greatly enhanced their reactivity. On the other hand, such defects were undoubtedly generated during the experiments on the hectorite laths, but a similar increase in reactivity was not observed.

Implications for edge surface structure

Models of phyllosilicate edge structures

These conclusions about the reactivity of hectorite and nontronite edges obviously must be explained in terms of the atomic structure and reactivity of the edge surfaces in question. However, given the morphology and chemistry of these minerals, it is not presently possible to directly probe the structure of specific phyllosilicate edge surfaces using techniques like Low Energy Electron Diffraction or Scanning Tunneling Microscopy (see Hochella, 1990). To date models of phyllosilicate edge structure have usually been derived using established crystallochemical principles (see Bleam, 1993).

Several workers have proposed schematic models of the types of sites available at phyllosilicate edges, in order to explain their observed pH dependent charge (Schofield and Samson, 1953; Muljadi *et al.*, 1966; van Santen, 1982). However, others have constructed more detailed and useful models, taking into account differences in the crystal structure parallel to preferred growth faces. For instance, White and Zelazny (1988) used the crystal growth theory of Hartman and Perdock (1955a,b,c; Hartman, 1963, 1973, 1978; cf. Paquette and Reeder, 1990, Fouke and Reeder, 1992) to predict the topology of edge sites on the (110), $(1\bar{1}0)$, and (010) faces of dioctahedral phyllosilicates. They further speculated that a certain amount of bond relaxation occurred on the (110) and $(1\bar{1}0)$ faces, leaving them uncharged at normal pH levels (pH 3-9). Bleam *et al.* (1993) used an identical method to predict the topology of the same edges on pyrophyllite, as well as the (100) and (130) faces. However, they did not allow for surface relaxation, but instead used an unrelaxed surface configuration, and optimized the surface OH bond vectors to obtain the surface Coulomb energy and proton Coulomb energy for these faces. Koretsky *et al.* (1998) predicted the site types and densities on prominent crystal faces of several minerals, including the kaolinite (010) and (110) edges, by slicing the crystal structures along planes that produced the minimum total strength of bonds severed, calculated using the method of Altermatt and Brown (1985). While Koretsky *et al.* (1998) did not provide illustrations of the inferred edge surface topologies, it appears from the site types they predicted that they likely chose to terminate these edge faces along the same planes predicted by crystal growth theory. As with Bleam *et al.* (1993), they did not allow for surface relaxation.

We have chosen to interpret our results within the framework of the type of model articulated by White and Zelazny (1988). As will be shown below, allowing for charge neutralization via surface relaxation at some edge sites provides us with a rationale for the exceptionally low reactivity of the preferred growth faces on nontronite. Specifically, the O atoms connecting between the octahedral and tetrahedral sheets (hereafter designated "connecting oxygens") on dioctahedral phyllosilicates are predicted to be fully bonded, and hence less reactive with respect to proton attack. On the other hand, some of the connecting oxygens at kink sites on broken edges and the connecting oxygens on trioctahedral edge faces are predicted to be underbonded. In order to show that this is the case, in the following sections Hartman-Perdock crystal growth theory will be applied to predict the topology of all the relevant edge surfaces.

Hartman-Perdock crystal growth theory

Hartman and Perdock (1955a,b,c) proposed that the typical morphology of crystals could be explained in terms of bond energies. Crystal growth is approximated as the formation of strong bonds between growth units of stoichiometric composition (Grim and Güven, 1978), and growth faces are observed to lie parallel to one or more continuous chains of strong bonds within the crystal structure, called Periodic Bond Chains (PBCs). It must be possible to divide the entire crystal structure into PBCs of stoichiometric composition, which have no bonds in common, and a PBC must not entirely consist of periods of other PBCs. Planes parallel to two or more PBCs exhibit a low surface energy configuration, which results in a prominent, flat (F) face. Faces parallel to one PBC are stepped (S), and are less prominent than F faces. Kinked (K) faces are parallel to no PBCs, and due to their high surface energy, usually do not occur as growth surfaces.

The topology of the predicted F and S surfaces may be inferred by assuming that they are terminated along the edges of the stoichiometric PBCs. However, Grim and Güven (1978) pointed out that one cannot realistically impose the condition of stoichiometry on such a complex structure, and instead defined separate PBCs along chains of oxygen-linked tetrahedral and octahedral cations. For the purpose of defining edge surface topology, in this paper we will adhere to the condition of stoichiometry with respect to the phyllosilicate T-O-T layers, unless a particularly high-energy surface is generated. In addition, all edge sites will be terminated with O atoms or OH groups.

Prediction of edge surface topology

White and Zelazny (1988) began their analysis of dioctahedral edge structure by defining the minimum stoichiometric units required for crystal growth, according to PBC theory. (Obviously this is somewhat of an oversimplification of the actual crystal growth process.) For 2:1 dioctahedral phyllosilicates without ordered substitution, this may be represented by two tetrahedra connected to a single octahedron, neglecting interlayer cations. The tetrahedron connected to the top of the octahedron is related to the tetrahedron connected to the bottom by a center of symmetry, so as not to create a dipole (see Fig. 4). Grim and Güven (1978) and Hartman (1982) showed that the PBCs in phyllosilicates are along the $[1\bar{1}0]$, [100] and [110] directions, so that a flat (001) face is predicted, as well as stepped (110), (010), and $(1\bar{1}0)$ edge growth faces. Consistent with this, atomically flat (001) faces dominate phyllosilicate crystal habits, and the predicted edges are the “pseudohexagonal” faces normally observed on euhedral phyllosilicate crystals. The fundamental crystal growth units are linked together in the PBCs shematically represented by the polyhedral models shown in Fig. 5, and ball and stick models of the PBCs, viewed parallel to the chain directions are shown in Fig. 6. It can be seen in this figure that edge faces terminated on either side of the chains would result in an equivalent topology. Also, the chains parallel to the (110) and $(1\bar{1}0)$ edges are symmetrically equivalent, so only the (110) is depicted here.

Bleam *et al.* (1993) suggested that the previous workers had neglected to describe two important PBCs in the phyllosilicate structure, parallel to the (100) and (130) edges. They supported this assertion by citing Sun and Baronnet (1989a,b), who reported synthetically grown phlogopite crystals with (100) and (130) faces. However, a closer analysis of the phyllosilicate structure shows that the bond chains parallel to (100) and (130) are what Hartman and Perdock (1955b) called “zigzag chains”, composed entirely of periods of other PBCs. The simple fact of their occurrence does not *a priori* indicate the presence of a PBC parallel to these faces. Indeed, Lazarenko *et al.* (1979) catalogued the occurrence of 33 distinct faces on phlogopite crystals grown in carbonatites, so it seems more realistic to designate (100) and (130) phyllosilicate edges as rarely-occurring K faces. This conclusion also seems consistent with Sun and Baronnet’s results, where the (100) and (130) forms were important only under low supersaturation conditions (Sun and Baronnet, 1989a) and where Cr inhibited the growth of these faces (Sun and Baronnet, 1989b).

The “zigzag” nature of the chains parallel to (100) and (130) can be clearly seen by examining the polyhedral representations in Figs. 7-8. In Fig. 7, a dioctahedral sheet structure is viewed perpendicular to the (001) plane, and tetrahedral elements of the bond chains parallel to (010), (110), $(1\bar{1}0)$, and (100) are highlighted. The chain of bonds parallel to (100) is composed exclusively of elements of the PBCs parallel to (010), (110), and $(1\bar{1}0)$. An identical result is obtained by examining the octahedral elements of these bond chains, and Fig. 8 shows the same to be true for the chain parallel to (130). Therefore, when interpreting the observed reactivity of the (100) growth faces on nontronite and hectorite laths, we will consider them as kinked surfaces composed of elements of the (010), (110), and $(1\bar{1}0)$ faces. (For a trioctahedral structure, the octahedral chains parallel to (100) and (130) would still be composed entirely of elements of other PBCs, but their edges would be straight. Perhaps this adds to the stability of these faces for trioctahedral minerals like phlogopite.)

The application of PBC theory to trioctahedral phyllosilicates is a somewhat more complex task. In order to maintain stoichiometry, the minimum growth unit for a trioctahedral T-O-T layer must consist of 4 tetrahedra and three octahedra, including two M2 and one M1 sites (see Fig. 9). Polyhedral representations of the PBCs formed by linking these chains are shown in Fig. 10, and ball and stick models of the PBCs, viewed parallel to the chain directions are shown in Fig. 11. Again, the bond chains parallel to (110) and $(1\bar{1}0)$ are symmetrically equivalent, so only the (110) is depicted. In Fig. 11a, it can be seen that terminating edge faces on either side of the (110) and $(1\bar{1}0)$ chains would result in an equivalent topology of edge sites. On the other hand, Fig. 11b shows that terminating edges on either side of the (010) chain would result in two very different edge site topologies. Whereas one side would be equivalent to the (010) edge of a dioctahedral phyllosilicate, the other would have M1 octahedra protruding from the surface. However, a tally of the type and number of bonds severed to generate such surfaces reveals that two more Si-O bonds per unit cell repeat would have to be broken to generate a surface with protruding M1 octahedra than to generate one without. Therefore, in our analysis we will assume that stable (010) surfaces on trioctahedral phyllosilicates have an edge site topology equivalent to that of a (010) face on a dioctahedral phyllosilicate.

Surface relaxation and observed reactivity

The assumption that surface sites with unsaturated valency are more reactive than fully saturated sites, using various methods for calculating bond valence, has commonly been used to explain the differential reactivity of crystal faces (e.g. van Santen, 1982; Ziolkowski, 1986; Bleam, 1993; Bargar *et al.*, 1997; Towle *et al.*, 1999a,b), with at least qualitative success. We will make the same assumption here to rationalize the observed reactivity of the nontronite and hectorite edge faces. Simple Pauling bond strengths will be used, where: $\zeta = \sum_i \frac{Z_i}{v_i}$. In this equation, ζ is the total bond strength coordinating each O or OH surface site, Z_i is the valence of each cation coordinating the site, and v_i is the coordination number of each cation.

Table 1 lists all the sites available on the surfaces of edge faces of nontronite and hectorite, terminated by the PBCs discussed above. Since we are making generalizations about the reactivity of distinct crystal faces, we have ignored the effects of isomorphous substitutions (see White and Zelazny, 1988). Thus, ideal structures with only one type of tetrahedral cation (Si^{4+}) and one type of octahedral cation (Fe^{3+} or Mg^{2+}) are included. In the first column of Table 1 is listed the type of site (O or OH), and the coordinating atoms are listed in the second. The third column lists the total strength of bonds coordinating each site based on simple Pauling bond strengths. The fourth column lists the number of each site per unit cell repeat, and the fifth column lists the same site densities in sites/nm^2, using the unit cell face areas calculated above.

In the nontronite structure, the 2-coordinated connecting oxygens on the (110) and $(1\bar{1}0)$ edges are situated adjacent to 1-coordinated oxygens bonded to octahedral Fe. White and Zelazny (1988) suggested that if the 1-coordinated O were doubly protonated, this Fe-O bond might lengthen out to a bond strength of near 0, resulting in an uncharged bound water site. Simultaneously, the bonds to the adjacent 2-coordinated connecting O would shorten, raising the total bond strength reaching this site to 2, leaving the 2-coordinated oxygen fully charge-satisfied. Given that at pH values between approximately 3 and 9 the silanol groups at these edges would be singly protonated, leaving these sites fully charge-satisfied, these faces would normally be uncharged. However, even at extreme pH levels, the connecting O sites would remain uncharged, and thus would have a very low affinity for adsorbing protons. On the nontronite (010) faces, all surface sites are fully bonded, except for adjacent 1-coordinated OH's bonded to octahedral cations. Each of these is underbonded by 1/2, and when doubly protonated, they would be overbonded by 1/2. Again, however, the connecting O sites are fully bonded, and would have a very low affinity for adsorbing protons.

White and Zelazny (1988) justified their speculations about the surface relaxation discussed above by citing similar phenomena known to occur at the edges of sepiolite and palygorskite (Preisinger, 1959), and by the ability of their model to successfully predict observed anomalies in structural formulae calculated for fine-grained clay minerals. In addition, Childs *et al.* (1999) recently observed the presence of five-coordinate Al in allophane using nuclear magnetic resonance spectroscopy, and suggested these might originate at the edges of incomplete octahedral layers. Since the proposed bond shifts on dioctahdral clay edges would effectively result in five-coordinate octahedral cations, such observations may be significant to White and Zelazny's case. In the case of nontronite, even in the bulk the octahedral sheet is severely distorted, with Fe-O bond lengths ranging from 1.815 Å to 2.062 Å, corresponding to empirically-determined bond strengths of 0.86 to 0.44 (Altermatt and Brown, 1985). This suggests that the proposed bond shifts would not be out of the question. Beyond these simple arguments, molecular modeling calculations are needed to theoretically justify the predicted surface relaxation.

On the other hand, cutting our crystal models along noneuhedral planes to simulate broken edges yielded numerous kink sites, often including underbonded connecting oxygens coordinated to an octahedral cation surrounded by at least two other underbonded anion sites. In such cases we would not expect a complete neutralization of the surface charge.

Similarly, on both the (010), (110), and $(1\bar{1}0)$ edges of hectorite, the underbonded connecting oxygens are bonded to octahedral cations which are also bonded to another undersaturated O. The total strength of bonds (Pauling) coordinating each of these oxygens is 1 2/3, so shifting a 1/3 charge from one site to the other would still leave one of the sites underbonded. Therefore, we would not expect complete autocompensation of the surface charge on these faces, either.

If it is assumed that the slowest step in the dissolution process of nontronite and hectorite is the breaking of connecting oxygen bonds between the octahedral and tetrahedral sheets, the observed differential reactivity is readily explained. That is, all the faces which dissolve relatively quickly, including all the hectorite edge surfaces and nontronite broken edges, are predicted to have coordinatively unsaturated connecting oxygens, which would have a high affinity for attacking protons. On the other hand, the faces observed to dissolve much more slowly, including nontronite (010), (110), and $(1\bar{1}0)$, are predicted to have fully charge-satisfied connecting oxygens with a much lower affinity for protonation. Even the stability of the (100) growth faces on the nontronite laths can be explained if we interpret them as K surfaces composed of elements of the (010), (110), and $(1\bar{1}0)$ edges. Thus, it seems to follow that (100) growth surfaces would exhibit low reactivity, but established dissolution fronts at broken edges or defects likely would not show a tendency to become pinned at a K face.

Implications for the mechanism of proton attack

The conclusion that the dissolution rate is controlled by the breaking of bonds to connecting oxygens between the tetrahedral and octahedral sheets seems inconsistent with the model of kaolinite dissolution proposed by Wieland and Stumm (1992). In their study, Wieland and Stumm measured the surface protonation of kaolinite via potentiometric titration, as well as the dissolution rate, in acidic and basic solutions. They interpreted their results within the framework of the coordinative chemical model of mineral dissolution developed by Furrer and Stumm (1986) and Wieland *et al.* (1988), where dissolution rates of simple oxides in acidic solutions were shown to be proportional to integral orders of the concentration of protonated surface species. It was assumed that these integral orders corresponded to the stoichiometry of a precursor to the rate-controlling activated complex for the dissolution reaction. In the case of kaolinite, Wieland and Stumm (1992) found that the dissolution rate of the edge surfaces in acid solution could be modeled as a first-order function of the concentration of protonated aluminol sites on the edge faces of the mineral. They concluded that the activated complex controlling the dissolution reaction at the kaolinite edge surface had a stoichiometry of 1 H to 1 Al. Such a model seems to implicitly assume that all protonated surface groups associated with the octahedral cations are equally reactive. However, Wieland and Stumm (1992) realized that "precursor configurations" associated with different surface functional groups might have very different surface energies, but appealed to Monte-Carlo simulations which showed that the surface of a dissolving mineral will tend toward a configuration with only one type of surface complex (Wehrli, 1989). On the other hand, Wieland and Stumm's (1992) explanation is still inconsistent with ours, because if the rate-determining step is associated with the hydrolysis of connecting O bonds, rather than easily-protonated, monodentate aluminol groups, there should be no such direct link between total surface protonation on aluminol groups and the rate-determining activated complex.

In the case of nontronite dissolution, one cannot explain the tendency for the reaction front to become pinned at the pseudo-hexagonal face angles in terms of a minimization of protonated surface functional groups associated with the octahedral cations. Such an explanation might suffice for the (110) and $(1\bar{1}0)$ edges, which likely have no such readily-protonated surface functional groups, but not for the (010) edges, which have a reasonably high density of amphoteric, monodentate groups coordinated to an octahedral cation. While the density of these sites on the (010) edges is almost certainly lower than on most broken edges, the difference cannot be so great as to explain the much, much slower dissolution of the nontronite (010) faces.

Another problem with the model proposed by Wieland and Stumm (1992) is that *ab initio* calculations performed by Xiao and Lasaga (1994) predicted the key step in the dissolution of Si-O-Al groups would be proton adsorption on the connecting oxygens. Also, an adsorbed proton on one Si-O-Al group was not predicted to significantly affect the dissolution reaction on neighboring groups. Therefore, the protonation of amphoteric, monodentate surface functional groups on such surfaces should not control their dissolution rates.

Our explanation of the *in situ* observations of nontronite and hectorite dissolution is also consistent with the model of proton attack at the edges of kaolinite proposed by Ganor *et al.* (1995). They found that, within experimental error, kaolinite dissolution rates in acid solutions were first order with respect to the *total* surface protonation. A model of kaolinite dissolution was proposed, where the rate-controlling step is the sequential breaking of bonds to connecting oxygens. They explained the linear dependence of the rates on total surface proton concentration by assuming equilibrium between the various types of surface protonated sites. Assuming the activity coefficients and concentrations of the surface species are reasonably constant during the dissolution reaction, this results in a first-order reaction with respect to total surface proton concentration. In a similar study, Zysset and Schindler (1996) showed that the proton-promoted dissolution of montmorillonite is first order with respect to total surface proton concentration, including protons inferred to have exchanged into the interlayer spaces of the mineral. They proposed that the dissolution rate is controlled by hydrolysis of either Si-O-Al or Al-OH-Al bonds, and that protons adsorbed anywhere on the montmorillonite surface can quickly diffuse to the active sites. This explanation appears to be nearly equivalent, at least qualitatively, to the one proposed by Ganor *et al.* (1995). However, the possibility that the breaking of bonds between octahedral sites controls the dissolution rate can be excluded on the basis of the hectorite dissolution data reported by Bosbach *et al.* (1999), who showed that the step retreat rate for hectorite was much slower than that for brucite (Jordan & Rammensee, 1996).

Concluding Remarks

The *in situ* observations of the dissolution of nontronite and hectorite laths described here have graphically revealed the differential reactivity of various crystal faces on these minerals. We have shown that if Hartman-Perdock crystal growth theory is applied to the prediction of edge site topology, and the type of surface relaxation proposed by White and Zelazny (1988) occurs on these surfaces, a ready explanation for the observed reactivity emerges. That is, dissolution reactions are observed to be much slower on surfaces where the oxygen atoms connecting the octahedral and tetrahedral sheets are predicted to be coordinatively saturated. This conclusion also implies that the hydrolysis of these connecting sites controls the dissolution rate.

Aside from any implications about the dominant mechanism of dissolution, such models of phyllosilicate edge structure could have a profound effect on geochemical calculations based on assumed edge site densities. This is especially true with respect to dioctahedral minerals with a dominantly euhedral habit. For example, two-thirds of the edge surface area on a hexagonal kaolinite crystal might be charge-free at normal pH levels.

Given the environmental and industrial importance of reactions taking place at the edges of phyllosilicate minerals, we suggest that further attempts should be made to explore their structure and reactivity. Given the extant data, two available courses of action seem to present themselves. First, molecular modeling calculations should be applied to phyllosilicate edge surfaces to see whether the surface relaxation predicted by White and Zelazny (1988) can be theoretically justified. Second, Monte-Carlo simulations of the dissolution of phyllosilicate mineral structures, such as those discussed by Lasaga (1995) for kaolinite, should be performed to see which combinations of bond strengths, etc., would result in the kind of differential reactivity observed in this study.

Acknowledgements

We thank Michel Schlegel for preparing the hectorite suspension. BB, MH, and ER are grateful for the support of the National Science Foundation (EAR-9628023, EAR-9902996, and the Graduate Student Fellowship program) and the Petroleum Research Fund administered by the American Chemical Society (ACS-PRF 31598-AC2 and ACS-PRF 34326-AC2). DB and LC are grateful for financial support by the Deutscher Akademischer Austauschdienst and the French Ministery of Foreign affairs.

References Cited

Altermatt, D., and Brown, I.D. (1985) Bond-valence parameters obtained from a systematic analysis of the inorganic crystal structure database. Acta Crystallographica, B41, 244-247.

Anderson, S.J., and Sposito, G. (1991) Cesium-adsorption method for measuring accessible structural surface charge. Soil Science Society of America Journal, 55, 1569-1576.

Bargar, J.R., Towle, S.N., Brown, G.E., Jr., and Parks, G.A. (1997) XAFS and bond-valence determination of the structures and compositions of surface functional groups and Pb(II) and Co(II) sorption products on single-crystal α-Al_2O_3. Journal of Colloid and Interface Science, 185, 473-492.

Barrett, S.D. (1997) Image analysis and the internet. Scientific Data Management, 1, 18-25.

Besson, G., de la Calle, C., Rautureau, M., Tchoubar, C., Tsipurski, S.I., and Drits, V.A. (1982) X-ray and electron diffraction study of the structure of the Garfield nontronite. Developments in Sedimentology, 35, 29-40.

Besson, G., Bookin, A.S., Dainyak, L.G., Rautureau, M., Tsipursky, S.I., Tchoubar, C., and Drits, V.A. (1983) Use of diffraction and Mössbauer methods for the structural and crystallochemical characterization of nontronites. Journal of Applied Crystallography, 16, 374-383.

Bickmore, B.R., Hochella, M.F., Jr., Bosbach, D., and Charlet, L. (1999a) Methods for performing Atomic Force Microscopy imaging of clay minerals in aqueous solutions. Clays and Clay Minerals, 47, 573-581.

Bickmore, B.R., Rufe, E., Barrett, S.D., and Hochella, M.F., Jr. (1999b) Measuring discrete feature dimensions in AFM images with Image SXM. Geological Materials Research, 1, n.5. See http://gmr.minsocam.org

Bleam, W.F. (1993) Atomic theories of phyllosilicates: Quantum chemistry, statistical mechanics, electrostatic theory, and crystal chemistry. Reviews of Geophysics, 31, 51-73.

Bleam, W.F., Welhouse, G.J., and Janowiak, M.A. (1993) The surface Coulomb energy and proton Coulomb potentials of pyrophyllite {010}, {110}, {100}, and {130} edges. Clays and Clay Minerals, 41, 305-316.

Bloss, F.D., Shekarchi, E., and Shell, H.R. (1959) Hardness of synthetic and natural micas. American Mineralogist, 44, 33-48.

Boisen, M.B., and Gibbs, G.V. (1985) Mathematical Crystallography, Reviews in Mineralogy 15, 460 pp. The Mineralogical Society of America.

Bonin, D., Calas, G., Suquet, H., and Pezerat, H. (1985) Sites occupancy of Fe^{3+} in Garfield nontronite: A spectroscopic study. Physics and Chemistry of Minerals, 12, 55-64.

Bosbach, D., and Rammensee, W. (1994) In situ investigation of growth and dissolution on the (010) surface of gypsum by Scanning Force Microscopy. Geochimica et Cosmochimica Acta, 58, 843-849.

Bosbach, D., Jordan, G., and Rammensee, W. (1995) Crystal growth and dissolution kinetics of gypsum and fluorite: An in situ Scanning Force Microscope study. European Journal of Mineralogy, 7, 267-278.

Bosbach, D., and Hochella, M.F. Jr. (1996) Gypsum growth in the presence of growth inhibitors: a scanning force microscopy study. Chemical Geology, 132, 227-236.

Bosbach, D., Junta-Rosso, J.L., Becker, U., and Hochella, M.F. Jr. (1996) Gypsum growth in the presence of background electrolytes studied by Scanning Force Microscopy. Geochimica et Cosmochimica Acta, 60, 3295-3304.

Bosbach, D., Hall, C., and Putnis, A.. (1998) Mineral precipitation and dissolution in aqueous solution: in-situ microscopic observations on barite (001) with atomic force microscopy. Chemical Geology, 151, 143-160.

Bosbach D, Charlet L, Bickmore BR, Hochella, MF, Jr. (1999) The dissolution of hectorite: In-situ, real-time observations using Atomic Force Microscopy. American Mineralogist, in press.

Brady, P.V., Cygan, R.T., and Nagy, K.L. (1996) Molecular controls on kaolinite surface charge. Journal of Colloid and Interface Science, 183, 356-364.

Casey, W.H., Carr, M.J., and Graham, R.A. (1988) Crystal defects and the dissolution kinetics of rutile. Geochimica et Cosmochimica Acta, 52, 1545-1556.

Charlet, L., Schindler, P.W., Spadini, L., Furrer, G., Zysset, M. (1993) Cation adsorption on oxides and clays—the Aluminum case. Aquatic Sciences, 55, 291-303.

Childs, C.W., Hayashi, S., Newman, R.H. (1999) Five-coordinate aluminum in allophane. Clays and Clay Minerals, 47, 64-69.

Deer, W.A., Howie, R.A., and Zussman, J. (1992) An Introduction to the Rock-Forming Minerals, 2nd edition. Longman Scientific & Technical.

Dove, P., and Chermak, J. (1994) Mineral-water interactions: Fluid cell applications of scanning force microscopy. In Scanning Probe Microscopy of Clay Minerals (ed. K.L. Nagy and A.E. Blum), pp. 139-169. The Clay Minerals Society.

Dove, P.M., and Hochella, M.F. Jr. (1993) Calcite precipitation mechanisms and inhibition by orthophosphate: In situ observations by Scanning Force Microscopy. Geochimica et Cosmochimica Acta, 57, 705-714.

Drake, B., Prater, C.B., Weisenhorn, A.L., Gould, S.A.C., Albrecht, T.R., Quate, C.F., Cannell, D.S., Hansma, H.G., and Hansma, P.K. (1989) Imaging crystals, polymers, and processes in water with the atomic force microscope. Science, 243, 1586-1588.

Eggleton, R.A. (1977) Nontronite: Chemistry and X-ray diffraction. Clay Minerals, 12, 181.

Eslinger E, and Pevear D. (1988) Clay Minerals for Petroleum Geologists and Engineers. Society of Economic Paleontologists and Mineralogists.

Fouke, B.W., and Reeder, R.J. (1992) Surface structural controls on dolomite composition: Evidence from sectoral zoning. Geochimica et Cosmochimica Acta, 56, 4015-4024.

Furrer, G., and Stumm, W. (1986) The coordination chemistry of weathering: I. Dissolution kinetics of d-Al_2O_3 and BeO. Geochimica et Cosmochimica Acta, 50, 1847-1860.

Ganor, J., Mogollón, J.L., and Lasaga, A.C. (1995) The effect of pH on kaolinite dissolution rates and on activation energy. Geochimica et Cosmochimica Acta, 59, 1037-1052.

Grantham, M.C., and Dove, P.M. (1996) Investigation of bacterial-mineral interactions using Fluid Tapping Mode Atomic Force Microscopy. Geochimica et Cosmochimica Acta, 60, 2473-2480.

Grim, R.E., and Güven, N. (1978) Bentonites. Geology, Mineralogy, Properties and uses. Developments in Sedimentology, 24. Elsevier.

Güven, N. (1988) Smectites. In Hydrous phyllosilicates (ed. S.W. Bailey), Reviews in Mineralogy 19, pp. 497-560. Mineralogical Society of America.

Hansma, P.K., Cleveland, J.P., Radmacher, M., Walters, D.A., Hillner, P.E., Bezanilla, M., Fritz, M., Vie, D., Hansma, H.G., Prater, C.B., Massie, J., Fukunaga, L., Gurley, J., and Elings, V. (1994) Tapping mode atomic force microscopy in liquids. Applied Physics Letters, 64, 1738-1740.

Hartman, P. (1963) Structure, growth and morphology of crystals. Zeitschrift für Krystallographie, 119, 65-78.

Hartman, P. (1973) Structure and morphology. In Crystal Growth: An Introduction (ed. P. Hartman), pp. 367-402. North Holland Publishing Company.

Hartman, P. (1978) On the validity of the Donnay-Harker Law. Canadian Mineralogist, 16, 387-391.

Hartman, P. (1982) On the growth of dolomite and kaolinite crystals. Neues Jahrbuch für Mineralogie, Monatshefte 1982, 84-92.

Hartman, P., and Perdock, W.G. (1955a) On the relations between structure and morphology of crystals. I. Acta Crystallographica, 8, 49-52.

Hartman, P., and Perdock, W.G. (1955b) On the relations between structure and morphology of crystals. II. Acta Crystallographica, 8, 521-524.

Hartman, P., and Perdock, W.G. (1955c) On the relations between structure and morphology of crystals. III. Acta Crystallographica, 8, 525-529.

Hillner, P.E., Gratz, A.J., Manne, S., and Hansma, P.K. (1992) Atomic-Scale imaging of calcite and dissolution in real time. Geology, 20, 359-362.

Hochella, M.F., Jr. (1990) Atomic structure, microtopography, composition, and reactivity of mineral surfaces. In Mineral-Water Interface Geochemistry (M.F. Hochella, Jr., and A.F. White), Reviews in Mineralogy 23, pp. 87-132. The Mineralogical Society of America.

Hochella, M.F. Jr. (1995) Mineral surfaces: Their characterization and their chemical, physical and reactive nature. In Mineral Surfaces (ed. D.J. Vaughan and R.A.D. Pattrick), pp. 17-60. Chapman & Hall.

Hochella, M.F., Jr., Rakovan, J., Rosso, K., Bickmore, B., and Rufe, E. (1998) New directions in mineral surface geochemical research using scanning probe microscopy. In Mineral-Water Interfacial Reactions: Kinetics and Mechanisms (ed. D.L. Sparks and T.J. Grundl), ACS Symposium Series Vol. 715, pp. 37-56. American Chemical Society.

Johnson, C.A. (1995) Applications of scanning probe microscopy part 4: AFM imaging in fluids for the study of colloidal particle adsorption. American Laboratory, 27, 12.

Jordan, G., and Rammensee, W. (1996) Dissolution rates and activation energy for dissolution of brucite (001): A new method based on the microtopography of crystal surfaces. Geochimica et Cosmochimica Acta, 60, 5055-5062.

Junta, J.L., and Hochella, M.F. Jr. (1994) Manganese (II) oxidation at mineral surfaces: A microscopic and spectroscopic study. Geochimica et Cosmochimica Acta, 58, 4985-4999.

Junta-Rosso, J.L, Hochella, M.F. Jr., and Rimstidt, J.D. (1997) Linking microscopic and macroscopic data for heterogeneous reactions illustrated by the oxidation of manganese (II) at mineral surfaces. Geochimica et Cosmochimica Acta, 61, 149-159.

Kadi-Hanifi, M., and Méring, J. (1972) Précisions sur la structure de l'hectorite. C.R. Acad. Sc. Paris, Série D, 274, 149-151.

Kaviratna, H., & Pinnavaia, T.J. (1994) Acid hydrolysis of octahedral Mg^{2+} sites in 2:1 layered silicates: An assessment of edge attack and gallery access mechanisms. Clays and Clay Minerals, 42, 717-723.

Klein, C., and Hurlbut, C.S., Jr. (1993) Manual of Mineralogy, 21st ed., 681 pp. John Wiley & Sons.

Koretsky, C.M., Sverjensky, D.A., Sahai, N. (1998) A model of surface site types on oxide and silicate minerals based on crystal chemistry: Implications for site types and densities, multi-site adsorption, surface infrared spectroscopy, and dissolution kinetics. American Journal of Science, 298, 349-438.

Lasaga, A.C. (1995) Fundamental approaches in describing mineral dissolution and precipitation rates. In Chemical Weathering Rates of Silicate Minerals (ed. A.F. White and S.L. Brantley), Reviews in Mineralogy 31, pp. 23-86. Mineralogical Society of America.

Lazarenko, E.K., Krochuk, V.M., and Pavlishin, V.I. (1979) New data on the morphology of phlogopite crystals and their typomorphic significance. Transactions (Doklady) of the U.S.S.R. Academy of Sciences: Earth Science Sections, 246, 157-159.

Liang, Y., Baer, D.R., McCoy, J.M., Amonette, J.E., and LaFemina, J.P. (1996) Dissolution kinetics at the calcite-water interface. Geochimica et Cosmochimica Acta, 60, 4883-4887.

Manceau, A., Chateigner, D., and Gates, W.P. (1998) Polarized EXAFS, distance-valence least-squares modeling (DVLS), and quantitative texture analysis approaches to the structural refinement of Garfield nontronite. Physics and Chemistry of Minerals, 25, 347-365.

Muljadi, D., Posner, A.M., and Quirk, J.P. (1966) The mechanism of phosphate adsorption by kaolinite, gibbsite, and pseudoboehmite. Journal of Soil Science, 17, 212-247.

Murad, E. (1987) Mössbauer spectra of nontronites: structural implications and characterization of associated iron oxides. Zeits. Pflanzenernaehr. Bodenk. 150, 279-285.

Nagy, K.L. (1995) Dissolution and precipitation kinetics of sheet silicates. In Chemical Weathering Rates of Silicate Minerals (ed. A.F. White and S.L. Brantley), Reviews in Mineralogy 31, pp. 173-233. Mineralogical Society of America.

Nagy, K.L., and Blum, A.E., Eds. (1994) Scanning Probe Microscopy of Clay Minerals, CMS Workshop Lectures vol. 7, 239 pp. Clay Minerals Society.

Oberlin, P.A., and Méring, J. (1966) Observations sur l'hectorite (etude en microscopie et diffraction electroniques). Bull. Soc. fran. Miner. Crist., LXXXIX, 29-40

Pandya, N.S., and Pandya, J.R. (1959) Etching of mica by fused alkalies. Bulletin of the National Institute of Sciences of India, 14, 148-151.

Paquette, J., and Reeder, R.J. (1990) New type of compositional zoning in calcite: Insights into crystal-growth mechanisms. Geology, 18, 1244-1247.

Park, N.-S., Kim, M.-W., Langford, S.C. & Dickinson, J.T. (1996) Atomic layer wear of single-crystal calcite in aqueous solution using scanning force microscopy. Journal of Applied Physics, 80, 2680-2686.

Patel, A.R., and Ramanathan, S. (1962) Etching Mica Cleavages. Acta Crystallographica, 15, 860-862.

Preisinger, A. (1959) X-ray study of the structure of sepiolite. In Clays and Clay Minerals, Proceedings of the 6th National Conference, Berkeley, California, 1957 (ed. A. Swineford), pp. 61-67. Pergamon Press.

Putnis, A., Junta-Rosso, J.L., and Hochella, M.F. Jr. (1995) Dissolution of barite by a chelating ligand: An atomic force microscopy study. Geochimica et Cosmochimica Acta, 59, 4623-4632.

Rakovan, J., Becker, U., and Hochella, M.F., Jr. (1999) Aspects of goethite surface microtopography, structure, chemistry, and reactivity. American Mineralogist, 84, 884-894.

Rich, C.I. (1969) Suction apparatus for mounting clay specimens on ceramic tile for x-ray diffraction. Soil Science Society of America Proceedings, 33, 815-816.

Rufe, E., and Hochella, M.F., Jr. (1999) Quantitative assessment of reactive surface area of phlogopite dissolution during acid dissolution. Science, 285, 874-876.

Russ, J.C. (1995) The Image Processing Handbook, 2nd Ed., 674 pp. CRC.

Schlegel, M.L., Manceau, A., Chateigner, D., and Charlet, L. (1999) Sorption of metal ions on clay minerals: I. Polarized EXAFS evidence for the adsorption of Co on the edges of hectorite particles. Journal of Colloid and Interface Science, 215, 140-158.

Schofield, R.D., and Samson, H.R. (1953) The deflocculation of kaolinite suspensions and the accompanying change over from positive to negative chloride adsorption. Clay Minerals Bulletin, 2, 45-51.

Sposito, G. (1984) The Surface Chemistry of Soils, 277 pp. Oxford University Press.

Sun, B.N., and Baronnet, A. (1989a) Hydrothermal growth of OH-phlogopite single crystals. I. Undoped growth medium. Journal of Crystal Growth, 96, 265-276.

Sun, B.N., and Baronnet, A. (1989b) Hydrothermal growth of OH-phlogopite single crystals. II. Role of Cr and Ti adsorption on crystal growth rates. Chemical Geology, 78, 301-314.

Teng, H.H., Dove, P.M., Orme, C.A., and De Yoreo, J.J.. (1998) Thermodynamics of Calcite Growth: Baseline for Understanding Biomineral Formation. Science, 282, 724-727.

Towle, S.N., Brown, G.E., Jr., and Parks, G.A. (1999a) Sorption of Co(II) on metal oxide surfaces: I. Identification of specific binding sites of Co(II) on (110) and (001) surfaces of TiO_2 (rutile) by Grazing-Incidence XAFS Spectroscopy. Journal of Colloid and Interface Science, 217, 299-311.

Towle, S.N., Bargar, J.R., Brown, G.E., Jr., and Parks, G.A. (1999b) Sorption of Co(II) on metal oxide surfaces: II. Identification of Co(II)(aq) adsorption sites on the (0001) and (1-102) surfaces of α-Al_2O_3 by Grazing-Incidence XAFS Spectroscopy. Journal of Colloid and Interface Science, 217, 312-321.

Turpault M.-P. Trotignon L. (1994) The dissolution of biotite single crystals in dilute HNO_3 at 24°C: Evidence of an anisotropic corrosion process of micas in acidic solutions. Geochimica et Cosmochimica Acta, 58, 2761-2775.

van Santen, R.A. (1982) Chemical-bonding aspects of heterogeneous catalysis. II. Solid acids. Recueil, Journal of the Royal Netherlands Chemical Society, 101, 157-163.

Wehrli, B. (1989) Monte-Carlo simulations of surface morphologies during mineral dissolution. Journal of Colloid and Interface Science, 132, 230-242.

White, G.N., and Zelazny, L.W. (1988) Analysis and implications of the edge structure of dioctahedral phyllosilicates. Clays and Clay Minerals, 36, 141-146.

Wieland, E., Wehrli, B., and Stumm, W. (1988) The coordination chemistry of weathering. III. A generalization on the dissolution rates of minerals. Geochimica et Cosmochimica Acta, 52, 1969-1981.

Wieland, E., and Stumm, W. (1992) Dissolution kinetics of kaolinite in acidic aqueous solutions at 25 ºC. Geochimica et Cosmochimica Acta, 56, 3339-3355.

Xiao, Y., and Lasaga, A.C. (1994) Ab initio quantum mechanical studies of the kinetics and mechanisms of silicate dissolution: H^+ (H_3O^+) catalysis. Geochimica et Cosmochimica Acta, 58, 5379-5400.

Zachara, J.M., and McKinley, J.P. (1993) Influence of hydrolysis on the sorption of metal cations by smectites: Importance of edge coordination reactions. Aquatic Sciences, 55, 250-261.

Ziolkowski, J. (1986) Crystallochemical model of active sites on oxide catalysts. Journal of Catalysis, 100, 45-58.

Zysset, M., and Schindler, P.W. (1996) The proton promoted dissolution kinetics of K-montmorillonite. Geochimica et Cosmochimica Acta, 60, 921-931.

Table 1. Site Types and Densities on Nontronite and Hectorite Edge Faces

site type	*coordinating atoms*	*coordinating bond strength*	*sites per unit cell face*	*Sites per nm^2*
Nontronite (110) and (1$\bar{1}$0)				
O	Si	1	4	3.76
O	2 Si	2	8	7.53
O	Si, 2 Fe	2	2	1.88
O	Si, Fe	1 1/2[†]	2	1.88
O	Fe	1/2[‡]	2	1.88
OH	2 Fe	1	2	1.88
Nontronite (010)				
O	Si	1	2	3.80
O	2 Si	2	4	7.59
O	Si, 2 Fe	2	2	3.80
OH	Fe	1/2	2	3.80
Hectorite (110) and (1$\bar{1}$0)				
O	Si	1	4	3.70
O	2 Si	2	8	7.41
O	Si, 2 Mg	1 2/3	2	1.85
O	Mg	1/3	2	1.85
OH	2 Mg	2/3	2	1.85
OH	Mg	1/3	2	1.85
Hectorite (010)				
O	Si	1	2	3.94
O	2 Si	2	4	7.89
O	Si, 2 Mg	1 2/3	2	3.94
OH	Mg	1/3	2	3.94

[†] These bonds are predicted to shorten, so that the coordinating bond strenth will total 2.

[‡] These bonds are predicted to lengthen to bond strength 0, so that when the site is doubly

Table 5-1. Site types and densities of nontronite and hectorite edge faces.

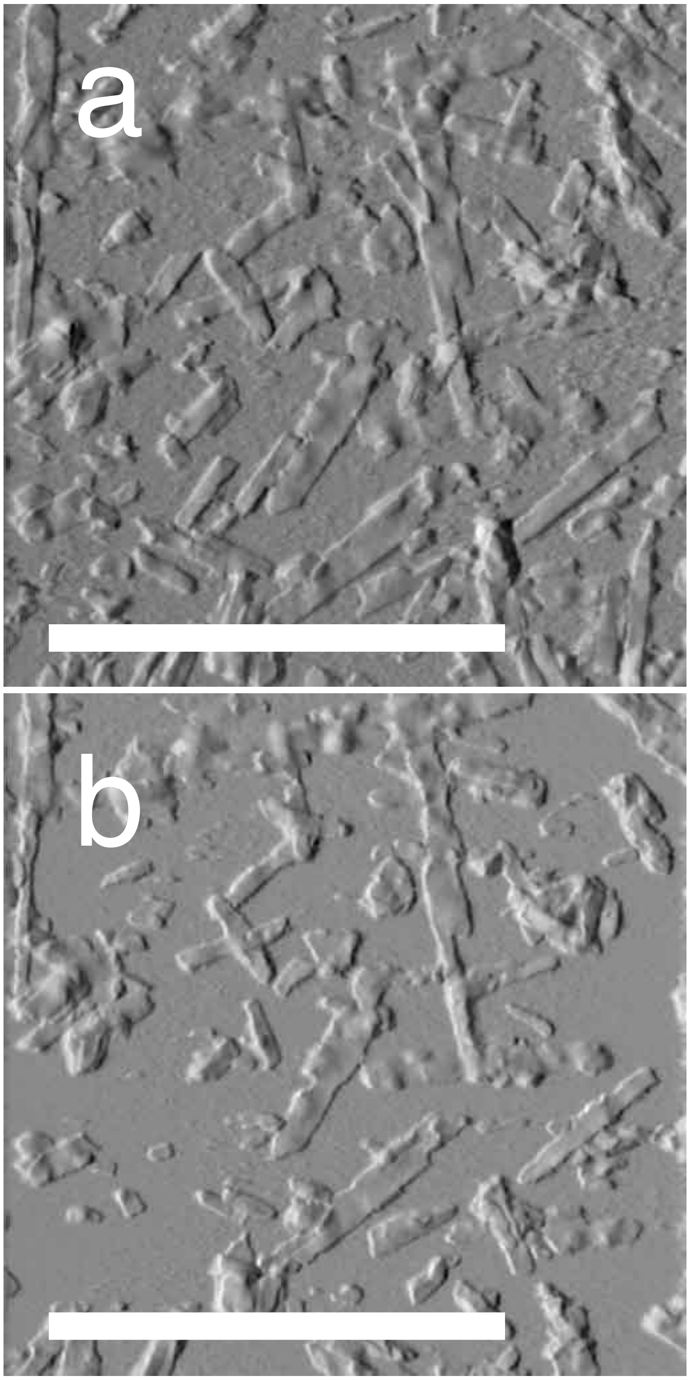

Figure 5-1. AFM deflection images of hectorite laths during a dissolution experiment. a) Under deionized water. b) The same area after 45 min. exposure to pH 2 HCl. Scale bar = 1 μm. Most particles are ~2 nm in height.

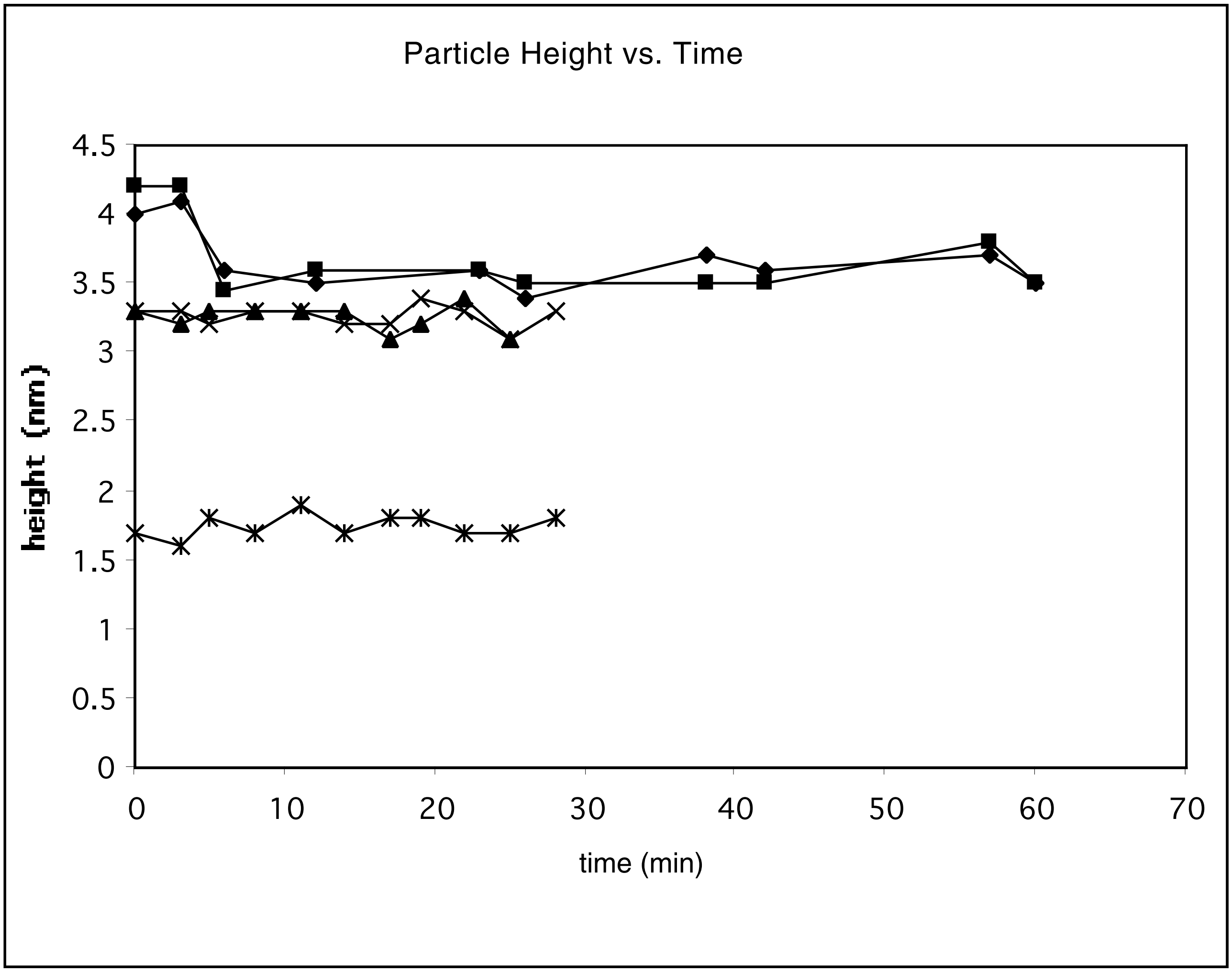

Figure 5-2. Measured particle heights of several very flat nontronite laths over time during dissolution experiments. While significant dissolution took place at the edges of all these particles, the particle heights appeared to stay essentially constant.

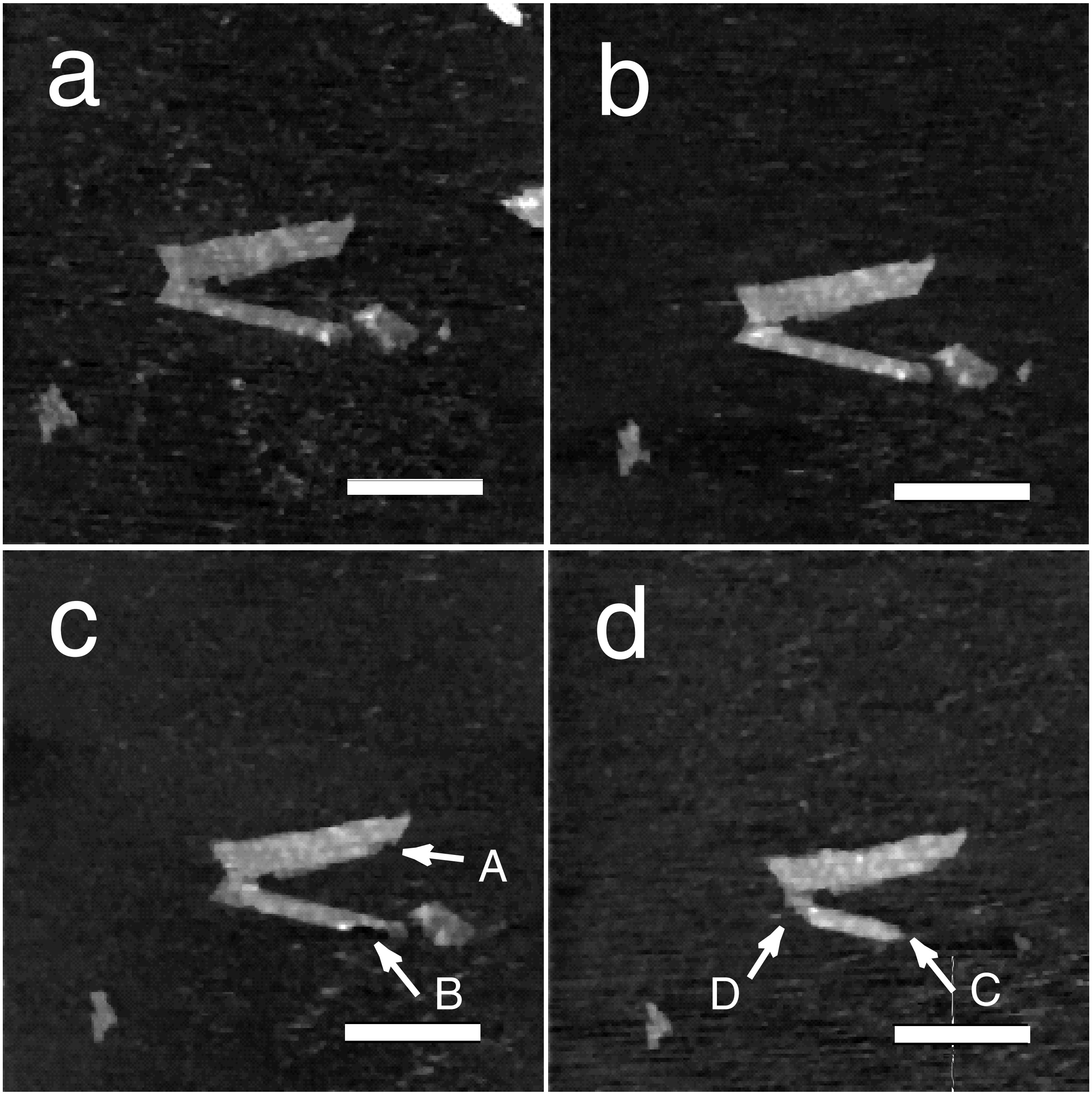

Figure 5-3. AFM height images of nontronite laths after a) 0 min., b) 6 min., c) 38 min., and d) 60 min. of exposure to pH 2 HCl. Scale bar = 1 μm. The two particles in the middle are both ~4 nm in height.

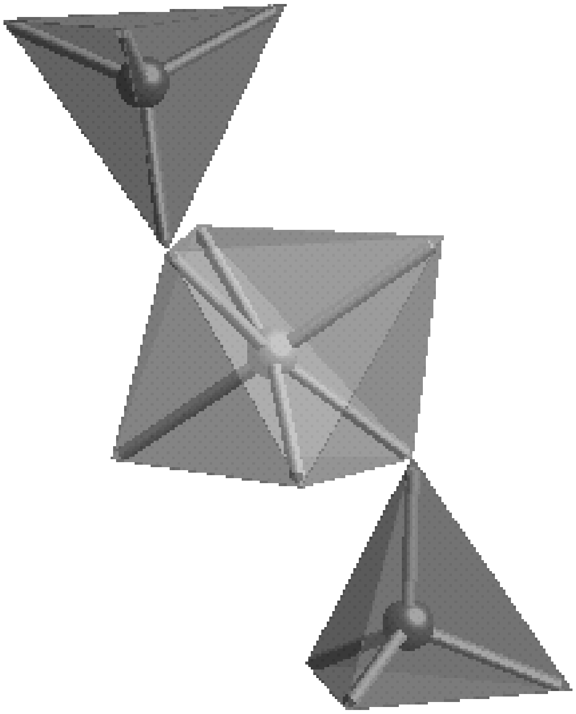

Figure 5-4. One stoichiometric crystal growth unit for a dioctahedral 2:1 phyllosilicate, assuming random substitutions.

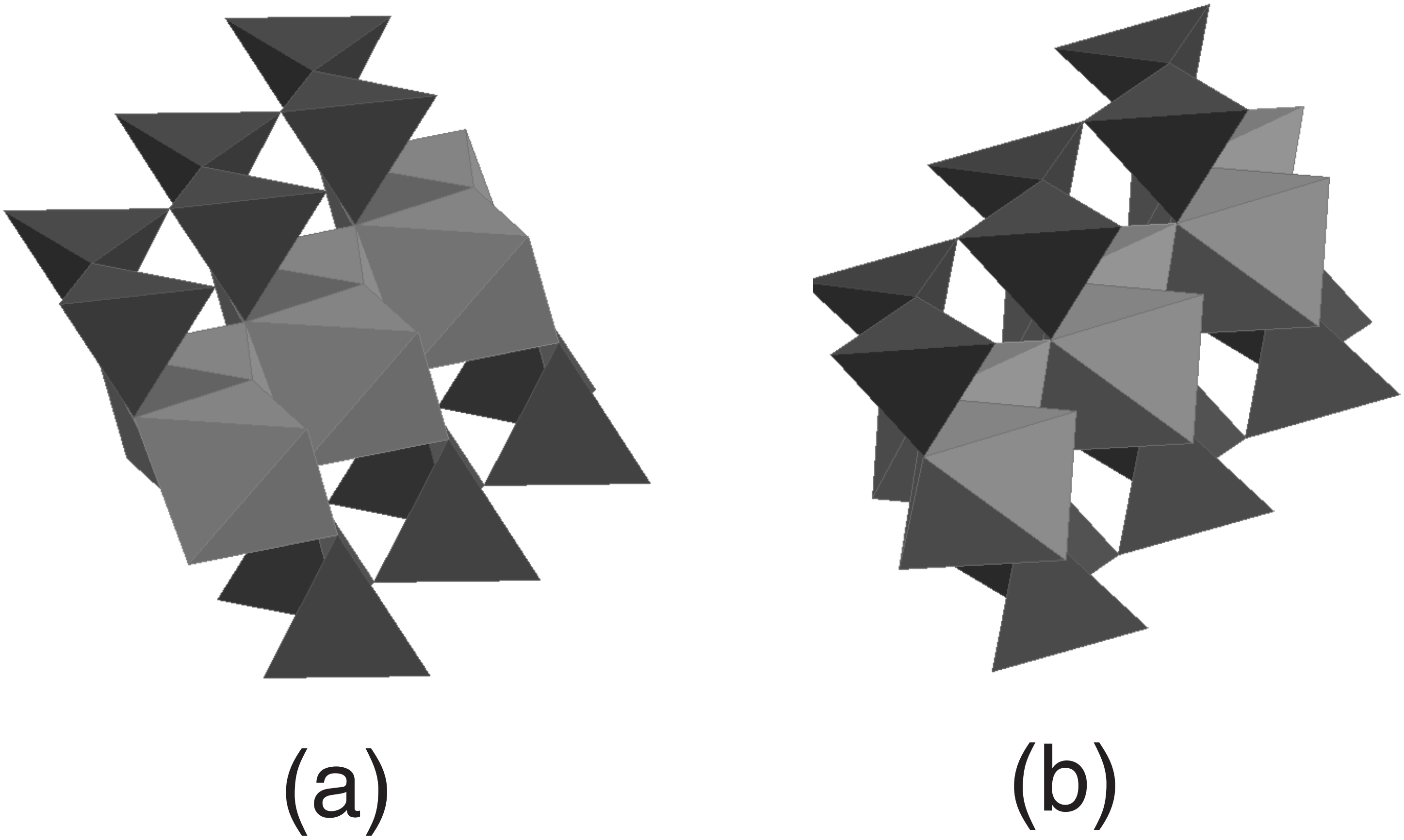

Figure 5-5. Stoichiometric Periodic Bond Chains (PBCs) for a dioctahedral 2:1 phyllosilicate. a) Chain running parallel to the (110) face. The ( ) face is symmetrically equivalent. b) Chain running parallel to the (010) face.

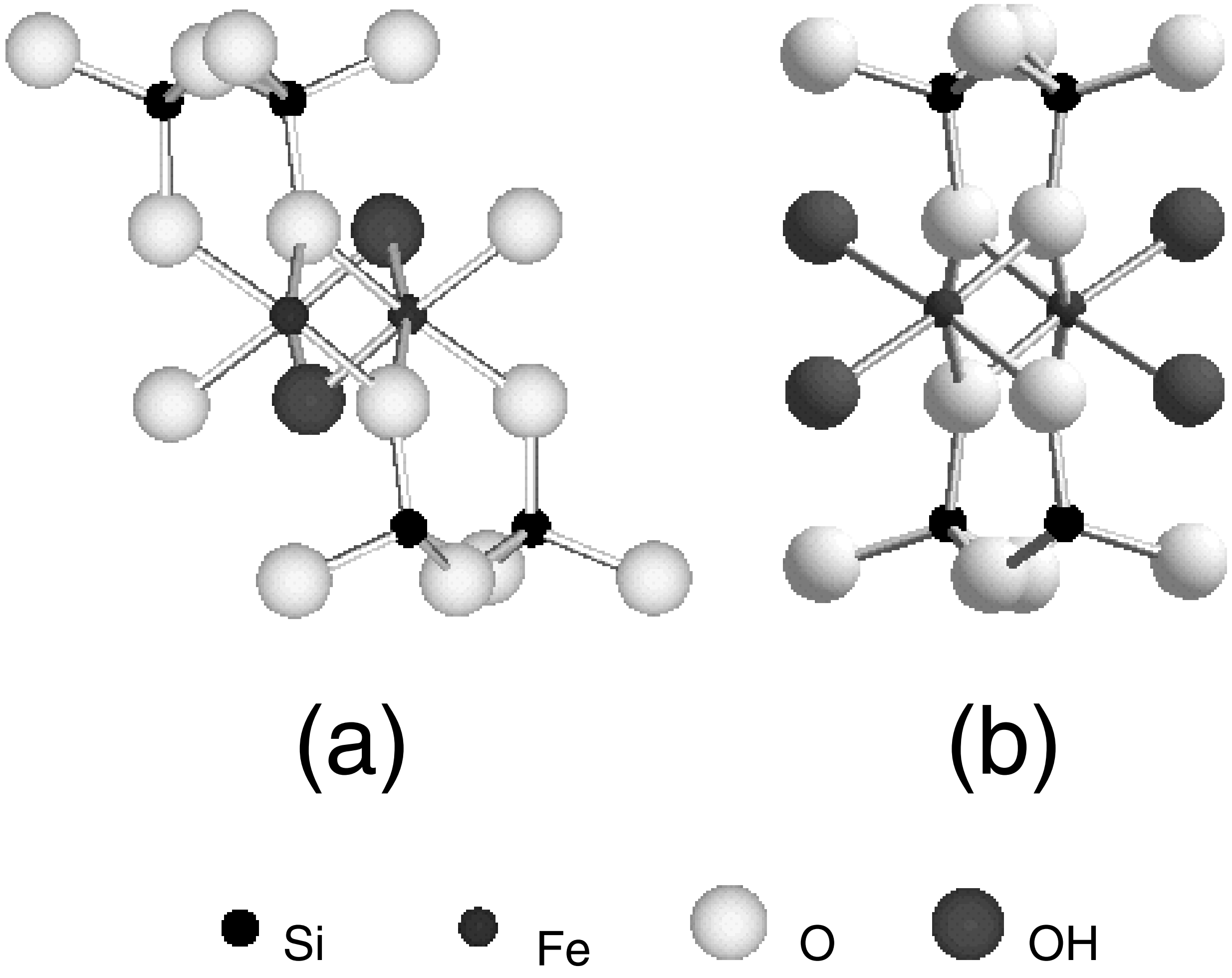

Figure 5-6. Ball and stick models of the Periodic Bond Chains (PBCs) in Fig. 5, viewed parallel to the PBC vector. a) Chain parallel to the (110) face. The ( ) face would be symmetrically equivalent. b) Chain parallel to the (010) face.

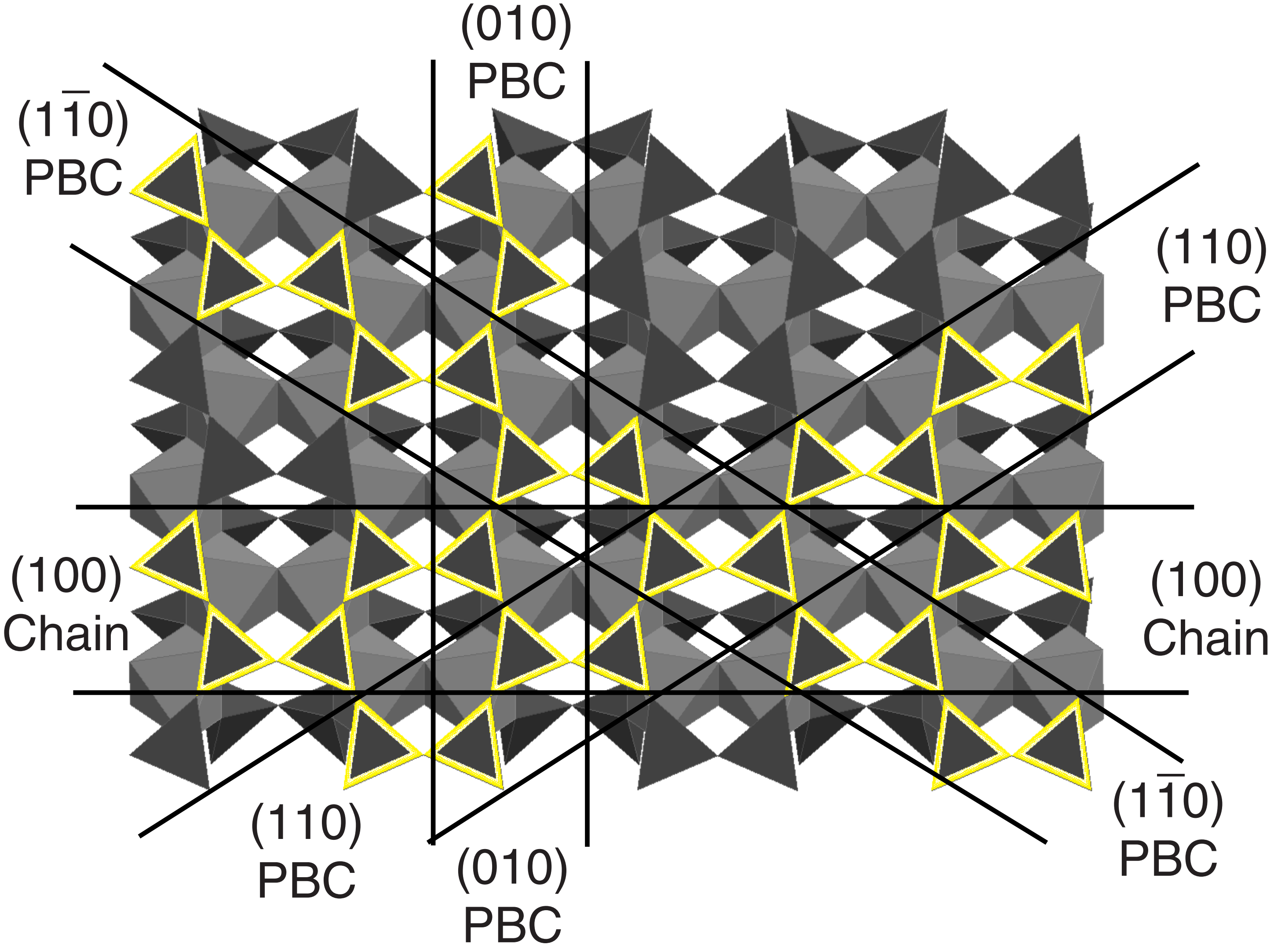

Figure 5-7. Polyhedral representation of a dioctahedral T-O-T layer. The highlighted tetrahedra are part of the bond chains indicated in the figure. It can clearly be seen that the chain parallel to the (100) face is composed entirely of elements of the (110), ( ), and (010) Periodic Bond Chains (PBCs). Thus, (100) should not be treated as a PBC.

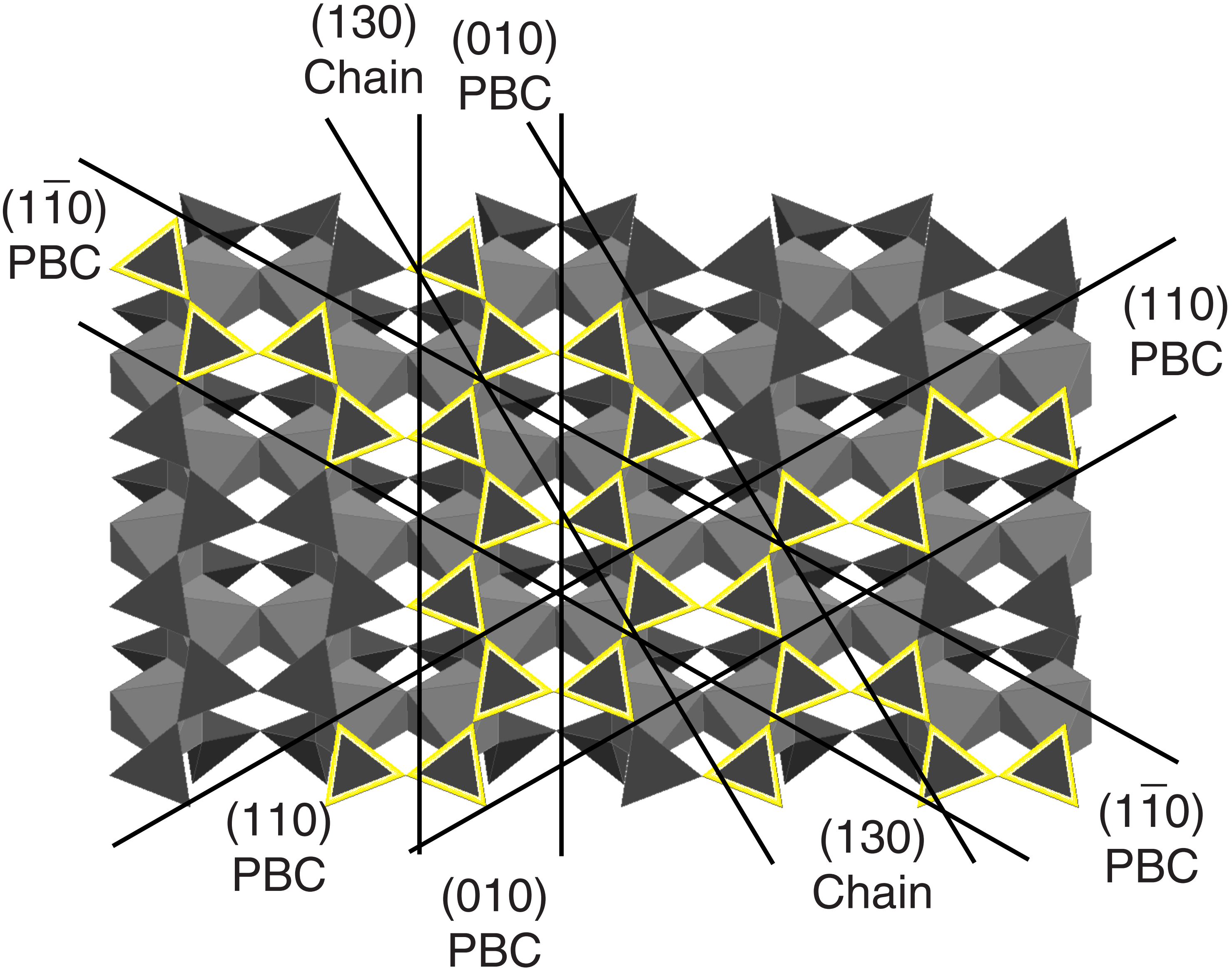

Figure 5-8. Polyhedral representation of a dioctahedral T-O-T layer. The highlighted tetrahedra are part of the bond chains indicated in the figure. It can clearly be seen that the chain parallel to the (130) face is composed entirely of elements of the (110), ( ), and (010) Periodic Bond Chains (PBCs). Thus, (130) should not be treated as a PBC.

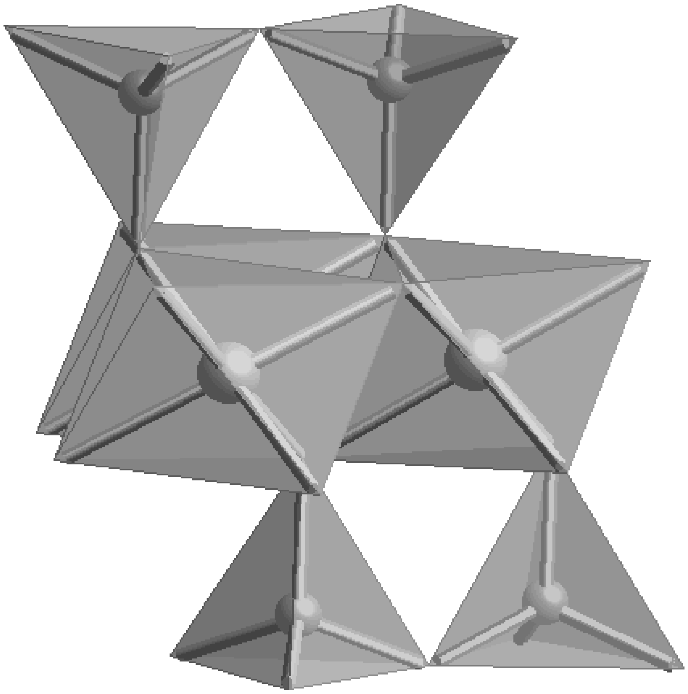

Figure 5-9. One stoichiometric crystal growth unit for a trioctahedral 2:1 phyllosilicate, assuming random substitutions.

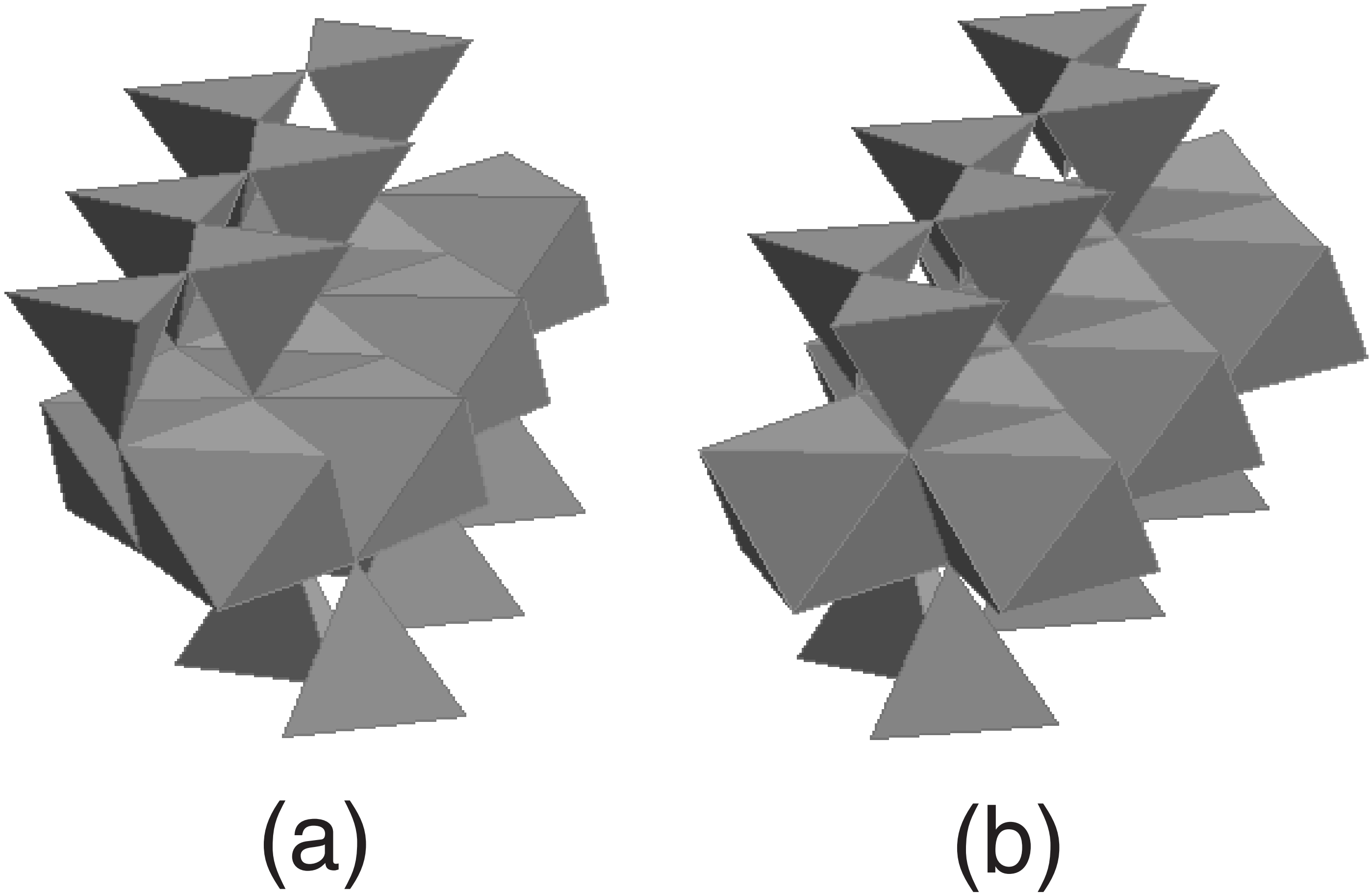

Figure 5-10. Stoichiometric Periodic Bond Chains (PBCs) for a trioctahedral 21 phyllosilicate. a) Chain running parallel to the (110) face. The ( ) face is symmetrically equivalent. b) Chain running parallel to the (010) face.

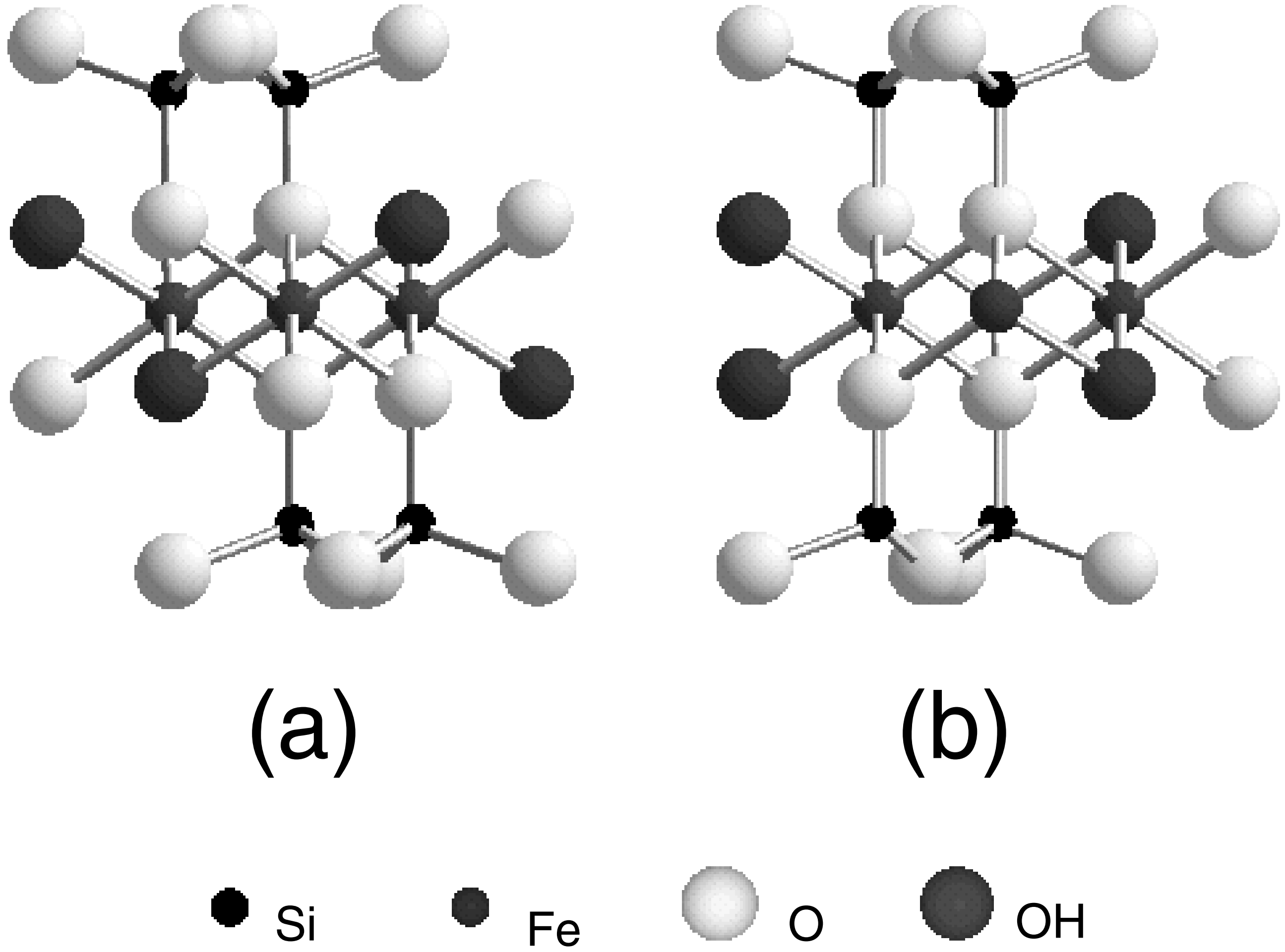

Figure 5-11. Ball and stick models of the Periodic Bond Chains (PBCs) in Fig. 10, viewed parallel to the PBC vector. a) Chain parallel to the (110) face. The ( ) face would be symmetrically equivalent. b) Chain parallel to the (010) face.

Vita

"I Am Barry" or "Nobody is Going to Read This, Anyway"

I am Barry, hear me snore
because I'm so smart I am bored
And I know too much to go back an' pretend
'cause I've heard it all before
And I've been down there on the floor
No one's ever gonna keep me down again

CHORUS:

Oh yes I am wise
But it's wisdom born of pain
Yes, I've paid the price
But look how much I gained
If I have to, I can do anything

I am strong (strong)
I am invincible (invincible)
I am Barry

You can bend but never break me
'cause it only serves to make me
More determined to achieve my final goal
And I come back even stronger
Not a novice any longer
'cause you've deepened the conviction in my soul

CHORUS:

I am Barry watch me blow
the competition out the do'
As I spread my heap big mojo across the land
But I'm still an embryo
With a long long way to go
Until I make my future bosses understand

Oh yes I am wise
But it's wisdom born of pain
Yes, I've paid the price
But look how much I gained
If I have to I can face anything
I am strong (strong)
I am invincible (invincible)
I am Barry
Oh, I am Barry
I am invincible
I am strong

FADE
I am Barry
I am invincible
I am strong
I am Barry